MODELLING THE STATIC PROPERTIES OF IONS UNDER

DIFFERENT CHARGE DISTRIBUTIONS.

A THESIS

SUBMITTED TO THE UNIVERSITY OF STRATHCLYDE

FOR THE DEGREE OF

PHD IN CHEMICAL AND PROCESS ENGINEERING

IN THE FACULTY OF ENGINEERING

PAUL MATTHEW DUNCAN

Academic Supervisors: Dr. Leo Lue and Dr. Paul Mulheran

DEPARTMENT OF CHEMICAL AND PROCESS ENGINEERING

2016

Declaration of Authenticity and Authors Rights

This thesis is the result of the authors original research. It has been composed by the author and has not been previously submitted for examination which has led to the award of a degree.

The copyright of this thesis belongs to the author under the terms of the United Kingdom Copyright Acts as qualified by University of Strathclyde Regulation 3.50. Due acknowledgement must always be made of the use of any material contained in, or derived from, this thesis.

Signed:

Date:

Acknowledgements

I would like to thank my academic supervisor Dr Leo Lue for his advice, guidance and infinite patience throughout my PhD. His knowledge and enthusiasm on an interesting and challenging topic made this a very worthwhile endeavour. I would not have been able to complete my studies without his encouragement and helpful supervision.

I made many (too many) friends during my PhD who I would like to thank for all their assistance and friendship throughout. In particular, I would like to thank Dr Javier Cardona for all of his assistance with the simulation work and beyond. His willingness to help and ability to answer even my most inane questions was greatly appreciated. To David, Scott, Alessia, Dorin, Evan, Vitor and many others, thank you for making my studies a very enjoyable time in my life and always making each day interesting.

Finally, I would like to thank my family, particularly my parents who have supported me through all of my decisions, no matter how ridiculous, in my studies and throughout my life. To Carlota, without your support and encouragement I would never have completed this thesis.

Contents

List of Figures

8

13

List of Tables

Publications and Conference Presentations

Publications

Duncan, P; Hatlo M; Lue L.,"A Field Theory Approach for Modeling Electrostatic Interactions in Soft Matter". *Electrostatics of Soft and Disordered Matter* ed Dean, DS et al (Signapore:Pan Stanford). 2013.

Conference Presentations

Duncan P. - March 2014, Open Statistical Physics Conference. Open University, UK. *"Modelling the statics and dynamics of charged colloids in solution"*

Abstract

This thesis studies the electrostatic interactions of ions in solution. This is a well studied but counter-intuitive field with many behaviours which defy conventional theoretical results, mainly as a result of the complexity of modelling the ions and the surrounding systems. Therefore this work endeavours to simplify the theoretical environment by considering ions under purely Coulombic interactions. A further simplification of this model is to consider the ions to be completely penetrable or 'ultrasoft', i.e. the ions can pass through one another, this reduces the complexity of dealing with the excluded volume associated with the non-penetrable or 'hard core' ions. This 'ultrasoft' model is studied using both a variational mean field theory and a virial expansion in the first place and compared to integral equation methods such as the random phase approximation and the Hyper-netted chain theory as well as Monte Carlo (MC) simulations from the available literature. Then molecular dynamics simulations are used to test the model in various situations. The two main systems studied under this model are a symmetric electrolyte consisting of penetrable cations and anions with identical size and charge to one another, and an asymmetric electrolyte consisting of ultrasoft cations and point-charge anions. The Ultrasoft model requires a charge distribution to be defined within the theory, this work has examined both a Bessel and a Gaussian charge distribution for each of the symmetric and asymmetric cases.

The symmetric model shows good agreement with MC simulations from the literature

which allows for more extreme temperatures and densities to be studied. This study reveals like charged clustering at the low temperature-high density limit. The asymmetric model shows analogies with the classical one component plasma as the temperature of the system is decreased and the density is increased. The asymmetric model also shows clustering but it takes a different form to the symmetric electrolyte.

Chapter 1

Introduction

Electrostatic interactions have played a defining role in the behaviour of much of the materials which make up life. All materials gain surface charges when exposed to water, this allows materials to become soluble. However, despite this being a fundamental part of life there is still not a clear understanding of the effect of electrostatic interactions or a clear theoretical treatment. One major example of electrostatic interactions being fundamental to life on earth would be the role played by electrostatics in human DNA. DNA stores large, strongly charged systems in a tight wrapped state which is constantly replicated, repaired and transcribed. Taking this at it's lowest level we see a section of the DNA molecule wrapped twice around a positively charged protein [18]. Experimentally, this packing behaviour is only comparable to a stable system of physiological salt concentrations [19]. These salts govern the electrostatic interactions suggesting that electrostatics can cause this tightly wrapped behaviour.

Another major application of electrostatics in soft matter would be the behaviour of colloids dispersed in aqueous solutions. Colloids are prevalent in industrial applications such as paint dispersion, food emulsions such as mayonnaise or milk which require stability as part of the processes. This stabilisation of colloids against coagulation is achieved

through including permanent charges to the colloids. Understanding how the electrostatic interactions of these charges behave under various conditions is important to the success of these endeavours. These permanent charges which appear in colloids to halt aggregation are achieved either through dissociating behaviour of the colloids or the ability to accept protons in the surface to induce positive charges. This is true for any permanent charges which appear on single molecules, surfaces or interfaces. Therefore, the thermodynamic behaviour of charged systems becomes fundamental to our work.

However, the grand extent of these practical applications have still not led to a complete understanding of the properties of ionic structures. There are many behaviours which remain unexplained even after over 100 years of research. Therefore it is important to be able to model the behaviour of these structures in certain situations, and in particular it is important to understand interactions at a nanoscale level in order to design the manner in which particles self-assemble [20, 21]. When considering the examples detailed above, and indeed any charged system, it is often required to study the surrounding electrolyte. The phenomena described, while complex, can be described using some relatively simple models and theories which display similar behaviour. Much of the current theory on studying electrolytes and electrostatic interactions has roots in the Debye-Hückel theory [22], a simple model of electrolytes developed almost 100 years ago. Electrostatic interactions and a focus on their behaviour in a system is analogous to studying a strongly charged system, meaning it is sensible to ignore all but the Coloumbic interactions. This thesis will focus purely on the electrostatic interactions which occur in systems of ions and will study the field effect rather than the individual particles themselves. This will allow charge distributions and correlation effects to play a major role in the system by effectively controlling the shape of our cations and anions.

The remainder of the thesis is divided into seven chapters, Chapter 2 describes the methods by which electrolytes have been studied in the literature from early electrolyte

studies, moving through the Debye-Hückel theory before introducing the Primitive Model and the variations of this model which exist, leading up to the introduction of the ultrasoft restricted primitive model which will feature greatly throughout this thesis. Then Chapter 3 will introduce briefly the theoretical treatment of electrolytes and the functional integration formation of the partition function before describing several methods used to approximate the partition function. These methods will be used within translationally invariant systems to define the Helmholtz free energy of the ultrasoft model and the thermodynamic properties which may be derived from this. Chapter 4 will discuss Symmetric electrolyes, The Ultrasoft Restricted Primitive model consists of identical penetrable cations and anions. This chapter will use the theory derived in Chapter 3 to analyse this model and in particular the behaviour in the low temperature limit which has been neglected in the literature thus far. Then Chapter 5 will cover Asymmetric electrolytes. The Ultrasoft Asymmetric Restricted Primitive Model differs from the Symmetric model as the cations and anions are permitted to have different size and charge. The thermodynamic behaviour of this model will be discussed as well as the clustering which is discovered as part of this process. The clustering found in the asymmetric model leads to a discussion of the most simple model of an electrolyte system, the one component plasma. In chapter 6, the empirical results of this model are discussed as well as differing approaches to modelling this system. A link between the one component plasma and a system of asymmetric electrolytes is then introduced. The clustering phenomena discovered in the symmetric and asymmetric systems through Molecular Dynamics simulations is analysed in Chapter 7 further to determine the behaviour and validity of these clusters under varying thermodynamic conditions. Finally, Chapter 8 contains a summary of the findings of this work is presented as well as suggestions of possible directions for further study.

Chapter 2

Background

2.1 Overview

This chapter contains a review of the theoretical and simulation work pertaining to the electrostatic properties of ions and charged colloids in solution. First, the history of the study of electrolytes is discussed in Section 2.2, leading to the famous Debye-Hückel theory which will be studied in detail in this work. In Section 2.3, attention is turned to what is currently the most popular model for studying electrolytes; the primitive model (PM) and a variation on that model, the restricted primitive model (RPM). The primitive model consists of ions containing a hard core with a finite size immersed in a dielectric continuum whilst the RPM takes this model but forces the ions to be symmetric in size and charge, thus creating a less realistic, but mathematically simpler system to model. The numerical approaches to studying the RPM will then be detailed to display the early attempts of describing this model. The simulation results of the RPM will be discussed with a view to explaining the phase diagram of the RPM which was not described by the numerical theories.

We then turn our attention to the modified and simplified methods and theories for

modelling the RPM. Up until this point, the systems discussed have all consisted of symmetric electrolytes meaning that the size, charge and other properties of the ions in the system are identical to one another. We will then introduce the idea of asymmetric electrolytes, and the studies thus far which pertain to the RPM. The idea of having different types of ions in a system leads to a discussion of the simplest model of electrolytes the One Component Plasma.

The main focus of this thesis will be on a modified RPM consisting of symmetric ultrasoft ions; the ultrasoft restricted primitive model (URPM). The pioneering works in this model will be discussed in Section 2.4 leading to a novel work on the ultrasoft asymmetric restricted primitive mode (UARPM) and its relevance to the OCP model. The UARPM considers cations and anions with different ion 'size' and charge, leading to a more realistic but complicated system.

Finally, we discuss crystallisation and clustering phenomena in various systems in Section 2.5 to ascertain what conclusions we may be able to make with clustering in the URPM and what the potential applications of these systems could be.

2.2 Electrolytes

In 1887, Arrhenius, expanding upon the previous experimental work of van't Hoff [23] which developed the theory of osmotic pressure of electrolyte solutions, proposed the idea of salts and acids becoming ionised when they are dissolved in water [24]. Therefore, salt will dissociate and form microscopic cations and anions of sodium (Na^+) and chlorine (Cl^-) respectively whilst acids and bases will form ions of hydrogen (H^+) and hydroxide (OH^-), respectively. Arrhenius proposed that, as the cations and anions are distributed uniformly (on average) throughout the system that the average chemical field will be zero (i.e. there will, on average, be no interaction between the ions [6]). This meant that where electrolytes displayed separate thermodynamic behaviour from non electrolytes that this was due to incomplete dissociation of the ions which could be solved through chemical equilibrium. Therefore, this theory treats electrolytes as an ideal gas with no mutual interaction. In this simple picture, an electrolyte is treated as an ideal gas composed of three species, cations, anions, and neutral molecules, whose densities are controlled by the law of mass action. While this theory found success in the case of 'weak' electrolytes such as Brønsted acids and bases, which do not completely dissociate in solution, its predictions did not match the experimental data of 'strong' electrolytes such as $NaCl$ and HCl which completely ionise in solution and therefore conduct electricity well. This led to an understanding that the fundamental mean field theory of Arrhenius required the inclusion of ion-ion interaction to bring the theory more in line with the experimental procedures being carried out at the time.

2.2.1 Debye Hückel Theory

Ten years after Gouy and Chapman [25, 26] first used the Poisson Boltzmann (PB) equation to develop their theory of the electric double layer, Debye and Hückel used a lin-

earised form of the PB equation to develop a theory on strong electrolytes [22] which gave a clearer picture of the problem. Here, the ions in the system were treated as point charges meaning that the charges in the system have no excluded volume but obey classical electrostatic principles. What set this aside from the then current mean field theory was it introduced the idea of strong positional correlations between the cations and anions despite the random distribution of the ions on average. Debye and Hückel considered an electrolyte with volume V consisting N ions, where $N_+ = N_- = N/2$ to satisfy charge neutrality. Here, the solvent molecules of the system are removed and replaced by a dielectric continuum, with a dielectric constant ϵ, meaning that the solvent is treated as a continuous medium. Therefore, the Coulombic interactions are valid as when considering water. Here, the dielectric medium will retain the permittivity of water for aqueous solutions, as described in the McMillan-Mayer theory of solutions [27].

Therefore the internal structure of each ion is ignored and DH theory does not consider interactions between the ion and the surrounding solvent molecules. This makes this a suitable model for systems where the length scales are greater than that of the size of the solvent molecules. With this in mind, the dimensionless length scale used to define the DH theory and much electrostatic studies is the Bjerrum length [28] .

$$l_B = \beta q^2/\epsilon$$

where q represents the ion charge, $\beta = 1/k_B T$. The Bjerrum length is the separation at which the electrostatic interaction between two elementary charges is comparable in magnitude to the thermal energy scale $k_B T$ and is used widely when discussing electrostatic, electrodynamic and electrokinetic phenomena in electrolytes, polyelectrolytes and colloidal dispersions. For example, considering an ion pair that is much closer to one another than the Bjerrum length means that we can essentially ignore the thermal effects as

the electrostatic interaction will dominate. If they are much further apart than the Bjerrum length we can ignore the electrostatics effects. Therefore the Bjerrum length is an important characteristic to frame the study of symmetric electrolytes and electrolytes in general. Water at room temperature, for example, has $l_B = 0.7nm$.   This led to the introduction of the Debye screening length which alongside the Bjerrum length is an important characteristic of the most electrolyte theories. κ^2_{DH} represents the inverse screening length,

$$\kappa^2_{DH} = 4\pi \sum_\eta \beta q^2_\eta \rho_\eta / \epsilon$$

where ρ_η is the ion density and η denotes the ion type (eg cation, anion etc). The Debye screening length is the scale over which mobile charges screen out electric fields in electrolytes and other conductors such as plasmas etc. In other words, the Debye length is the distance over which significant charge separation can occur.   The Debye-Hückel theory (DH) works well in the limit where the thermal energy of the system is larger than that of the average of all interactions [6]. However, the DH theory makes several assumptions which, as the coupling parameter, κl_B, is increased, makes it more important to modify the original theory. It is assumed that there is complete dissociation between the ions in DH theory which is not always the case, particularly with ions of high charge. DH theory also assumes that ions are not polarised and are spherical which does not fit all ions. Finally, DH theory assumes that there are no interactions between the ions and the solvent itself which, in the example of water, ignores the polarizable and dipolar nature of its molecules [29].

2.3   The Primitive Model

What followed the Debye-Hückel theory was an idealised version of a model electrolyte, The Primitive Model, (PM) which describes a mixture of differently sized charged hard

spheres. What is meant by this is a point charge of charge $\pm q$ is at the centre of a hard sphere of diameter $\alpha_\pm$. immersed in a dielectric continuum. Therefore an ion fixed at the origin $r = 0$ will see no other charges in the region $0 < r \leq \alpha$. Therefore the PM strikes a delicate balance between the very far-reaching Coulombic forces and the extremely short-range hard-sphere forces.

This incorporated the classical DH theory for determining the thermodynamic properties of the system but introduced a level of simplicity in the structure of the model which made it applicable to many systems. Despite its simplicity, the model is capable of explaining many experimentally determinable properties of real electrolytes [30, 31], as well as their mixtures [32]. The Primitive Model was not without it's limitations however, one major deficiency was due to the finite sized ions. When studying water molecules of similar dimension to the ions, granularity was observed, i.e. the water molecules were. visible to the charged ions through hydration or simple exclusion. It was also discovered that the repulsive interactions of the hard spheres were not as strong as predicted by the Primitive Model. However, the major issues with the Primitive model was the representation of differently sized hard spheres requiring extensive calculations to resolve the excluded volume effects of these hard spheres. Therefore, much work has focused on a restricted version of the Primitive Model which can reduce the complexity of these calculations.

2.3.1 The Restricted Primitive Model

To achieve quantitative agreement, the Primitive Model would have to be modified or 'restricted' to include an adjustable ionic diameter or a state-dependent dielectric constant. Therefore, the major difference between the this and the PM is that the we now model a symmetric electrolyte, meaning the cations and anions are identical in size and charge. This model is known as the Restricted Primitive Model (RPM) [33, 34] and will form the basis for this work.
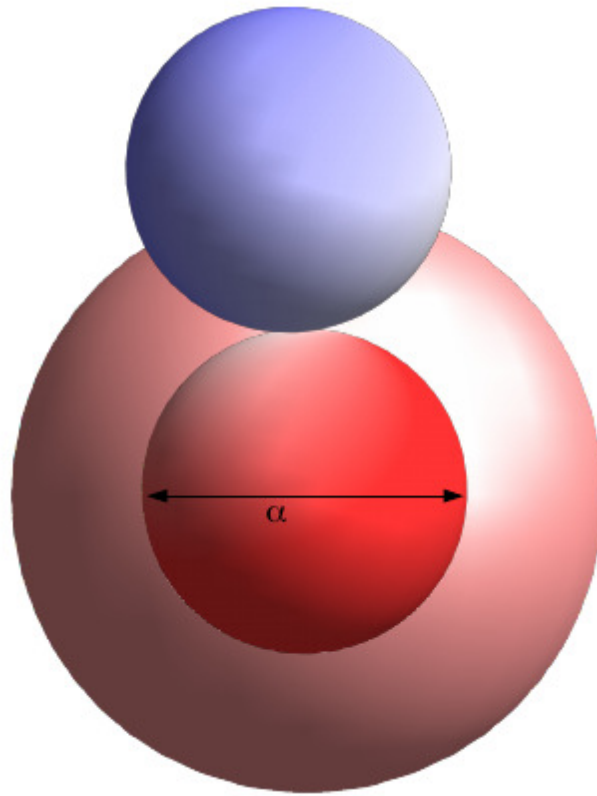
Figure 2.1: RPM configuration of closest approach between two oppositely charged ions (different colours). The impenetrable hard core of the RPM is shown here.

Within this model, shown in Figure 2.1, the ionic fluid consists of point charges surrounded by hard spheres of equal diameter α, half of which carry a charge of $+q$, the other half a charge of q. These spheres are immersed in a continuum of dielectric constant ϵ. This theory requires the ions to be symmetric in terms of ion size, valency, density and charge to ensure electro-neutrality in the bulk electrolyte. The RPM is possibly the most studied model of electrolytes due to it's initial simplicity and success in modelling electrolytes under various conditions.

Firstly, this section will describe some of the main attempts at modelling the RPM thus far, these theoretical approaches take the form of the integral equation theories which defined the early work on the RPM.

While there have been many approaches to studying the RPM, it is widely accepted that the simulation work completed on the RPM is the most accurate representation of the system to date, on par with experimental results and in particular, the simulation methods were the first to predict the phase behaviour of the RPM. The two main simulation methods used to study the RPM have been molecular dynamics (MD) and Monte Carlo (MC) methods with the former being used in this work as a primary modelling tool. MC simulations use random sampling to generate different microscopic configurations of a system which share the same macroscopic state. A Boltzmann factor is applied to each configuration for validity and a weighted average is used for the state of the system. MD simulations solve Newton's equations of motion for each particle in a system of model particles assigned with initial positions and momenta. Then a discrete difference method is used to calculate the new positions and momenta. Each microscopic property of the system is averaged over time to give the macroscopic thermodynamics of the system. The critical behaviour of the RPM under simulation studies will be discussed below in detail.

The remainder of this section will be concerned with modifications to the initial RPM general formalism and theory with particular interest in the Debye-Hückel Hole or Splitting theory as well as asymmetric electrolytes and the phase behaviour of these systems.

Theoretical Approaches

The complicated phase behaviour of the RPM has the constraints of purely consisting of Coulombic interactions and hard-core repulsions. There have been various attempts to model this behaviour through integral equation theories such as the Mean Spherical Approximation (MSA), random-phase approximation (RPA) and Hypernetted Chain theory (HNC).

The RPM is well described by the Debye-Hückel theory when the system is driven by thermal fluctuations. As the coupling parameter, κl_B is increased so do the electro-

static contributions to the DH theory. There are several ways in which this can happen; decreasing temperature (which, in practice, could freeze the solvent), immersing the ions in a solvent with a low dielectric such as oil, increasing the valency of the ions and finally, increasing the density of the ions. The latter uses the diameter of each ion, α, to form the dimensionless packing fraction $\rho\alpha^3$, which defines how close each of the spheres are to one another. As l_B/α (or reduced temperature) becomes very high i.e. $l_B/\alpha >> 1$ then the temperature becomes low and the interaction between two ions is much greater than the thermal energy, making electrostatic fluctuations large. Under these conditions the linearised DH theory and the MSA are able to describe the system well [6]. Coupling this with a low density $\rho\alpha^3 << 1$ can cause the ions to form clusters. This clustering effect is one of the most interesting facets of electrolyte systems and one of the most difficult effects to capture analytically. In the opposite case, when the reduced temperature is low ($l_B/\alpha < 1$) meaning that the system temperature is high and that the electrostatic interaction between two ions is never higher than the thermal energy. The hard spheres which surround the point charges can also influence excluded volume effects which can cause an added complexity to the analytical calculations. As $\kappa\alpha$ increases, the coupling between excluded volume and the electrostatic interactions becomes important. This also plays a factor as the packing fraction tends towards unity. Meaning that the system is completely filled with the hard spheres. Therefore new approaches were required to model to account for these cases.

However, the problem of modelling electrolytes at low temperatures means that these numerical techniques can fall down, particularly when clustering or ion pairing are present. These phenomena are important in understanding critical behaviour and liquid-vapour co-existence in electrolytes [2]. A problem with the HNC is that it will in some cases, inexplicably be unable to produce a result in the ion pairing regime [35] and is known that it does not possess a true critical region. The MSA produces negative radial distribution

functions for low temperatures as a result of the linearisation involved in its development, this cannot occur physically which makes these results difficult to trust. Therefore the AMSA which incorporated ion association has been developed and used to reasonably predict critical density and temperature for charge and size asymmetric system [36].

Whilst the numerical methods struggle to predict criticality in the RPM, they are considered to be excellent methods of modelling simple molecular fluids and were the tools first used to predict correlation-induced attraction between like-charged macromolecules [37–39] and work extremely well for the One-Component Plasma which will be discussed further later in this work. The Ornstein-Zernike equation, which defines the HNC provides a great many closures which work well for different and specific problems, therefore building a general approach using these methods becomes very complex.

Phase Behaviour

The first work to propose a liquid-vapour transition and critical points in the RPM was Vorontsov-Velyaminov et al. [33, 34] using constant-pressure MC simulations they obtained values for the critical temperature, $T_c \approx 0.095$ and critical density, $\rho_c \approx 0.17$. Using equation of state data from simulations and theoretical approximations Stell et al [40] obtained critical values of $T_c \approx 0.085$ and $\rho_c \approx 0.01$. These early studies, whilst quite a distance from the modern values of the critical parameters (see Table 2.1) firmly established the existence of a vapour-liquid transition within the RPM in the low-temperature region. 20 years later Panagiotopoulos [41] discerned critical values of $T_c \approx 0.056$ and $\rho_c \approx 0.04$ using a Gibbs ensemble Monte Carlo simulation with single-ion transfers. This method was adapted to include biased pair transfers by Orkoulas and Panagiotopoulos [42] to obtain $T_c \approx 0.053$ and $\rho_c \approx 0.025$. The Gibbs ensemble has since been proven to be unsuitable in determining phase coexistence [43]

Table 2.1: Critical points for the vapour-liquid transition of the RPM

T_c	ρ_c	Reference
0.0489	0.076	[44]
0.0492	0.062	[45]
0.0490	0.070	[46]
0.04917	0.080	[47]
0.04933	0.075	[48]

Clearly there is an uncertainty in the determination of the criticality of the RPM. There have been many diferent methods used to improve the validity and accuaracy of the simulations. Most liquid-vapour simulation studies of recent times use the mixed field finite-size scaling approach of Bruce and Wilding [49, 50] which assumes that the system is in the three-dimensional Ising universality class, this was proven further by Kim and Fisher [48] who examined the discretization dependence of the critical behaviour and extrapolated this to the continuum limit. The critical parameters of the RPM have been determined by Caillol et al [51, 52] using hyper-spherical boundary conditions, Orkoulas and Panagiotopoulos [46] in cubic boundary conditions Yan and de Pablo [45] used it in combination with hyper-parallel tempering Monte Carlo. Panagiotopoulos [44] obtained the critical parameters of the continuum RPM by extrapolating results on the finely discretized lattice analog to the RPM to infinitely fine discretization. It has been suggested by Kim and Fisher [48] that using the Bruce-Wilding method with no pressure mixing could lead to unreliable estimates of the critical density, but is not likely to result in major errors in the critical temperature.

The phase behaviour of the RPM is also well covered in the simulation studies. Figure 2.2 shows the stages of RPM phase transitions discovered thus far in terms of the packing fraction $\rho\alpha^3$.
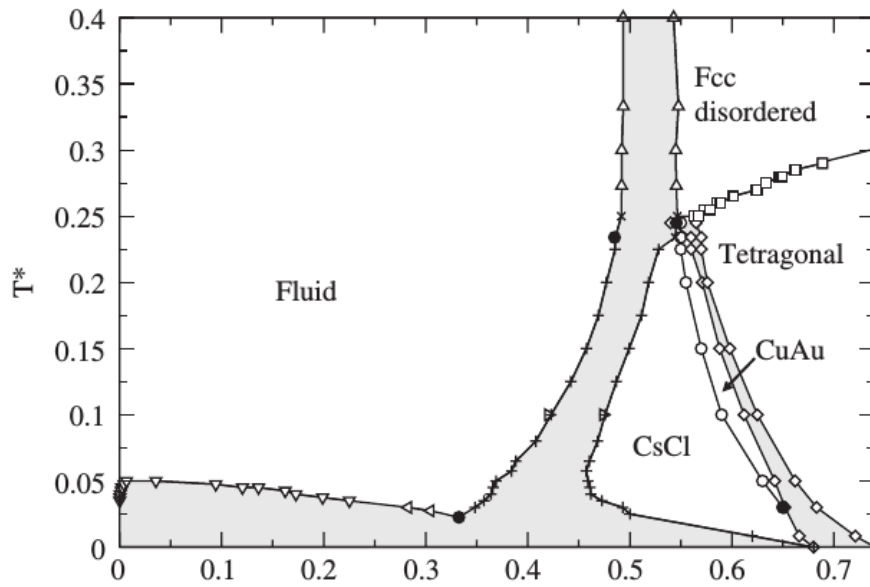
Figure 2.2: Simulation produced phase diagram of the RPM. Figure reproduced from Hynninen et al [1].

The grey areas in Figure 2.2 are coexistence regions of the first order phase transition. Smit et al [53] and Vega et al [54] discovered two regions of liquid-solid crystal transitions in the RPM. Namely, the high temperature limit yielded a disordered liquid-fcc transition while the lower temperatures yielded a liquid-bcc transition. The liquid-bcc transition is seen to take three different forms of the atomic structures $CsCl$ [53, 54], $CaAu$ [1] and a tetragonal fcc solid [55]. These structures are shown in Figure 2.3
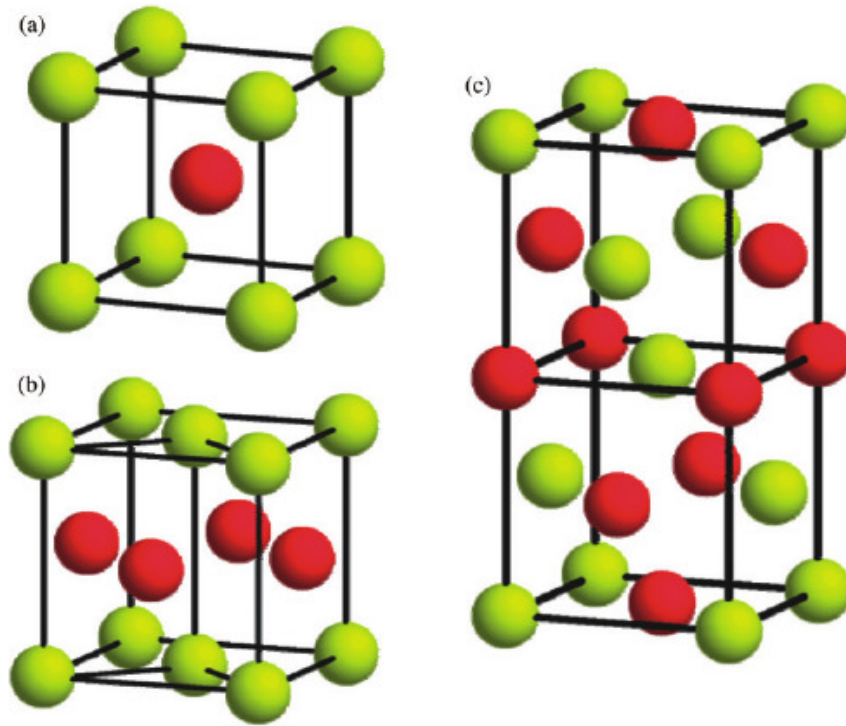
Figure 2.3: Atomic structures seen within RPM simulations. (a) $CsCl$, (b) $CuAu$ and (c) tetragonal structure. Different coloured spheres correspond to opposite charges. Figure reproduced from Hynninen et al [1].

As is seen in the iterative nature of the conclusion of the critical nature of the RPM, there is still much which is left unanswered in the simulation results such as the nature of the phase transitions and the phase behaviour in the high and low temperature limits.

Modified Debye Hückel

There have been several attempts to solve the problem of modelling the low temperature behaviour of the RPM. Mainly these involve making modifications the the existing theory to remove the complexity of the calculations and enable analytical formulae to be developed. Levin and Fisher [2] developed a modified Debye Hückel theory where a portion of the hard spheres have formed Bjerrum pairs. The success of this Bjerrum-Debye-Hückel theory (BjDH) suggests that the RPM consists of a low density of monopoles. For this

36

to be accurately described by the DH theory means that the average distance between the monopoles are greater than the Bjerrum length. All remaining ions in the system have formed dipoles which are highly coupled.
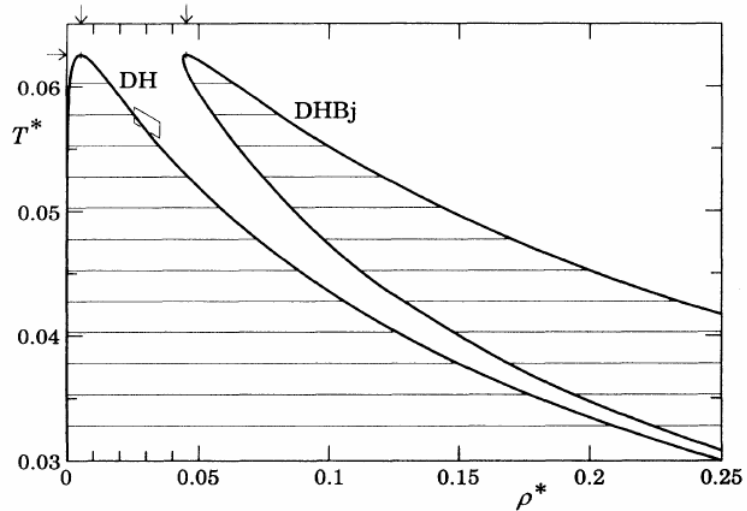
Figure 2.4: Phase diagram for the RPM. Here DH theory has been combined with Bjerrum pairing (DHBj). Figure reproduced from Fisher and Levin [2]

To calculate the number of dipoles in the BjDH theory, the law of mass action is employed. Ignoring the interactions between the individual charges and the dipoles we see the phase diagram of the BjDH (Figure 2.4). Here the BjDH has a non-physical phase diagram at low critical densities.
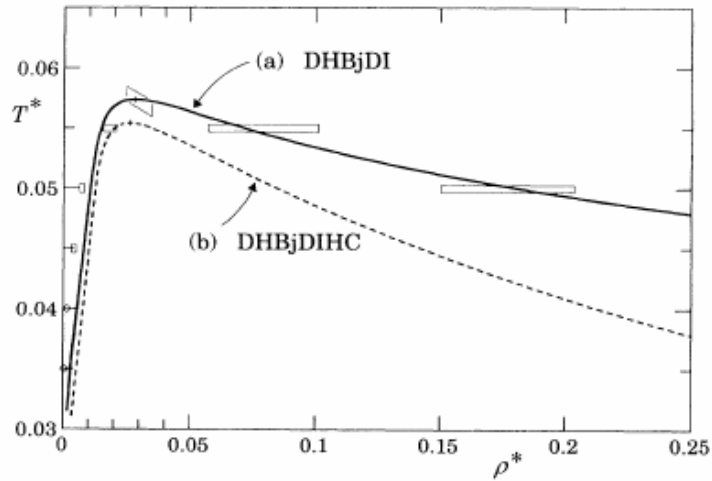
Figure 2.5: Phase diagram for the RPM. Here DH theory has been combined with Bjerrum pairing (DHBj) and dipole charge interactions where (a) and (b) refer to hard core and non hard core interactions respectively. Figure reproduced from Fisher and Levin [2]

There has also been work including the charge-dipole interactions, with and without hard core interactions, the Bjerrum-Debye-Hückel-Dipole theory (BjDHDI) [5] as shown in Figure 2.5. These avoid the non-physical results at low critical densities but overestimates the critical temperatures. However, when these results are compared with the critical temperatures and densities of the Monte-Carlo simulations of Table 2.1 there is an over-prediction of $T_c \approx 0.055$ and an under-prediction of $\rho_c \approx 0.02 - 0.03$. These under predictions are compounded by the Phase diagrams Figures 2.4 and 2.5 not corresponding to the shape of the Monte Carlo phase diagram of Figure 2.2 at higher densities and therefore not predicting the liquid-solid phase transitions in the high and low temperature limits.

Splitting Theory

An interesting approach in modelling electrolytes has been to 'split' the modelling method depending on the strength of the electrostatic interactions between the ions. This method finds its roots in the correlation hole corrected Debye-Hückel theory (CCDH) [56].
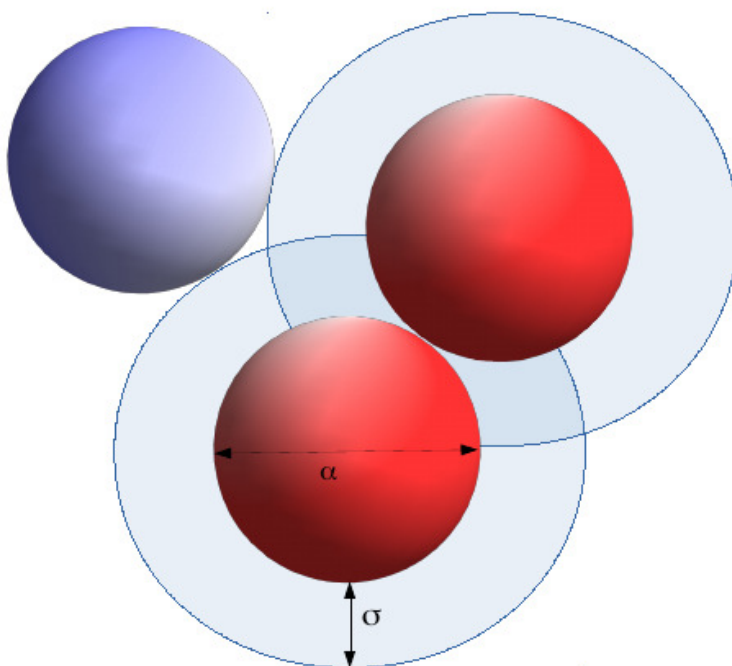
Figure 2.6: Example of correlation hole around an ion repelling oppositely charged (different coloured) ions. The size of the ion and correlation hole are defined by α and σ respectively

This 'correlation hole' is a region around each ion as shown in Figure 2.6 in which it is energetically unfavourable for other ions of like charge to be present. Therefore it is reasonable to split the approaches into treating each area the weak and strong coupling limit. Mean field theories are used in the weak-coupling limit as electrostatic interactions are low and it is reasonable to take averages with respect to the field. However, charge correlations in this limit should not be ignored. Loop expansions were employed by Coalson/Duncan and Netz/Orland [57, 58] to correct the correlation effects in the mean field, here the field is expanded around the classical field ($\psi = \hat{\psi} + \delta\psi$). Other approaches which also assume that the fluctuations in the system can be described by Gaussian statistics include variational perturbation approaches [21, 59–61] where it is assumed that the grand partition function of the system is independent of the screening function $\mathcal{K}$ and the

instantaneous electric potential of the system $i\hat{\psi}$.

When the electrostatic interactions between counterions become significant and the spatial correlation among them becomes large, mean-field approaches break down, and other approximation methods are required. Therefore the strong-coupling expansion [62–64] is employed. In the strong-coupling expansion, the counterions are treated as largely independent from each other due to the mutual repulsions from the highly correlated and distant counterions. The strong interactions of the counterions with the fixed surface charge density are explicitly accounted for, and the weaker ion-ion interactions are added as corrections [63, 65].

This now brings us back to the idea of splitting our approach, the systems covered so far in this section are successful, but only in either the strong or weak coupling limit. If, as mentioned previously, we split the electrostatic potential into the short and long wavelength contributions and treat each with a different approach. [66–72]. Treating the long-wavelength interactions with a mean-field approximation and the short-wavelength correlations with a virial expansion leads to a theory that has been found to work well from the weak to the intermediate and to the strong-coupling regimes for planar geometries. This splitting theory reduces to a mean-field theory for systems with weak electrostatic interactions and to the strong-coupling expansion for systems with very large electrostatic interactions.

2.3.2   Asymmetric Electrolytes

One of the main areas in which the Debye-Hückel theory breaks down is in it's assumption that the cations and anions in question are treated as identical spheres. This doesn't prevent the theory from succeeding in describing many behaviours of electrolytes but leaves an interesting area in which to focus our studies; asymmetry. What is meant by an asymmetric electrolyte in this work is a system composed of cations and anions with different features

between the two. For example, cations and anions may have differing size, charge, density and quantity which can lead to interesting results for the thermodynamic properties such as the free energy, chemical potential or system pressure. As seen in Figure 2.7 and studied further in Chapter 6, a system consisting of smeared charged cations with point charge anions can approach the behaviour of the OCP. This system is known as the UARPM, introduced briefly by Coslovich et al [7, 10].
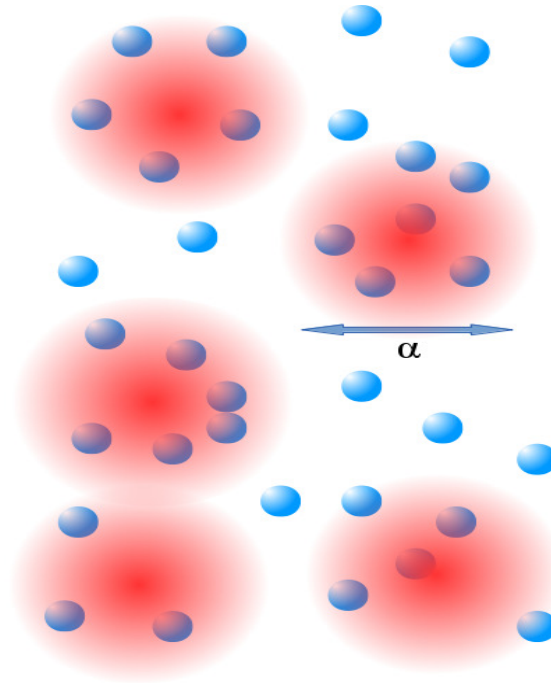
Figure 2.7: A 'size' asymmetric Electrolyte. Smeared charges of diameter α interacting with point charges

However, this is not the first example of an asymmetric adaptation to the RPM. There have been several works which use the hard sphere RPM but vary the ratio of properties such as valency, size, charge etc. The charge symmetry of the RPM plays a crucial role in the determination of its universality class and in the ability to obtain analytic solutions. Therefore changing this symmetry can have a profound effect on the thermodynamic properties as well as the critical points of electrolyte systems. If we initially consider the

charge asymmetric primitive model which is defined as having size symmetry between the ions but varying absolute values for the cations and anions; the MC simulation work of Camp et al and Panagiotopoulos et al [73, 74] have revealed that the critical temperature (T_c) of the system gas-liquid transition decreases as the charge asymmetry grows, i.e. the ratio increases between the charge of the ions. This is considered to be $Z : 1$ where Z is the parameter of asymmetry. It was also noted that as Z increases the critical density ρ_c grows in turn. As noted by Levin [6] there is a great deal of inconsistency in the results for the ARPM, particularly between different calculation methods. Simple Debye-Hückel theory and the mean-spherical approximation do not predict a dependence on the asymmetry parameter Z on the the criticality of the RPM [2, 75]. The mean spherical approximation (MSA), using symmetric PoissonBoltzmann and modified PoissonBoltzmann integral equation methods, was used by Sabir et al [3] to study both size and charge asymmetric electrolytes as shown in Figure 2.8. Two different Poisson-Boltzmann approaches to compute critical parameters were utilised; the reduced critical density ρ_c^* increased with greater size asymmetry, but trends for the reduced critical temperature T_c^* were inconsistent. The inconsistency in these results are further compounded by the field theoretical approach by Netz and Orland [4] which predicts that as the system becomes more charge asymmetric, i.e. $Z \to \infty$ that there will be large increases in T_c and, similarly a large decrease in ρ_c which is contrary to the computer simulation results, even requiring division by a factor of 6 to be included in Figure 2.8. This failure of field theoretic calculations was described by Levin as being 'attributed to their intrinsically perturbative nature'. The hypernetted chain theory was found to have good agreement with an restricted primitive model (ARPM) of valence and size asymmetric electrolytes by Outhwaite et al [76]. The only discrepancies found were for high concentrations of either size or valence asymmetry. It was noted that the modified Poisson-Boltzmann theory used gives similar results to the HNC equation but requires much less numerical effort to produce a solution. Charge

42

asymmetry can also induce an attraction near contact between the lower-valence like ions at high concentrations.

A highly asymmetric model was investigated with regards to the Debye-Hückel-Bjerrum theory for charged colloids by Tamashiro et al [77]. Comparing the cluster density distribution it is observed that as the temperature of the system is decreased the effect of counter-ion condensation is increased whilst the width of the distributions are unaffected by a changing temperature. The system pressure showed no phase transition and was backed up by experimental and MC results. Romero-Enrique et al [78] found a decrease in critical density and temperature as size asymmetry increases which contradicts previous works.

A hard sphere plasma hole corrected Debye-Hückel theory is tested against MC simulations by Penfold et al [79] for both symmetric and asymmetric systems. In general, it had been found that normalised critical temperatures *decrease* with size and charge while critical density will *increase* with z but *decrease* with size asymmetry [80–83]
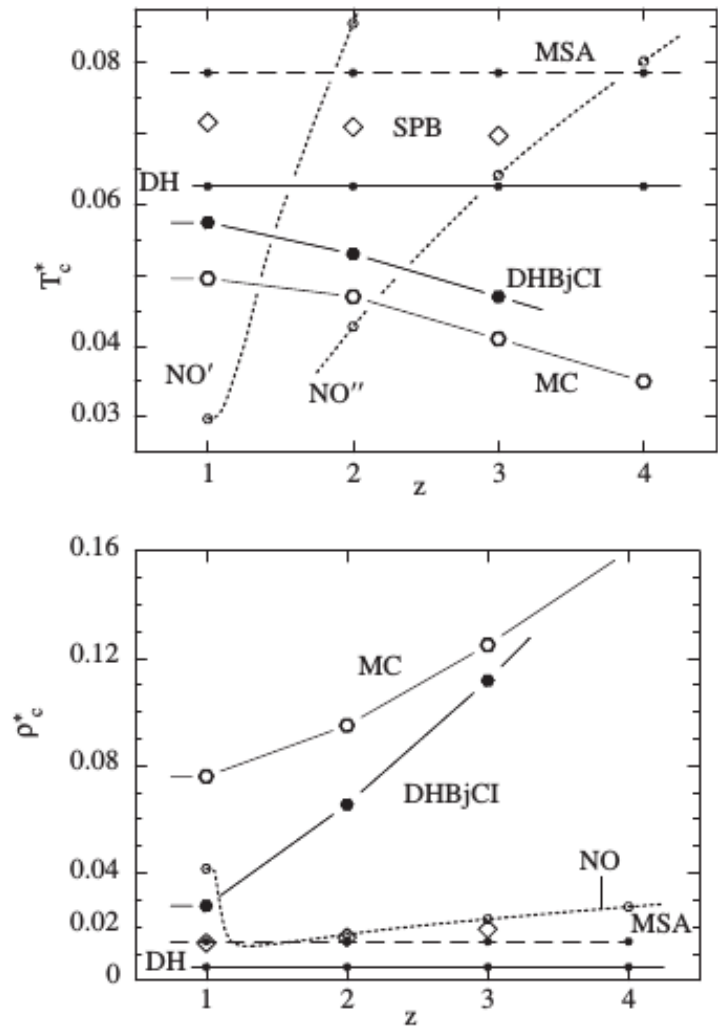
Figure 2.8: Critical Temperatures and densities of a (z:1) charge asymmetric electrolyte. contains predictions of the DH theory, MSA, SPB [3], the Netz-Orland [4] mean field theory (NO' reduced by a factor of 6 and NO" by 12) and the modified DHBjCl theory [2, 5]. Reproduced from [6]

Figure 2.8 shows the difficulty of the Asymmetric electrolyte, field theoretic methods and numerical integral equation methods cannot match the simulation results and vary wildly from each other. Therefore our thoughts turn towards simpler systems. A very simple system, the One Component Plasma (OCP), may be considered a size asymmetric electrolyte if we consider a system of point charges surrounded by a much larger counterion (i.e. as $\alpha \rightarrow \infty$). Therefore, we turn our attention towards understanding the

behaviour of the OCP in order to frame our discussion of asymmetric electrolytes.

2.3.3 One Component Plasma

The one component plasma model is generally considered the simplest example of a Coulomb system [6]. The OCP deals with a large assembly of identically charged ions (eg an atomic nucleus) contained within a rigid neutralizing background of opposite charge so that the overall charge density of the system is electrically neutral [84], there is a simple Coulomb potential between the ions. While this is a simplistic model, this may be used for a number of practical applications including interiors of stars, liquid metals and magnetically confined electrons. The OCP can be used to model interiors of white dwarfs and other compact stellar remnants where crystallisation is an important factor [85]. There is also a link to the classic "Jellium" model of electrons in a solid when we model particles in a positive neutralising background. This classic electron gas was shown by Wigner [86] to form a crystal at relatively low temperature and density in order to minimise the potential energy of the system, whilst in the other limit the OCP will become an ideal Fermi gas at high densities in order to minimise the kinetic energy of the system. The OCP is used as a first approximation to the conduction electron fluid in metals and dense plasmas ignoring the details of the underlying discrete ionic subsystem. A very attractive feature of the OCP is that its physical properties in or near equilibrium can be fully characterized by a single dimensionless parameter, the so-called "Coulomb coupling parameter", Γ, defined as

$$\Gamma = l_B/a = \left(\frac{4\pi}{3}\rho l_B^3\right)^{1/3} \tag{2.1}$$

where, $a = (3/4\pi\rho)^{1/3}$ is the Wigner-Seitz radius which determines the mean spacing between the ions, $\beta = (k_B T)^{-1}$. Γ measures the level of non-ideality of the system, i.e. the degree to which many-body interactions affect the properties of the ensemble

of particles or the strength of electrostatic interactions in the system. By varying Γ, the OCP exhibits the various faces of strong coupling effects on the plasma properties. As Γ increases, the OCP displays a transition from a nearly collision-less, gaseous regime for $\Gamma << 1$ continuously through an increasingly correlated, liquid like regime before an isochoric freezing transition into a body-centred cubic Wigner crystal in the region, $\Gamma = 172 - 178$ [15, 16]. At low Γ, particles configurations are highly disordered and particles undergo only occasional binary collisions. Baus and Hansen [87] showed that for $\Gamma > 3$, the isothermal compressibility and pressure of the OCP become negative. Increasing the coupling parameter causes the mobile ions to pull upon the rigid background which is a possible reason for this asymptotic behaviour. The pair distribution function $u(r)$, which characterizes the modulation of the local density around a given particle as a function of the distance from this particle, is smooth, and rapidly vanishes for small r because of the repulsions between the particles. This structure is characteristic of a dilute gas phase. As the coupling Γ increases, positions of neighbouring particles are more and more correlated, leading to a modulation of $u(r)$ extending over a few inter-particle distances. This short-range order is characteristic of the liquid phase. The minima may be associated with shells of neighbours, but the oscillations are rapidly damped, showing the gradual smearing out of short-range order. At $\Gamma = \Gamma_m$, the short-range order grows spontaneously into full long-range order, characteristic of a periodic crystalline structure.

Chapter 6 will investigate the OCP in more detail. In particular, the relationship between the OCP and the splitting theory and eventually the ultrasoft electrolyte model.

2.4   Ultrasoft Restricted Primitive Model

Just as the RPM simplifies the PM by restricting the PM to symmetric ions, there have been other attempts at reducing the complexity of the calculations, in particular the excluded

volume interactions of the hard spheres which become important as the packing fraction is increased and the ions in the system become much closer together. This theoretical difficulty with the RPM has been considered by Ruelle et al [88]. Here, the proximity of the hard spheres when the dipolar pairs propagate the system causes leads to the spheres collapsing on top of one another and forming infinitely strongly bound ion pairs. Therefore, as shown in Figure 2.9 the interaction potential between the component ions of the dipoles diverges as the distance between each particle, r, tends towards zero.
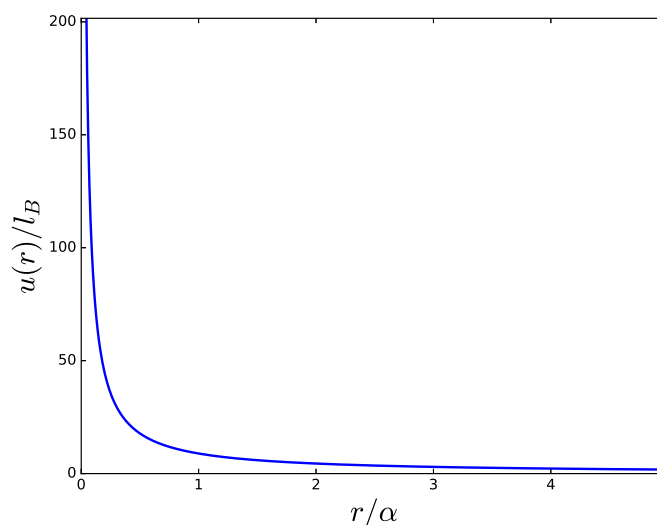
Figure 2.9: Interaction potential between two hard spheres as $r \to 0$

To solve this divergent interaction and to determine the behaviour of the RPM at $r \to 0$, the idea of replacing the hard cores which surround the point charges with a 'charge cloud'. This is achieved by effectively *smearing* the charges out over a distance comparable to the soft sphere repulsion radius. Figure 2.10 shows the comparative interaction potential, note that as $r \to 0$ the divergent nature of the hard spheres is replaced by a smooth cut-off. This is due to the smeared charges being completely penetrable which leads to this model being called the Ultrasoft Restricted Primitive Model (URPM). The form of the charge cloud does not have a physical significance and is purely chosen due to it's compatibility with

47
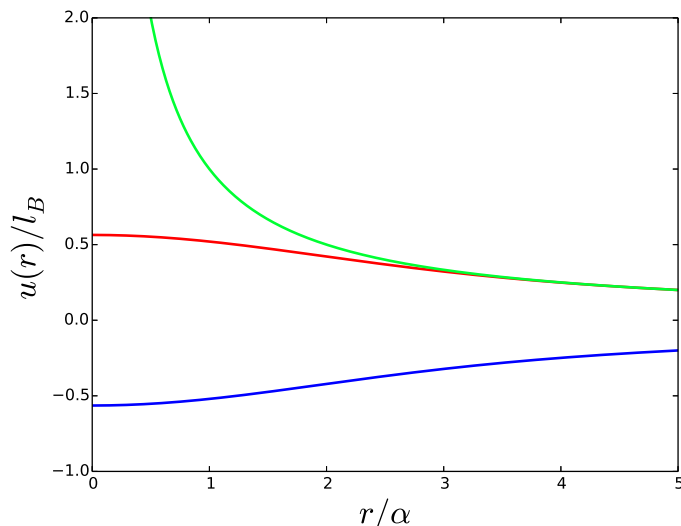
Figure 2.10: Interaction potential between: (i) two cations (red line), (ii) two anions (green line), and (iii) a cation and an anion (blue line).

computational methods, therefore there have been several different forms of charge cloud suggested; Dissipative particle dynamics (DPD) have been adapted to model electrostatic interactions by Groot where a particle-particle mesh method with linear charge smoothing was investigated [89]. It was noted that at short distances, numerical artefacts are observed in the ion-ion force, possibly due to the size of the grid used. This could be rectified by using a smaller grid but not without some CPU costs. The DPD simulations are seen to be much faster than Molecular Dynamics simulations of similar systems. Following on from the work of Groot, Gonzalez-Melchor et al [90] replaced the particle mesh and employed an Ewald sum method with exponential charge smoothing. To avoid the formation of artificial ion pairs Gonzalez-Melchor et al assign charge distributions to charged DPD particles. It is predicted that by employing fast Fourier transform techniques, this method could improve it's calculations in reciprocal space. The results were in general agreement with the work of Groot without ignoring the short range ion-ion effects. In their 2011 papers, Coslovich, Hansen and Kahl discussed the aggregation, phase separation and dy-
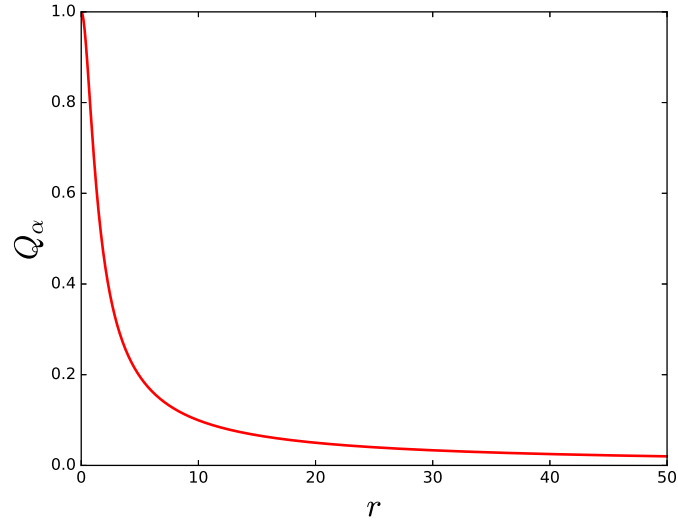
Figure 2.11: Gaussian charge distribution

namics of a polyionic URPM [7, 10]. Here, a system consisting of Gaussian smeared charges (see Fig 2.11) whereby the charge around the centre of mass of each macro-ion is described by a Gaussian distribution, it is also suitable to choose other distributions such as a Bessel distribution.

Coslovich et al use both MD and MC simulations to describe this system and are able to see marked clustering at sufficiently low temperatures and densities which is a similar effect to the experimental results of complexation of ionic polyelectrolytes [91, 92]. It is found that the URPM phase separates into a dilute phase of dimers and a concentrated phase of unpaired ions below a certain temperature. This allows the conductor/insulator transition to be determined as well as the liquid vapour coexistence transition as shown in Figure 2.12.

Increasing the density, ρ of the URPM leads to the introduction of the dimensionless packing fraction $\rho\alpha^3$ where α is the size of the ion charge cloud. As $\rho\alpha^3$ tends towards unity, the charge clouds begin to overlap one another. This is because increasing the density will effectively increase the electrostatic interactions between the ions by pushing

49

them closer together. This is a marked difference from the RPM as the penetrable core means that excluded volume effects are not as important in the URPM.
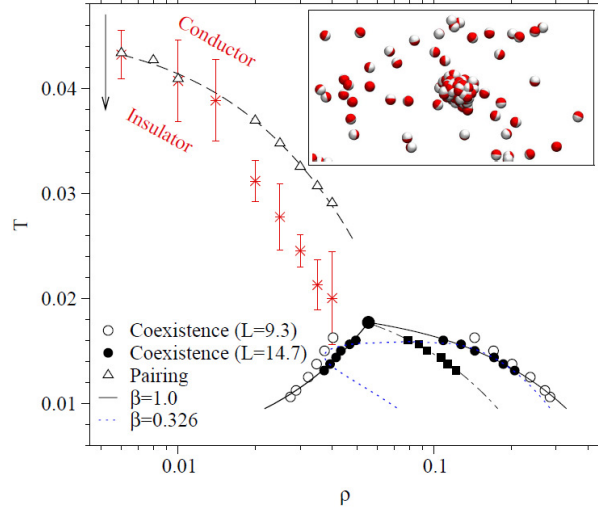
Figure 2.12: Extended phase diagram of the URPM: Figure reproduced from [7]

The URPM is studied further by Nikoubashman et al [93] who found that, unlike the RPM, the mean field theory approach does not match the simulation data of Coslovich et al [91, 92] for the URPM where mean field theory predicts a much higher critical density and a much lower critical density. Possible reasons for this discrepancy are described as a problem in the linearisation of the Poisson-Boltzmann theory, double 'counting' of the Coulombic interactions of oppositely charged polyions, excluding tetramers in the mean field approach and most likely the nature of the URPM where only Coulombic interactions are included. Therefore, whilst the MD simulations can account for the many-body nature of the ion-pair and pair-pair interactions, the strong fluctuations make a mean field theory a non-trivial undertaking.

The URPM has led to a simplified Ewald sum method with Gaussian smeared charge smoothing.[12]. It is noted that the URPM shows marked clustering at values of the dimensionless coupling constant $l_B/\alpha \geq 30$ and a condensation transitions at $l_B/\alpha \geq 100$

for densities in the range $\rho\alpha^3 \approx 0.01 - 0.1$ where α refers to the size of the Gaussian charge cloud and ρ is the total ion density. This model is well predicted by the HNC approximation for $l_B/\alpha = 1, 10$ but lower temperatures have remained unstudied thus far to avoid approaching the point charge limit and any numerical artefacts incurred, i.e. $l_B/\alpha \leq 30$.

Heyes and Rickayzen compare the results of MD, Ornstein-Zernike (OZ) integral equation with the mean spherical approximation (MSA) and the hypernetted-chain (HNC) closures [8]. It is found that if the size of the charge distribution, α, is high enough then the radial distribution functions of the MD and HNC methods are fairly agreeable whilst MD and HNC methods are in agreement for values $\alpha/l_B \approx 1$. Figure 2.13 shows the structural changes which occur within the ionic fluid as the size of the charge spread is changed. It is observed that dimers are being formed as the value of α is decreased.
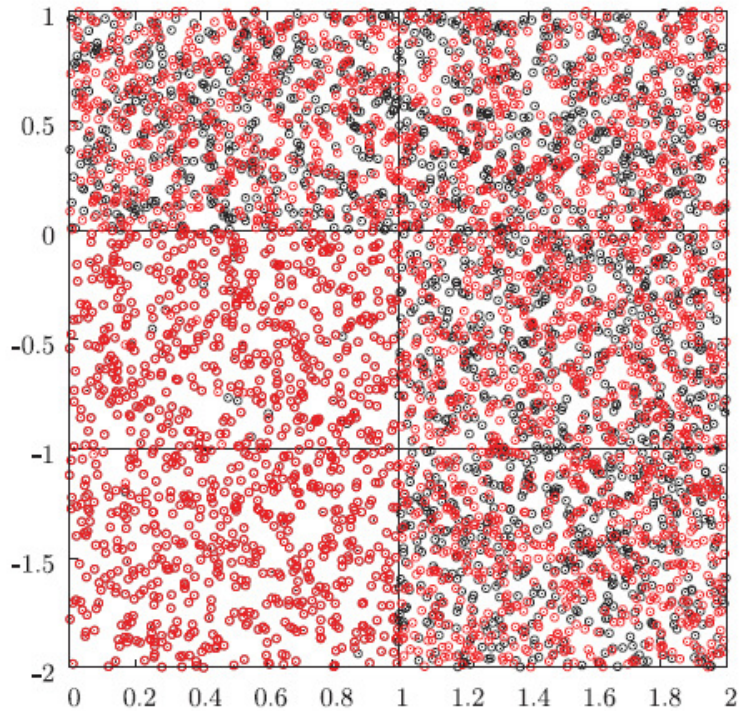
Figure 2.13: Snapshot projections of the $+$ and $-$ CD coordinates generated by MD simulations. The black and red discs are projections of the centres of the oppositely charged particles onto one of the faces of the MD simulation cell wall. Key: From top to bottom on the left- and right-hand sides, $(a)\alpha D = 1$, $(b)\alpha D = 70$ and $(c)\alpha D = 150$, where $\alpha D = 1/2\alpha$. The left-hand three frames are for the state points $\xi = 1.0$ and the reduced temperature $T = 1$. The three right-hand frames are for $\xi = 1.0$ and the reduced temperature $T = 10$. The distance unit in the x and y directions is based on the side length of the MD cell being equal to unity. Note that for the small α (the two bottom left frames), the black circles are hidden by the red ones, as in these states substantially overlapping dimers form.[8]

A MC study of the URPM has been carried out by Caillol and Levesque [9] who determine the chemical potential, critical temperature and density of the Gaussian smeared charge model for four different volumes. It was found that the size of the critical temperature decreases as the volume of the system increases whilst the reverse is true for the critical chemical potential and critical density. This is shown in Figure 2.14
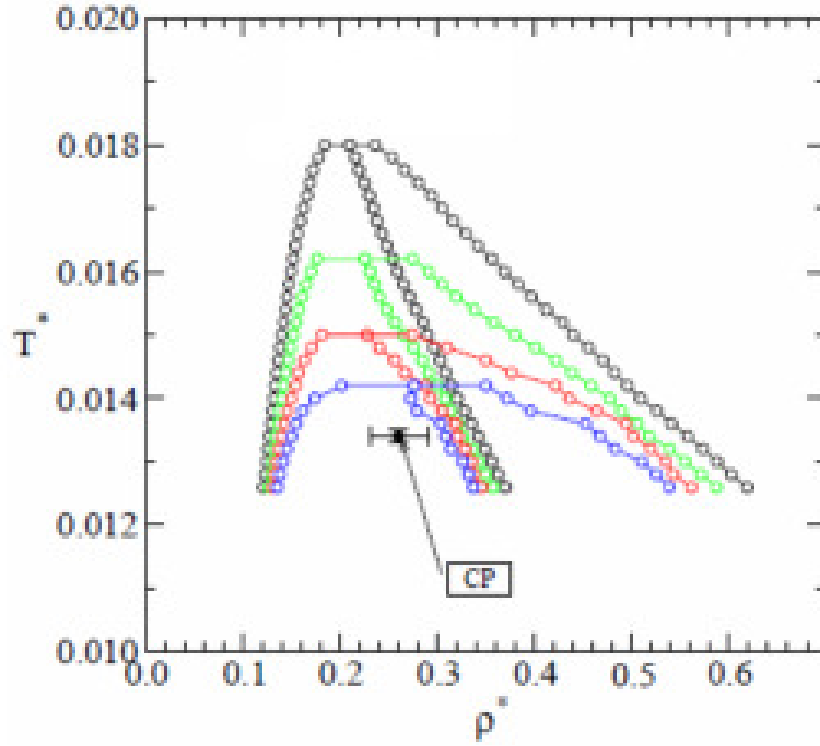
Figure 2.14: Coexistence curves $\rho_g(T*)$ and $\rho_l(T*)$ for the volumes $V* = 500$ (black),$V* = 1000$ (green), $V* = 2000$ (red), and $V* = 4000$ (blue). We also display the curves $(\rho_g(T*) + \rho_l(T*))/2$ which roughly satisfied the law of rectilinear diameters[9]. Solid circles : estimates for the critical points from Coslovich et al. Taken from [10]

In recent years there has been an encouraging increase in studies of the RPM and symmetric electrolytes. Not least the introduction of smeared charges and the ultrasoft restricted primitive model [7, 10], however work on this model is still in its infancy. One model which has been richly studied since its inception is the One component plasma which can provide useful analogies to the URPM.

Ultrasoft Asymmetric Restricted Primitive Model

Whilst the current theoretical treatment of asymmetric electrolytes has been relatively sparse compared to that of symmetric electrolytes, there are still interesting works being considered [94, 95]. However, with most work being carried out on hard sphere models it is difficult to relate this to the as yet unapproached ultrasoft model. Coslovich et al [7, 10] introduced briefly the idea of the UARPM whereby the ultrasoft model would undergo a similar treatment as the ARPM described above. Coslovich et al begins the mathematical approach to the system but as of yet the ultrasoft model remains unstudied.

Chapter 5 aims to investigate the UARPM in more detail and to use the Splitting theory to determine a previously undescribed version of the ultrasoft RPM.

2.5 Crystallisation and Clustering

As shown in Figure 2.2, as the RPM increases density, it enters into a crystalline phase. This phase takes differing forms depending on the temperature of the system going from an unstructured fcc phase to the atomic forms shown in Figure 2.3. The OCP also shows an isochoric freezing transition into a bcc Wigner crystal as the coupling parameter Γ is increased. This section will define some of the crystallising or clustering effects which are common in this type of crystallisation shown in the RPM and OCP systems. Firstly, the types of crystallisation will be defined.
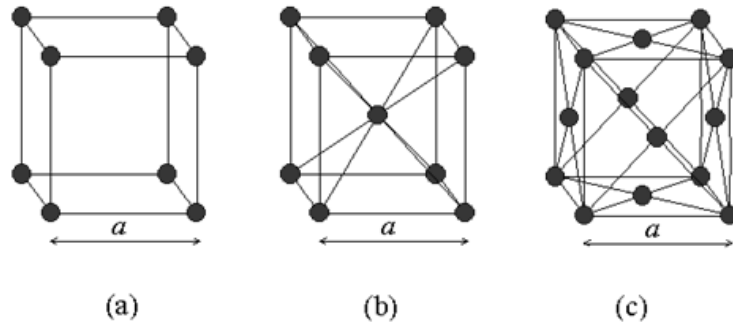
Figure 2.15: Structure of different types of crystallisation. The different structures are defined as (a) Simple cubic, (b) body-centred cubic (c) face-centred cubic

In a crystal structure, the arrangement extends over millions and millions of atoms. Here we consider the unit cell, the smallest unit that, when repeatedly stacked together, will generate the entire structure. As shown in Figure 2.15 there are 3 main crystalline structures; the simple cubic (sc) body-centred cubic (bcc) and face-centred cubic (fcc), we will focus on the fcc and bcc for brevity. The bcc unit cell has one lattice point in the centre of the unit cell in addition to the eight corner atoms. Each of the corner atoms is the corner of another cube so the corner atoms are shared among eight unit cells. At room temperatures, elements Li, Na, K, Rb, Ba, V, Cr and Fe have structures that can be described as body centre cubic (bcc) packing of spheres.

The fcc unit cell has lattice points on the faces of the cube, that each gives exactly one half contribution, in addition to the corner lattice points, giving a total of 4 lattice points per unit cell. Many of the technologically most important metals possess the fcc structure such as the catalytically important precious metals Pt, Rh and Pd.

Wigner Crystal

In 1934, Wigner [86] found that in the presence of a positively charged neutralising background, a system of electrons will crystallise in the low density limit. This has led to a wealth of work into the one and three dimensional 'Wigner crystals' [96]. This is one of

the most commonly studied examples of a bcc crystal. Shklovski [97] found that due to the cohesive energy of the Wigner crystal, a bundle of parallel rods can be considered as a uniform negative background at which condensed ions form this crystal. It was seen that the rods self assemble due to a binding energy being formed from narrow contact stripes where rods pairwise contact each other and allow their Wigner crystals to overlap, therefore creating a bundle. This theory was adapted for hard spheres where, for a large enough sphere, the 2D Wigner crystal is formed at its surface. Here, the binding energy which causes two spheres of radius r to bundle together originates from a contact disc with radius $(rR)^{1/2}$ where R is the lattice constant for the Wigner crystal. The aggregation of rigid 'rodlike' polyelectrolytes has been studied in depth for a range of biopolymers [98–111]. Tang and Lyubartsev [100, 105] showed that for negatively charged rodlike polyelectrolytes, the hydrated sizes of the multivalent cations influence their function of an aggregating agent. The point-like ions are assumed to neutralise the charge of the rodlike polyelectrolyte completely whilst the large ions have steric hindrance in the packing, which prevents charge neutralisation of the polyelectrolyte [98]. It has also been reported that a slight difference in the surface charge density of negatively charged rodlike polyelectrolytes influences its condensation with positively charged multivalent ions [106].

2.6 Summary

This work in this chapter presents the general theory of modelling electrolytes, from the first mean-field theory of Arrhenius through to the modern numerical and simulation techniques. The initial difficulties of this model in describing 'strong' electrolytes are discussed leading to the discovery of the famous Debye-Hückel theory which allowed electrostatic interactions between the ions in the system. The Primitive Model which was built upon the Debye Hückel theory is introduced leading to the centrepiece of the chapter; the Restricted Primitive Model. The restricted primitive model is a remarkably successful model considering the simplicity of its initial structure. The phase behaviour of the RPM was discussed including a description of the transitions from vapour-liquid-crystalline solid. The RPM is, however, not without its limitations. Difficulty in producing an analytical framework and numerical approaches for the RPM has lead to many modified approaches designed to address specific problems. These include the Modified Debye-Hückel theories which add characteristics to the DH theory such as the system ions forming Bjerrum pairs. Other modifications to the RPM include the Splitting theory which splits the mathematical approach into a strong and weak coupling component. Versions of the RPM with size and charge asymmetry yielded uncertain results in both simulation and numerical studies leading to a consideration of the One-component plasma, one of the simplest models of electrolytes. An interesting approach to the limitations of the RPM concerning the hard spheres was discussed. The URPM removes the hard spheres and replaces them with a smeared charge distribution. The literature on this topic is still in its early stages so the URPM will be covered in great detail in the remainder of this thesis.

We now introduce the mathematical theory on which much of this sections results have been built which will lead us towards an analytical approach which will be used throughout the remainder of this thesis.

Chapter 3

Theory

3.1 Overview

In this chapter, the theoretical framework which will be used in this thesis is introduced, as well as the background to the expressions. We begin by defining the system used throughout this work. The remainder of this chapter will detail the governing electrostatics before defining the mean field approach and the grand partition function. This leads to the definition of the Helmholtz free energy through the partition function and a discussion on ways to approximate the partition function. This work previously exists in the available literature but our main goal is to develop a unique analytical approach to the pre-existing theory. Once we have used the partition function to determine a form for the Helmholtz free energy of the system we will use a Fourier transform to adapt this for a translationally invariant system which will form the unique part of the theoretical framework. From here we can use Equations 3.3 and 3.4 to determine a final Free energy, electrochemical potential and pressure for the URPM which we will apply is subsequent chapters.

3.2 System Definition

We consider a system of mobile particles with an extended charge distribution which are immersed in a spatially varying continuum dielectric $\epsilon(\mathbf{r})$ as a result of the possible presence of a solvent. The identical mobile particles consist of cations and anions with a net positive and negative charge respectively, carrying a charge of magnitude q. The number density of the ionic particles may be written as $\rho = \rho_+ + \rho_-$ due to the global charge neutrality of the system where $\rho\pm$ is the density of the cations $(+)$ and anions $(-)$. The absolute temperature of the system is T, the chemical potential of ion species η is γ_η (in units of $k_B T$ with k_B being the Boltzmann constant.) The defining nature of the ultrasoft model is the 'smearing' of the charges over a certain charge distribution. The charge distribution of a particle of type η that is located at the origin and is in an orientation $\boldsymbol{\Omega}$ is $Q_\eta(\mathbf{r}, \boldsymbol{\Omega})$. In addition, there may also be a fixed background charge $\Sigma(\mathbf{r})$. The system volume is V and thermal averages will be written as $\langle \cdots \rangle$. The properties which govern the model are the length scales α and l_B referring to the size and Bjerrum length of the ions as well as the densities $\rho_\pm$.

The goal for this section is to develop an expression for the Helmholtz free energy F which is defined as a function of the state of a system specified with the independent variables T, V and N_η which describe the temperature, volume and number of each species η respectively. This is defined by Prigogine and Defay [112] as

$$dF = -SdT - PdV + \sum_\eta \mu_\eta d\rho_\eta \tag{3.1}$$

where μ_η defines the electro-chemical potential of ion species η. Equation 3.1 may also be written as

$$\beta F = \ln Q \tag{3.2}$$

59

where $\ln Q$ is the canonical partition function of the system. Further details of the partition function can be found in Section 3.4. Once the Helmholtz free energy is obtained we are able to determine forms for the pressure and chemical potential of the system via

$$\mu_\eta = \left(\frac{\partial F}{\partial \rho_\eta} \right)_{V,T,\rho_\eta \neq \nu} \tag{3.3}$$

$$P = - \left(\frac{\partial F}{\partial V} \right)_{\rho_\eta,T} \tag{3.4}$$

where the subscripts indicate the properties which are treated as constants when taking derivatives.

This work will be primarily concerned with ultrasoft electrolytes as described in Section 2.4. This system contains size and charge identical smeared charges immersed in a dielectric continuum.

3.3 Electrostatics

This section will provide a brief introduction to the electrostatics which will be used in this work. We will be using the Gaussian system of units [113]. Beginning with the Maxwell equations for electrostatic fields, we first discuss the fundamental equation which governs electrostatics. The Poisson equation relates the electric field $\mathbf{E}(\mathbf{r})$ to the total charge density $q_{tot}(\mathbf{r})$. This gives the following equation

$$\nabla \cdot \mathbf{E}(\mathbf{r}) = 4\pi q_{tot}(\mathbf{r}) \tag{3.5}$$

We may obtain the macroscopic version of Poisson's equation, which relates the gradient in the electric field to the charge density at a point, as

$$-\frac{1}{4\pi}\nabla \cdot (\epsilon \nabla \psi(\mathbf{r})) = q(\mathbf{r}) \tag{3.6}$$

by writing the electric field as the gradient of a scalar function

$$\mathbf{E}(\mathbf{r}) = -\nabla \psi(\mathbf{r})$$

and inserting this into Coloumbs law where $\psi(\mathbf{r})$ is the electrostatic potential. We may write a general solution to this is given as

$$\psi(\mathbf{r}) = \int d\mathbf{r}' G_0(\mathbf{r}, \mathbf{r}') q(\mathbf{r}') \tag{3.7}$$

where $G_0(\mathbf{r}, \mathbf{r}')$ is the Green's function.

Physically, $G_0(\mathbf{r}, \mathbf{r}')$ is the electrostatic potential at a position $\mathbf{r}$ due to a unit point charge located at $\mathbf{r}'$; it dictates how the electrostatic potential emanates from a charge.

Mathematically we obtain the Green's function as a solution to the equation

$$-\frac{\epsilon}{4\pi}\nabla^2 G_0(\mathbf{r}, \mathbf{r}') = \delta(\mathbf{r} - \mathbf{r}') \tag{3.8}$$

The total charge distribution from Equation 3.5 contains both the bare charges $q(\mathbf{r})$ and charges induced by the presence of an electric field $q_{ind}(\mathbf{r})$. The presence of an electric field induces a dipole on the background solvent where the dipole moment density is given as $\mu_{ind}(\mathbf{r}) = X \cdot E(\mathbf{r})$ and $\epsilon = 1 + 4\pi X$. Therefore we may describe the charge density associated with a dipole moment density as

$$q_{ind}(\mathbf{r}) = -\nabla \cdot \mu_{ind}(\mathbf{r})$$

Therefore we may write the total charge distribution as

$$q_{tot} = q(\mathbf{r}) + q_{ind}(\mathbf{r})$$

3.3.1 Energy of the Electric Field

A main goal of this work is to determine the total energy of a collection of charge distributions. The total energy is defined as the work required to assemble the charges of the system. The force felt by a charge q in an electric field is given by Jackson [113] as

$$\mathbf{F} = q\mathbf{E}$$

The work δW to move an infinitesimal charge δq from an initial position $\mathbf{r_0}$ to a final position $\mathbf{r}$ is give by the following integral where we have set $\psi(\infty) = 0$

$$\begin{aligned}
\delta W &= \int_{\mathbf{r_0}}^{\mathbf{r}} d\mathbf{X}.\mathbf{F} \\
&= \int_{\mathbf{r_0}}^{\mathbf{r}} d\mathbf{X}.\mathbf{E}\delta q \\
&= -\int_{\mathbf{r_0}}^{\mathbf{r}} d\mathbf{X} \cdot \nabla\psi\delta q \\
&= \delta q[\psi(\mathbf{r}) - \psi(\mathbf{r_0})]
\end{aligned}$$

For a general charge distribution we use the following formula

$$W = \frac{1}{2} \int d\mathbf{r} q(\mathbf{r})\psi(\mathbf{r})$$

We determine the influence of the dielectric constant to account for charges in a complex background by making the property ϵ represent the response and effect of all the charges on the solvent molecules. We may now write δW as

$$\delta W = \int d\mathbf{r}\delta q_{free}(\mathbf{r})\psi(\mathbf{r})$$

We may rewrite the above as

$$\delta W = \frac{1}{4\pi} \int d\mathbf{r}\{\nabla \cdot \delta[\epsilon(\mathbf{r})\mathbf{E}(\mathbf{r})]\}\psi(\mathbf{r})$$

Integrating by parts we get the following

$$\begin{aligned}
W &= \frac{1}{8\pi} \int d\mathbf{r}\mathbf{E} \cdot (\epsilon\mathbf{E}) \\
&= \frac{1}{8\pi} \int d\mathbf{r}\epsilon(\mathbf{r})|\nabla\psi(\mathbf{r})|^2 \quad\quad\quad (3.9)
\end{aligned}$$

63

We may now discuss the idea of a *free energy* which occurs in the presence of a dielectric medium (where $\epsilon \neq 1$). We may rewrite the above equation for the energy of the electrostatic field by incorporating Equations (3.6), (3.7) and (3.9) to give

$$W = \frac{1}{2} \int d\mathbf{r} d\mathbf{r}' q_{free}(\mathbf{r}) G_0(\mathbf{r}, \mathbf{r}') q_{free}(\mathbf{r}')$$

Here, our Green's function determines the free energy of the electrostatic field. The above equation also introduces us to the self energy which is defined as the contribution to the systems energy due to interactions between the particle, here our charge, and the system it is part of, the self generated electric field. For a point charge of magnitude q located at position $\mathbf{r}$, our self energy e_{se} is given as

$$e_{se} = \frac{1}{2} q^2 G_{free}(\mathbf{r}, \mathbf{r}')$$

The self energy contributes a constant, infinite value to the electrostatic energy of the system which is then subtracted from the total electrostatic energy to allow for calculations. The electrostatic energy between two point charges, one of magnitude q located at $\mathbf{r}$ and the other of magnitude q' located at $\mathbf{r}'$ in a medium with a uniform dielectric constant ϵ is given by

$$W = qq' G_{free}(\mathbf{r}, \mathbf{r}')$$
$$= \frac{qq'}{\epsilon |\mathbf{r} - \mathbf{r}'|}$$

3.4 Statistical Physics of Electrolytes

After developing the general electrostatic theory in the previous section, we must now adapt this to the Statistical Physics method of ensemble averaging of the studied system.

Statistical Physics takes the macroscopic thermodynamic properties of the microscopic interactions and displays them as averages of the functions of the state. This average is taken as a system of N particles is a function of $6N$ parameters due to the N position and momentum values in three dimensions. Taking systems in thermodynamic equilibrium means taking the macroscopic averages to be independent of time in the microscopic state. The Hamiltonian of a model system is used to obtain an expression for the previously mentioned partition function [114]. We begin by determining the charge distribution of the system. The total electrostatic energy of the system is

$$E_{\text{elec}} = \frac{1}{2} \int d\mathbf{r} d\mathbf{r}' \mathcal{Q}(\mathbf{r}) G_0(\mathbf{r}, \mathbf{r}') \mathcal{Q}(\mathbf{r}')$$

where G_0 is the Green's function of the Poisson equation as defined above

$$-\frac{1}{4\pi} \nabla \cdot [\epsilon(\mathbf{r}) \nabla G_0(\mathbf{r}, \mathbf{r}')] = \delta^d(\mathbf{r} - \mathbf{r}'),$$

and $\mathcal{Q}(\mathbf{r})$ is the total charge density of the system

$$\mathcal{Q}(\mathbf{r}) = \sum_{\alpha,k} Q_\alpha(\mathbf{R}_{\alpha,k}, \mathbf{\Omega}_{\alpha,k}) + \Sigma(\mathbf{r}),$$

where $\mathbf{R}_{\alpha,k}$ and $\mathbf{\Omega}_{\alpha,k}$ are the position and orientation, respectively, of the kth particle of type α. Formally, the grand partition function of this system can be written exactly as an integral over all the positions and orientations of the particles in the system [114]; however, the direct evaluation of the resulting integral is intractable for most systems. This allows all of the static properties of an equilibrium system to be determined from the one function. This not only includes thermodynamic properties such as phase behaviour but also the actual structure of the system such as the pair correlation functions.

Liquid state approaches to evaluating the partition function (*e.g.* hyper-netted chain

theory) focus on the particles in the system and how to develop approximations for correlations between them. These approaches work well in capturing the short range correlations and fluctuations that occur in the system. Another perspective is to use a field theoretic approach. In this case, the focus is no longer on the particles in the system, but rather on collective modes, such as the density or an effective one-body interaction potential generated by the particles. Mathematically, this is done by representing the grand partition function as a functional integral over an interaction field through the use of the Hubbard-Stratonovich transformation [115, 116]. The Hubbard-Stratonovich transformation is used to convert a particle theory into its respective field theory by linearizing the density operator in the many-body interaction term of the Hamiltonian and introducing an auxiliary scalar field. The main goal of the Hubbard-Stratonovich transformation is to reformulate a system of particles interacting through two-body potentials into a system of independent particles interacting with a fluctuating field.

For an open system where the charged particles are at a chemical potential μ and at an absolute temperature T, we may define the grand partition function as

$$Z_G[\gamma, \Sigma] = \sum_{N=0}^{\infty} \frac{1}{N! \Lambda^{3N}} \int \prod_{t=1}^{N} d\mathbf{R}_t d\mathbf{\Omega}_t \tag{3.10}$$

$$\times \exp\left[-\beta E^{elec} - \beta E^{ref} + \sum_{k=1}^{N} \gamma(\mathbf{R}_k, \mathbf{\Omega}_k) \right]$$

where $\beta = 1/(k_B T)$, k_B is the Boltzmann constant, N is the number of particles, R_k is the position of the kth particle, $\mathbf{\Omega}_k$ is the orientation, Λ is the thermal wavelength of the particle and $\gamma(\mathbf{r}, \mathbf{\Omega}) = \beta[\mu - \upsilon(\mathbf{r}, \mathbf{\Omega})]$ where υ is an arbitrarily applied external field. When integrating over the orientation Ω we write

$$\int d\mathbf{\Omega} \rightarrow \int_0^{\pi} \frac{\sin\theta d\theta}{2} \int_0^{2\pi} \frac{d\phi}{2\pi} \int_0^{2\pi} \frac{d\psi}{2\pi}$$

where θ, ψ and ϕ are the Euler angles which specify the orientation of the particles. We may now write the energy of electrostatic interaction with in the system E^{elec} as

$$E^{elec} = \int d\mathbf{r} d\mathbf{r}' Q(\mathbf{r}) G_0(\mathbf{r}, \mathbf{r}') Q(\mathbf{r}) - \sum_k e^{se}(\mathbf{r}_k, \mathbf{\Omega}_k) \tag{3.11}$$

with $G_0(\mathbf{r}, \mathbf{r}')$ the Greens function of the Poisson equation. The self energy of the particle $e^{se}(\mathbf{r}_k, \mathbf{\Omega}_k)$ may be written as

$$e^{se}(\mathbf{r}_k, \mathbf{\Omega}_k) = \frac{1}{2} \int d\mathbf{r} d\mathbf{r}' Q(\mathbf{r} - \mathbf{R}, \mathbf{\Omega}) G_0(\mathbf{r}, \mathbf{r}') Q(\mathbf{r}' - \mathbf{R}, \mathbf{\Omega})$$

We now use the Hubbard-Stratonovich transformation to express the grand partition function as a functional integral. The key identity in the Hubbard-Stratonovich method is simply an observation of the result of a Gaussian integral. This employs the relation

$$\int_{-\infty}^{\infty} dx\, e^{ax^2 - 2bx} = \sqrt{\frac{\pi}{a}} e^{b^2/a}$$

to rewrite the partition function of Equation 3.10 as

$$Z_G[\gamma, \Sigma] = \frac{N_0}{N_{free}} \langle Z_G^{ref}[\gamma - qi\psi + \beta e^{se}] \rangle_0 \tag{3.12}$$

where the average $\langle (\cdots) \rangle_0$ denotes

$$\langle (\cdots) \rangle_0 = \frac{1}{N_0} \int D\psi(\cdot)(\cdots) \exp\left\{ -\frac{1}{2\beta} \int d\mathbf{r} d\mathbf{r}' \psi(\mathbf{r}) G_0^{-1}(\mathbf{r}, \mathbf{r}') \psi(\mathbf{r}') \right\}$$

and

$$N_0 = \int D\psi(\cdots) \exp\left[-\frac{1}{2\beta} \int d\mathbf{r}d\mathbf{r}'\psi(\mathbf{r})G_0^{-1}(\mathbf{r}, \mathbf{r}')\psi(\mathbf{r}')\right]$$

$$N_{\text{free}} = \int D\psi(\cdots) \exp\left[-\frac{1}{2\beta} \int d\mathbf{r}d\mathbf{r}'\psi(\mathbf{r})G_{\text{free}}^{-1}(\mathbf{r}, \mathbf{r}')\psi(\mathbf{r}')\right]$$

This theory is exact and converts a particle focussed theory into a field theory. The partition function of a system with electrostatic interactions is the same as the partition function without, but with the particles coupled to a randomly fluctuating Gaussian field with a covariance given by the Green's function of the Poisson equation.

3.5 Approximating the Partition Function

While the definition of the partition function written previously is formally exact, it is extremely difficult to obtain analytical forms for anything but the most simple systems. This is a result of the dependence of Z_G^{ref} on the field ψ. We now present separate methods for approximating the partition function; mean field theory, variational perturbation theory and cumulant Expansion. These methods have been tried variously in the literature to overcome the intractability of the partition function.

3.5.1 Mean Field Theory

Mean field theories (MFT) or saddle point approximations are the most simple methods to approximate the partition function. Mean-field theory is based on the assumption that the fluctuations around the average value of the order parameter are so small that they can be neglected. The interaction terms in the Hamiltonian are replaced by an effective, mean field term. In this way, all the information on correlations in the fluctuations is lost. Here, the integrand of the functional integral from the partition function is replaced by

the maximum value possible. The advantage of MFT is that it is relatively simple to use and can correctly predict the qualitative features of systems in most cases. Examples of MFT are the Weiss molecular field theory [117] which gives an expression for the order parameter but offers no illumination on the free energy or partition function and the Bragg-Williams approximation which is based on minimizing the free energy. The mean field approach is analogous to the Poisson-Boltzmann approximation for Coulombic systems. To apply the mean field theory here we replace the fluctuating value of the field $\psi(\mathbf{r})$ with an unchanging value $\bar{\psi}(\mathbf{r})$. The stationary value of the field is found by the approximating the integral by its largest value, therefore

$$\frac{\delta ln Z_G[\gamma, \Sigma]}{\delta \psi(\mathbf{r})} \approx 0$$

which gives

$$-\frac{1}{4\pi} \nabla \cdot [\epsilon(\mathbf{r}) \nabla \langle i\bar{\psi}(\mathbf{r}) \rangle_G / \beta] = \sum_\nu q_\nu \langle \rho^{ref}(\mathbf{r}, \gamma - iq\bar{\psi}) \rangle_G$$

which is the Poisson equation. Our averages here are given by

$$\langle (\cdots) \rangle_G = \frac{1}{Z_G} \frac{N_0}{N_{free}} \langle (\cdots) Z_G^{ref} [\gamma - qi\psi + \beta e^{se}] \rangle_0$$

The stationary value of the field is referred to as the classical field, here, we use the definition of the number density of a particle of type η

$$\rho_\eta = \frac{\delta \ln Z_G[\gamma, \sigma]}{\delta \gamma_\eta(\mathbf{r})}$$

Therefore we may interpret the function $i\psi(\mathbf{r})/\beta$ as being equal to an instantaneous value of the electrostatic potential and the functional integral can be thought of as an integral

over all possible shapes of the electrostatic potential due to the thermal motion of the electrolytes. This theory works well when the Bjerrum length is much smaller than the average distance between the particles i.e. $l_B/\alpha < 1$ and the electrostatic correlations between the particles can therefore be ignored. The mean field approximation implies that Poissons equation can self-consistently solve.

3.5.2 Cumulant Expansion

The cumulant expansion in statistical physics works by treating the energy of such a large ensemble as the sum of the energy of nearly independent regions. A cumulant expansion or strong coupling theory of the PB theory has been successfully demonstrated by expanding the fugacity of the counter-ions [62, 63]. This method assumes that there is not a strong repulsion between the ions at small separations. Therefore a power series is used to reorder Equation 3.12 to a form which may be evaluated using a path integral. Taking logarithms of Equation 3.12 allows us to rewrite the partition function of our system to be

$$\ln Z_G[\gamma] = \ln \frac{\mathcal{N}_0}{\mathcal{N}_{free}} + \ln \left[\langle e^{\ln Z_G^{ref}[\gamma - qi\psi + \beta e^{se}]} \rangle_0 \right]$$

The cumulant expansion is defined as the logarithm of a characteristic function, the characteristic function is the generator of the moments of the distribution. Therefore, generally we may write the cumulant expansion of a characteristic simple exponential e^x

$$\ln\langle e^x \rangle = \sum_{n=1}^{\infty} \frac{1}{n!} \langle x^n \rangle_c$$

$$= \langle e^x - 1 \rangle_c$$

70

where the c subscript denotes the cumulant expansion. For the strong coupling approach this is written as

$$\ln\langle e^x \rangle \simeq \langle x \rangle + \frac{1}{2}\left[\langle x^2 \rangle - \langle x \rangle^2\right] + \cdots$$

Truncating this to second order, the partition function becomes

$$\ln Z_G[\gamma] = \ln \frac{\mathcal{N}_0}{\mathcal{N}_{free}} + \langle \ln Z_G^{ref}[\gamma - qi\psi + \beta e^{se}]\rangle_0$$
$$+ \frac{1}{2}\left(\langle \ln Z_G \cdot \ln Z_G \rangle - \langle \ln Z_G \rangle\right)$$
$$+ \cdots$$

As this is a power series we have just displayed the first order expansion for brevity. The first order cumulant expansion has been applied successfully to first order by Moriera et al and Naji et al [63, 118] for systems consisting only of counter-ions. However, the expansion reduces to a low fugacity virial expansion when treating the ideal gas.

3.5.3 Variational Perturbation Theory

A successful method for approximating the partition function is to approximate the integrand with a Gaussian Hamiltonian and treating the differences as a perturbation. Therefore we extend the variational approximation to path integrals proposed by Feynmann and Kleinert to any desired order and accuracy [59, 119], which has been used in several works for different electrolyte systems [21, 60, 120, 121]. The general idea of the variational perturbation theory is that it will convert a divergent weak-coupling expansion into an exponentially fast convergent strong-coupling expansion.

71

To begin, we take averages with respect to the Gaussian Hamiltonian

$$H_{\mathcal{K}}[\psi] = -\frac{1}{2\beta} \int d\mathbf{r} d\mathbf{r}' \left[i\psi(\mathbf{r}) - i\bar{\psi}(\mathbf{r}) \right] G_{\mathcal{K}}^{-1}(\mathbf{r}, \mathbf{r}') \left[i\psi(\mathbf{r}') - i\bar{\psi}(\mathbf{r}') \right]$$

where the function $i\bar{\psi}(\mathbf{r})$ is the mean value of the system electric potential. We now introduce $\mathcal{K}$ which is a non local screening function caused by the presence of mobile charged particles which alter the propagation of the electrostatic potential. A Gaussian distribution is used to approximate the fluctuations in the electric potential. This distribution has a modified mean and a cumulant expansion can be used later to counteract any deviations from the Gaussian form. Therefore $G_{\mathcal{K}}$ measures the strength of the electric potential fluctuations and is defined as

$$G_{\mathcal{K}}^{-1}(\mathbf{r}, \mathbf{r}') = G_0^{-1}(\mathbf{r}, \mathbf{r}') + \mathcal{K}(\mathbf{r}, \mathbf{r}')$$

from here we may also write the work required to locate a point charge of magnitude q at a position $\mathbf{r}$ in the system as $\frac{q^2}{2} \left[G_{\mathcal{K}}(\mathbf{r}, \mathbf{r}) - G_{free}(\mathbf{r}, \mathbf{r}) \right]$.

First Order Approximation

Now the grand partition function may be written as

$$\ln Z_G = -\frac{1}{\beta} \int d\mathbf{r} d\mathbf{r}' \bar{\psi}(\mathbf{r}) G_0^{-1}(\mathbf{r}, \mathbf{r}') \delta\psi(\mathbf{r}') - \int d\mathbf{r} \Sigma(\mathbf{r}) i\delta\psi(\mathbf{r}) + \ln \frac{\mathcal{N}_{\mathcal{K}}}{\mathcal{N}_0} + \ln\langle e^{-\delta H} \rangle_{\mathcal{K}}$$

where

$$\bar{\rho}_\alpha(\mathbf{R}) = \Lambda_\alpha^{-d} exp \left[\gamma_\alpha(\mathbf{R}) - \int d\mathbf{r} Q_\alpha(\mathbf{r} - \mathbf{R}) i\bar{\psi}(\mathbf{r}) \right]$$

Employing the first order approximation yields

$$\ln Z_G[\gamma] \geq \frac{1}{2\beta} \int d\mathbf{r} d\mathbf{r}' i\bar{\psi}(\mathbf{r}) G_0^{-1}(\mathbf{r}, \mathbf{r}') i\bar{\psi}(\mathbf{r}')$$

$$- \frac{1}{2} \int_0^1 d\zeta Tr\mathcal{K}(G_{\zeta\mathcal{K}} - G_{\zeta\mathcal{K}}) - \int d\mathbf{r} i\Sigma(\mathbf{r})\phi(\mathbf{r})$$

$$\ln \frac{\mathcal{N}_0}{\mathcal{N}_{free}} + \langle \ln Z_G^{ref} \left[\gamma - qi\psi - qi\bar{\psi} + \beta e^{se} \right] \rangle_{\mathcal{K}} \quad (3.13)$$

with the averages $\langle \cdots \rangle_{\mathcal{K}}$ taken as

$$\langle (\cdots) \rangle_{\mathcal{K}} = \frac{1}{\mathcal{N}_{\mathcal{K}}} \int \mathcal{D}\psi(\cdot)(\cdots)e^{-H_{\mathcal{K}}[\psi]}$$

and

$$\mathcal{N}_{\mathcal{K}} = \int \mathcal{D}\psi(\cdot)e^{H_{\mathcal{K}}[\psi]}$$

Now, the value of the grand partition function must be greater than the approximate value of equation (3.13) due to the rigorous lower bound from the approximation above. The general idea of the variational method is that we are able to choose the value of the arbitrary functions $\bar{\psi}$ and $\mathcal{K}$ so that the grand partition function is independent of the mean electric potential. To do this we must satisfy the following conditions

$$\frac{\delta \ln Z_G[\gamma]}{\delta i\bar{\psi}_l(\mathbf{r})} = 0 \quad (3.14)$$

$$\frac{\delta \ln Z_G[\gamma]}{\delta \mathcal{K}(\mathbf{r}, \mathbf{r}')} = 0 \quad (3.15)$$

The first condition equation (3.14) links the charge density to the mean electric potential $i\bar{\psi}$ via a Poisson equation. For a system with an ideal gas reference system we may now

write the density of an ion of species α as

$$\rho_\alpha(\mathbf{r}) = \rho_\alpha^{bulk} exp\left[-q_n i\bar\psi(\mathbf{r}) - \frac{\beta Q(\mathbf{r})_\alpha^2}{2}\delta G_{\mathcal{K}}(\mathbf{r}, \mathbf{r})\right]$$

where $\rho_\alpha(\mathbf{r})$ is the density, ρ_α^{bulk} is the density of a bulk system and $Q(\mathbf{r})$ is the general charge distribution. This leads to a new form of (3.14) as

$$-\frac{1}{4\pi}\nabla i\bar\psi(\mathbf{r}) = \sum_\alpha Q(\mathbf{r})\rho_\alpha(\mathbf{r})$$

Equation (3.15) links the ion densities to the screening function via an integral equation.

$$\mathcal{K}(\mathbf{r}, \mathbf{r}') = \delta(\mathbf{r}, \mathbf{r}')\beta \sum_\alpha Q(\mathbf{r})_\alpha^2 \rho_\alpha(\mathbf{r}) \tag{3.16}$$

This then leaves an integral equation to solve for the screening function.

Second Order Approximation

Whilst the first order approximation has successes in approximating systems such as the classical one component plasma. This thesis will discuss some more complicated systems where it is discovered that approximating to first order does not find an equilibrium form for the splitting parameter as discussed in Chapters 4 and 5. This part will be unique to this thesis building upon the previously available literature.

$$-H = -\frac{1}{2\beta}\int d\mathbf{r}d\mathbf{r}'\psi(\mathbf{r})G_0^{-1}(\mathbf{r}, \mathbf{r}')\psi(\mathbf{r}') - \int d\mathbf{r}\Sigma(\mathbf{r})i\psi(\mathbf{r})$$
$$+ \sum_\alpha \int d\mathbf{R}\Lambda_\alpha^{-d}e^{\left[\gamma_\alpha(\mathbf{R}) - \int d\mathbf{r}d\mathbf{r}'Q(\mathbf{r}-\mathbf{R})G_0(\mathbf{r}, \mathbf{r}')\Sigma'(\mathbf{r}') - \int d\mathbf{r}Q_\alpha(\mathbf{r}-\mathbf{R})i\psi(\mathbf{r}) + \cdots\right]}$$

There is an ambiguity as to where the fixed charge appears in the Hamiltonian. This does not influence the predictions at the mean field level. It does not appear to have an effect

until the second loop order.

$$-H = -\frac{1}{2\beta} \int d\mathbf{r}d\mathbf{r}' \bar\psi(\mathbf{r}) G_0^{-1}(\mathbf{r},\mathbf{r}')\bar\psi(\mathbf{r}') - \int d\mathbf{r}\Sigma(\mathbf{r})i\bar\psi(\mathbf{r})$$
$$-\frac{1}{\beta} \int d\mathbf{r}d\mathbf{r}' \bar\psi(\mathbf{r}) G_0^{-1}(\mathbf{r},\mathbf{r}')\delta\psi(\mathbf{r}') - \int d\mathbf{r}\Sigma(\mathbf{r})i\delta\psi(\mathbf{r})$$
$$-\frac{1}{2\beta} \int d\mathbf{r}d\mathbf{r}' \delta\psi(\mathbf{r}) G_0^{-1}(\mathbf{r},\mathbf{r}')\delta\psi(\mathbf{r}')$$
$$+\sum_\alpha \int d\mathbf{R}\Lambda_\alpha^{-d} exp\left[\gamma_\alpha(\mathbf{R}) - \int d\mathbf{r}Q_\alpha(\mathbf{r}-\mathbf{R})[i\bar\psi(\mathbf{r}) + i\delta\psi(\mathbf{r})]\right]$$

Therefore we may write the perturbation of the system as

$$-\delta H = -\frac{1}{\beta} \int d\mathbf{r}d\mathbf{r}' \bar\psi(\mathbf{r}) G_0^{-1}(\mathbf{r},\mathbf{r}')\delta\psi(\mathbf{r}') - \int d\mathbf{r}\Sigma(\mathbf{r})i\delta\psi(\mathbf{r})$$
$$+\frac{1}{2\beta} \int d\mathbf{r}d\mathbf{r}' \delta\psi(\mathbf{r})\mathcal{K}(\mathbf{r},\mathbf{r}')$$
$$+\sum_\alpha \int d\mathbf{R}\Lambda_\alpha^{-d} exp\left[\gamma_\alpha(\mathbf{R}) - \int d\mathbf{r}Q_\alpha(\mathbf{r}-\mathbf{R})i\bar\psi(\mathbf{r})\right]$$

Now

$$\ln Z_G = -\frac{1}{\beta} \int d\mathbf{r}d\mathbf{r}' \bar\psi(\mathbf{r}) G_0^{-1}(\mathbf{r},\mathbf{r}')\delta\psi(\mathbf{r}') - \int d\mathbf{r}\Sigma(\mathbf{r})i\delta\psi(\mathbf{r}) + \ln\frac{\mathcal{N}_\mathcal{K}}{\mathcal{N}_0} + \ln\langle e^{-\delta H}\rangle_\mathcal{K}$$

where

$$\bar\rho_\alpha(\mathbf{R}) = \Lambda_\alpha^{-d} exp\left[\gamma_\alpha(\mathbf{R}) - \int d\mathbf{r}Q_\alpha(\mathbf{r}-\mathbf{R})i\bar\psi(\mathbf{r})\right]$$

Therefore

$$
\begin{aligned}
-\delta H = & -\frac{1}{\beta} \int d\mathbf{r}d\mathbf{r}' \bar{\psi}(\mathbf{r}) G_0^{-1}(\mathbf{r}, \mathbf{r}') \delta\psi(\mathbf{r}') - \int d\mathbf{r}\Sigma(\mathbf{r}) i\delta\psi(\mathbf{r}) \\
& + \frac{1}{2\beta} \int d\mathbf{r}d\mathbf{r}' \delta\psi(\mathbf{r}) \mathcal{K}(\mathbf{r}, \mathbf{r}') \\
& + \sum_\alpha \int d\mathbf{R} \bar{\rho}_\alpha(\mathbf{R}) exp\left[-\int d\mathbf{r}Q_\alpha(\mathbf{r} - \mathbf{R}) i\delta\psi(\mathbf{r}) \right] \\
& \rightarrow \int db f R_1 \cdots \mathbf{R_N} exp\left[\sum_k \int d\mathbf{r}Q(\mathbf{r} - \mathbf{R_k}) i\psi(\mathbf{r}) \right]
\end{aligned}
$$

Now, taking averages yields

$$
\begin{aligned}
\langle -\delta H \rangle_\mathcal{K} = & \frac{1}{2\beta} \int d\mathbf{r}d\mathbf{r}' \mathcal{K}(\mathbf{r}, \mathbf{r}') G_+ \sum_\mathcal{K}(\mathbf{r}, \mathbf{r}') \\
& + \sum_\alpha \int d\mathbf{R} \bar{\rho}_\alpha(\mathbf{R}) exp\left[\frac{\beta}{2} \int d\mathbf{r}d\mathbf{r}' Q_\alpha(\mathbf{r} - \mathbf{R}) G_0^{-1}(\mathbf{r}, \mathbf{r}') Q_\alpha(\mathbf{r}' - \mathbf{R}) \right]
\end{aligned}
$$

3.6   Splitting Theory

As discussed in Section 2.3.1, whilst the mean field field theory is most accurate for longer wavelengths as it is focused on a non fluctuating average field, the strong coupling or loop expansions consider the movement of the individual ions and are therefore much more accurate under short wavelengths. Therefore, a method to "split" the approximation to the partition function under both long and short wavelengths is discussed. Santangelo [68] and Weeks et al [122] pioneered the usage of a "splitting operator" $\mathcal{P}$ to filter out short wavelengths from the Green's function. Therefore we may write the Green's function G_0 as a combination between the short wavelength contribution G_s and long wavelength contribution G_l. i.e.

$$
G_0(\mathbf{r}, \mathbf{r}') = G_s(\mathbf{r}, \mathbf{r}') + G_l(\mathbf{r}, \mathbf{r}')
$$

where $G_s = (1 - \mathcal{P})G_0$ and $G_l = \mathcal{P}G_0$. We must now define a form for the splitting parameter $\mathcal{P}$, the exact form of which remains arbitrary. Going by the works of Santangelo, Weeks et al and Halto and Lue, $\mathcal{P}$ may be written as

$$\mathcal{P} = \begin{cases} [1 - \sigma^2\nabla^2]^{-1} & \text{Santangelo} \\ \exp[-\sigma^2\nabla^2]^{-1} & \text{Weeks and co-workers} \\ [1 - \sigma^2\nabla^2 + \sigma^4\nabla^4]^{-1} & \text{Hatlo and Lue} \end{cases}$$

where σ is used as a length scale to divide the long and short wavelengths. Halto and Lue used the final splitting format to enable the calculations to take the form of differential equations rather than integral equations. Whilst the form of the splitting parameter is arbitrary, it could be possible to create a spatially varying splitting parameter instead of using a generic one as above. This could lead to more accurate results further down the line, particularly when dealing with more complicated systems. We can now write the one particle interaction potential as

$$u_\eta(\mathbf{r}) = \int d\mathbf{r}' G_s(\mathbf{r}, \mathbf{r}')\Sigma(\mathbf{r}') + \frac{q_\eta^2}{2}\delta G_0(\mathbf{r}, \mathbf{r}) - \frac{q_\eta^2}{2}\mathcal{P}G_{\text{free}}(\mathbf{r}, \mathbf{r})$$

with $\delta G_0 = G_0 - G_{\text{free}}$. The short wavelength contribution to the self energy of the particles may be written as

$$E^{\text{se}} = \frac{1}{2}\int d\mathbf{r}d\mathbf{r}'\Sigma(\mathbf{r})G_s(\mathbf{r}, \mathbf{r}')\Sigma(\mathbf{r}')$$

which allows us to now write the electrostatic contribution to the Hamiltonian as

$$E^{elec} = \frac{\lambda_l}{2} \int d\mathbf{r} d\mathbf{r}' Q(\mathbf{r}) G_l(\mathbf{r}, \mathbf{r}') Q(\mathbf{r}') + E^{se}$$

$$+ \frac{\lambda_l}{2} \sum_{\eta j, \eta' k} G_s(\mathbf{r}_{\eta,j}, \mathbf{r}_{\eta',k})$$

$$+ \sum_{\eta j, \eta' k} \left[u_e ta(\mathbf{r}_{\eta,k} - \frac{q_\eta^2 \lambda_s}{2} G_s(\mathbf{r}_{\eta,k}, \mathbf{r}_{\eta,k}) - \frac{q_\eta^2 \lambda_l}{2} \mathcal{P} \delta G_0(\mathbf{r}_{\eta,k}, \mathbf{r}_{\eta,k}) \right]$$

. Therefore the Hamiltonian of the system may be written as

$$H[\psi_l, \psi_s] = \frac{1}{2\beta\lambda_l} \int d\mathbf{r} d\mathbf{r}' \psi_l(\mathbf{r}) G_l^{-1}(\mathbf{r}, \mathbf{r}') \psi_l(\mathbf{r}') + \frac{1}{2\beta\lambda_s} \int d\mathbf{r} d\mathbf{r}' \psi_s(\mathbf{r}) G_s^{-1}(\mathbf{r}, \mathbf{r}') \psi_s(\mathbf{r}')$$

$$+ \beta E^{se} - \ln Z_G^{\text{ref}} \left[\gamma - qi\psi_l - qi\psi_s - \beta u + \frac{\beta q^2 \lambda_s G_s}{2} + \frac{\beta q^2 \lambda_l \mathcal{P} \delta G_0}{2} + \beta e^{se} \right]$$

by twice performing a Hubbard-Stratanovich transformation on the grand partition function of the system

$$Z_G[\gamma, \Sigma] = \frac{1}{\mathcal{N}_l \mathcal{N}_s} \int \mathcal{D}\psi_l(\cdot) \mathcal{D}\psi_s(\cdot) e^{-H[\psi_l, \psi_s}$$

where

$$\mathcal{N}_k = \int \mathcal{D}\psi(\cdot) e^{-\frac{1}{2\beta} \int d\mathbf{r} \psi(\mathbf{r}) G_k^{-1}(\mathbf{r}, \mathbf{r}') \psi(\mathbf{r}')}$$

and uses two fields ψ_l and ψ_s which fluctuate at long and short wavelengths respectively within the long and short wavelength Greens functions (G_l and G_s). We now come to the stage of choosing two approximations to approximate the long and short wavelength contributions individually. It makes sense to use the methods displayed above which are successful under specific scenarios. In this work we will use a mean field approximation to model the long range behaviour. This is due to the mean field theory approach taking

an average over all particles in a field, meaning that when the system is weakly fluctuating under a long wavelength ($\mathbf{r} - \mathbf{r}' > \sigma$), the loop expansion or variational perturbation theory are well suited. Conversely, under a short wavelength ($\mathbf{r} - \mathbf{r}' < \sigma$) where there are strong correlations between the individual particles, an approach which considers individual particles is most prudent. Therefore, as mentioned above, a cumulant expansion is used to approximate the short wavelength.

We are now in a position to use a path integral on the short wavelength field ψ_s to gain a mean field theory for the long wavelength. Therefore, as the functional of the long wavelength nodes of ψ_l, we may express the effective Hamiltonian H_l as

$$H_l[\psi_l] = -\beta E^{\mathrm{se}} - \ln\left[\frac{1}{\mathcal{N}_s} \int \mathcal{D}\psi_s(\cdot) e^{-H[\psi_l, \psi_s]}\right]$$

. The form of the splitting parameter $\mathcal{P}$ in it's precise form is fairly arbitrary, and in this work we will choose

$$\mathcal{P} = [1 - \sigma^2 \nabla^2 + \sigma^4 \nabla^4]^{-1}. \tag{3.17}$$

With this in mind we are able to rewrite the total electrostatic contribution to the system as

$$
\begin{aligned}
E^{elec} = E^{se} &+ \frac{1}{2}\int d\mathbf{r} d\mathbf{r}' Q(\mathbf{r}) G_l(\mathbf{r}, \mathbf{r}') Q(\mathbf{r}) \\
&+ \int d\mathbf{r} d\mathbf{r}' q(\mathbf{r}) G_s(\mathbf{r}, \mathbf{r}') q(\mathbf{r}) \\
&+ \sum_k [u(\mathbf{R}_k, \mathbf{\Omega}_k) - e_s^{se}(\mathbf{R}_k, \mathbf{\Omega}_k)]
\end{aligned}
\tag{3.18}
$$

where u represents the one particle interaction potential due to short wavelength interactions and is written as

$$u(\mathbf{R}, \mathbf{\Omega}) = \int d\mathbf{r} d\mathbf{r}' Q(\mathbf{r} - \mathbf{R}) G_l(\mathbf{r}, \mathbf{r}') \Sigma(\mathbf{r}') \tag{3.19}$$

Also, E^{se} represents the short range self energy of the fixed charges and is given by

$$E^{se} = \frac{1}{2} \int d\mathbf{r} d\mathbf{r}' \Sigma(\mathbf{r}) G_l(\mathbf{r}, \mathbf{r}') \Sigma(\mathbf{r}') \tag{3.20}$$

We may now apply the Hubbard-Stratonovich transformation[115, 116] to the grand partition function. This allows us to represent the grand partition function as a functional integral over ψ_l and ψ_s which represent the long and short length scale fluctuations respectively. We now write this as

$$Z_G[\gamma, \Sigma] = \frac{e^{-\beta E^{se}}}{N_1} \int D\psi_l(\cdot)$$
$$\times \exp\left[-\frac{1}{2\beta} \int d\mathbf{r} d\mathbf{r}' \psi_l(\mathbf{r}) G_l(\mathbf{r}, \mathbf{r}') \psi(\mathbf{r}') \right.$$
$$\left. + \ln \bar{Z}_G^{ref}[\gamma - \beta u + \beta e_s^{se} - Qi\psi_l] \right] \tag{3.21}$$

where $\bar{Z}_G^{ref}$ is the partition function of the reference system, where there are no electrostatic interactions and is given as

$$\bar{Z}_G^{ref}[\gamma - \beta u + \beta e_s^{se} - Qi\psi_l] \equiv \langle \bar{Z}_{[}^{ref} \gamma - \beta u + \beta e_s^{se} - Qi\psi_l - -Qi\psi_s] \rangle_s \tag{3.22}$$

where we define the average to be

$$\langle (\cdots) \rangle_s \equiv \frac{1}{N_s} \int D\psi_s(\cdot)(\cdots)$$
$$\times \exp\left[-\frac{1}{2\beta} \int d\mathbf{r} d\mathbf{r}' \psi_s(\mathbf{r}) G_s^{-1}(\mathbf{r}, \mathbf{r}') \psi_s(\mathbf{r}') \right] \tag{3.23}$$

and the normalisation constants are

$$N_l = \int D\psi(\cdot) \exp\left[-\frac{1}{2\beta}\int d\mathbf{r}d\mathbf{r}'\psi_s(\mathbf{r})G_l^{-1}(\mathbf{r},\mathbf{r}')\psi_s(\mathbf{r}')\right] \tag{3.24}$$

$$N_s = \int D\psi(\cdot) \exp\left[-\frac{1}{2\beta}\int d\mathbf{r}d\mathbf{r}'\psi_s(\mathbf{r})G_s^{-1}(\mathbf{r},\mathbf{r}')\psi_s(\mathbf{r}')\right] \tag{3.25}$$

We must approximate our grand partition function to be able to get a useful expression. We apply the variational perturbation theory [123] on the long wavelength interactions and also a strong-coupling expansion to the short wavelength interactions. This is important in a physical sense as it can be observed that the charges are strongly correlated at shorter length scales while being weakly correlated over long length scales. Using a cumulant expansion we may write the functional integration over the short-wavelength mode as

$$\ln \bar{Z}_G^{ref}[\gamma] \approx \langle \ln Z_G^{ref}[\gamma - Qi\psi_s]\rangle_s$$
$$+\frac{1}{2}\langle \ln Z_G^{ref}[\gamma - Qi\psi_s] ln Z_G^{ref}[\gamma - Qi\psi_s]\rangle_s^{(c)} + \cdots , \tag{3.26}$$

where (c) denotes a cumulant average. This is analogous to an expansion in the fugacity of the particles. If we use the ideal gas reference system we may write this as

$$\ln \bar{Z}_G^{ref}[\gamma] \approx \Lambda^{-3}\int d\mathbf{R}d\mathbf{\Omega}e^{\gamma(\mathbf{R},\mathbf{\Omega})-\beta e_s^{se}(\mathbf{R},\mathbf{\Omega})} + \cdots , \tag{3.27}$$

Adapting the variational perturbation theory for the long wavelength interactions. Our Hamiltonian is given by

$$H_\mathcal{K}[\psi_l] = \frac{1}{2\beta}\int d\mathbf{r}d\mathbf{r}'[\psi_l(\mathbf{r}) - \bar{\psi}_l(\mathbf{r})]G_\mathcal{K}^{-1}(\mathbf{r},\mathbf{r}')[\psi_l(\mathbf{r}') - \bar{\psi}_l(\mathbf{r}')], \tag{3.28}$$

Here the fluctuations in the field are assumed to be Gaussian with a mean value of $\bar{\psi}_l$ and

a spatial correlation of $G_{\mathcal{K}}(\mathbf{r}, \mathbf{r}')$. $G_{\parallel}$ is the normalised Greens function given by

$$G_{\mathcal{K}}^{-1}(\mathbf{r}, \mathbf{r}') = G_l^{-1}(\mathbf{r}, \mathbf{r}') + \mathcal{K}(\mathbf{r}, \mathbf{r}') \qquad (3.29)$$

Physically $G_{\mathcal{K}}^{-1}(\mathbf{r}, \mathbf{r}')$ is the renormalised green's function which represents how the influence of a charge propagates through the system. $\mathcal{K}(\mathbf{r}, \mathbf{r}')$ is a screening function which describes how the presence of mobile charges modifies the behaviour of the system.

Truncating the variational perturbation expansion at first order we obtain

$$
\begin{aligned}
\ln Z_G[\gamma, \Sigma] \approx \langle \ln \bar{Z}_G^{ref}[\gamma - \beta u + \beta e_s^{se} - Qi\bar{\psi}_l - Qi\bar{\psi}_l - Qi\delta\psi_l] \rangle_{\mathcal{K}} \\
+ \frac{1}{2\beta} \int d\mathbf{r} d\mathbf{r}' i\bar{\psi}_l(\mathbf{r}) G_l^{-1}(\mathbf{r}, \mathbf{r}') i\bar{\psi}_l(\mathbf{r}') \\
- \int d\mathbf{r} \Sigma(\mathbf{r}) i\bar{\psi}_l(\mathbf{r}) - \frac{1}{2} \int_0^1 d\zeta Tr\mathcal{K}(G_{\zeta\mathcal{K}} - G_{\mathcal{K}}) \\
- \frac{\beta}{2} \int d\mathbf{r} d\mathbf{r}' \Sigma(\mathbf{r})(G_s(\mathbf{r}, \mathbf{r}')\Sigma(\mathbf{r}'), \qquad (3.30)
\end{aligned}
$$

where $G_{\zeta\mathcal{K}}^{-1} = G_l^{-1} + \zeta\mathcal{K}$ and

$$
\begin{aligned}
\langle (\cdots) \rangle_{\mathcal{K}} = \frac{1}{\mathcal{N}_{\mathcal{K}}} \int \mathcal{D}\delta\psi(\cdot)(\cdots) \\
\times \left[- \frac{1}{2\beta} \int d\mathbf{r}\mathbf{r}' \delta\psi(\mathbf{r}) G_{\mathcal{K}}^{-1}(\mathbf{r}, \mathbf{r}')\delta\psi(\mathbf{r}) \right] \qquad (3.31)
\end{aligned}
$$

with the normalisation constant $\mathcal{N}_{\mathcal{K}}$ given as

$$\mathcal{N}_{\mathcal{K}} = \int \mathcal{D}\delta\psi(\cdot)(\cdots) \exp\left[- \frac{1}{2\beta} \int d\mathbf{r} d\mathbf{r}' \delta\psi(\mathbf{r}) G_{\mathcal{K}}^{-1}(\mathbf{r}, \mathbf{r}')\delta\psi(\mathbf{r}) \right]. \qquad (3.32)$$

Now, to adapt this for the ideal gas reference system we may combine (3.27) and (3.30) to

give

$$\ln Z_G[\gamma, \Sigma] \approx \Lambda^{-3} \int d\mathbf{R} d\mathbf{\Omega} exp\left[\gamma(\mathbf{R}, \mathbf{\Omega}) - \beta u(\mathbf{R}, \mathbf{\Omega})\right]$$
$$- \beta e_{\mathcal{K}}^{se}(\mathbf{R}, \mathbf{\Omega}) - \int d\mathbf{r} Q(\mathbf{r} - \mathbf{R}, \mathbf{\Omega}) i\bar{\psi}_l(\mathbf{r}')$$
$$+ \frac{1}{2\beta} \int d\mathbf{r} d\mathbf{r}' i\bar{\psi}_l(\mathbf{r}) G_l^{-1}(\mathbf{r}, \mathbf{r}') i\bar{\psi}_l(\mathbf{r}')$$
$$- \int d\mathbf{r} \Sigma(\mathbf{r}) i\bar{\psi}_l(\mathbf{r}) - \frac{1}{2} \int_0^1 d\zeta Tr\mathcal{K}(G_{\zeta\mathcal{K}} - G_{\mathcal{K}})$$
$$- \frac{\beta}{2} \int d\mathbf{r} d\mathbf{r}' \Sigma(\mathbf{r}) G_s(\mathbf{r}, \mathbf{r}') \Sigma(\mathbf{r}') \qquad (3.33)$$

where

$$e_{\mathcal{K}}^{se}(\mathbf{R}, \mathbf{\Omega}) = \frac{1}{2} \int d\mathbf{r} d\mathbf{r}' Q(\mathbf{R} - \mathbf{r}, \mathbf{\Omega}) G_0(\mathbf{r}, \mathbf{r}') Q(\mathbf{R} - \mathbf{r}', \mathbf{\Omega})$$

We may choose the quantities of $\bar{\psi}_l$ and $\mathcal{K}$ which best suit as in the exact system the physical properties do not depend on these variables. We must, however, choose the correct forms to assist the approximate theory. We choose the $\bar{\psi}_l$ and $\mathcal{K}$ to make the grand partition function stationary with respect to small variations in the functions

$$\frac{\delta \ln Z_G[\gamma, \Sigma]}{\delta i\bar{\psi}_l(\mathbf{r})} = 0 \qquad (3.34)$$

$$\frac{\delta \ln Z_G[\gamma, \Sigma]}{\delta \mathcal{K}(\mathbf{r}, \mathbf{r}')} = 0 \qquad (3.35)$$

The first equation leads to a Poisson equation

$$-\frac{1}{4\pi} \nabla^2 \phi(\mathbf{r}) = \int d\mathbf{R} d\mathbf{\Omega} Q(\mathbf{r} - \mathbf{R}, \mathbf{\Omega}) \rho(\mathbf{R}, \mathbf{\Omega}) + \Sigma(\mathbf{r}) \qquad (3.36)$$

where $\rho(\mathbf{R}, \boldsymbol{\Omega})$ is the density distribution of the particles and is described by the equation

$$\rho(\mathbf{R}, \boldsymbol{\Omega}) = \Lambda^{-3} \exp\left[\gamma(\mathbf{R}, \boldsymbol{\Omega}) - \beta u(\mathbf{R}, \boldsymbol{\Omega}) - \beta e_\mathcal{K}^{se}(\mathbf{R}, \boldsymbol{\Omega}) \right.$$
$$\left. - \int d\mathbf{r} Q(\mathbf{r} - \mathbf{R}, \boldsymbol{\Omega}) i \bar\psi_l(\mathbf{r}) \right] \tag{3.37}$$

where $\phi = \beta^{-1}\mathcal{P}^{-1} i\bar\psi_l$ is the electric potential with $i\bar\phi_l$. Therefore we may see that the slowly varying portion of the electric potential can be described by $\bar\phi_l$. Now, (3.34) allows us to describe $\mathcal{K}$, the screening function. We now allow the particles to interact through electrostatic forces only and truncate the cumulant expansion for the short-wavelength field and the variational perturbation expansion for the long wavelength field at first order to yield

$$\mathcal{K}(\mathbf{r}, \mathbf{r}) = \beta \int d\mathbf{R} d\boldsymbol{\Omega} Q(\mathbf{r} - \mathbf{R}, \boldsymbol{\Omega}) \rho(\mathbf{R}, \boldsymbol{\Omega}) Q(r' - R, \boldsymbol{\Omega}) \tag{3.38}$$

We can now calculate the Helmholtz free energy F of the system by performing a Legendre transform the grand partition function (3.33) to give

$$\beta F[\rho, \Sigma] \approx \int d\mathbf{R} d\boldsymbol{\Omega} \, \rho(\mathbf{R}, \boldsymbol{\Omega}) \left[\ln \rho(\mathbf{R}, \hat{\mathbf{n}}) \Lambda^d - 1 \right] + \frac{1}{2} \int_0^1 d\zeta \mathrm{Tr} \mathcal{K}(G_{\zeta\mathcal{K}} - G_l)$$
$$+ \frac{1}{2\beta} \int d\mathbf{r} d\mathbf{r}' i\bar\psi_l(\mathbf{r}) G_l^{-1}(\mathbf{r}, \mathbf{r}') i\bar\psi_l(\mathbf{r}')$$
$$+ \beta \int d\mathbf{r} d\mathbf{r}' Q(\mathbf{r} - \mathbf{R}, \boldsymbol{\Omega}) G_s(\mathbf{r}, \mathbf{r}') \Sigma(\mathbf{r}') + \frac{\beta}{2} \int d\mathbf{r} d\mathbf{r}' \Sigma(\mathbf{r}) G_s(\mathbf{r}, \mathbf{r}') \Sigma(\mathbf{r}')$$
$$\tag{3.39}$$

The first term in this equation is the ideal gas contribution to the free energy. The second is the long wavelength fluctuation contribution to the electrostatic interaction energy. The third term combines the short wavelength contribution with the self energy of the background charge and the short range interaction energy between the free charges in the system and the background charge.

Having determined the free energy, we are able to examine the influence of the properties which make up this energy. That is where the work will begin to take it's real shape as we will be able to model the effects of properties such as the density, charge etc and see how they affect the system.

3.7   Translationally Invariant Systems

Previous sections have built upon the existing literature to develop the theoretical framework which will be employed in this thesis. Taking the existing work into Fourier space and developing an analytical framework will be a unique part to this thesis. We will now simplify the final expressions for translationally invariant systems which will be used throughout this work to determine the thermodynamic properties of our system. In this work we define the Fourier transform as

$$\hat{f}(p) = \int dr e^{ipr} f(r)$$

with the inverse as

$$f(p) = -\int dp e^{-ipr} \hat{f}(r)$$

The Coulombic potential between two smeared charges $Q(\mathbf{r}')$ and $Q(\mathbf{r}')$ is defined as

$$\beta U = l_B \int d\mathbf{r} d\mathbf{r}' \frac{Q(\mathbf{r})Q(\mathbf{r}')}{|\mathbf{r}' - \mathbf{r}|}$$

which leads to a double convolution. We may then rewrite the general charge distribution of the system as

$$Q(p) = \int d\mathbf{r} e^{-i\mathbf{r}\cdot\mathbf{p}} Q(\mathbf{r})$$

leading to a Coulombic potential of

$$\beta U = \frac{4\pi l_B Q^2(p)}{p^2}$$

3.7.1 Debye Hückel Theory

Within this work we will refer to the first order variational perturbation theory of section 3.5.3 as the Debye-Hückel theory as the two are analogous when applied to point charge systems. We begin with the symmetric Debye Hückel theory, which considers a fluid composed of equal numbers of oppositely charged smeared charges with a charge distribution of $Q(p)$ in reciprocal space where p represents the distance from ion to ion (r). This represents the first order variational approximation discussed in Section 3.5.3. We may now rewrite equation 3.16 as $\mathcal{K}(p)$ which quantifies how the presence of mobile charges affects the behaviour of the system as

$$\mathcal{K}(p) = \beta \sum_\alpha \rho |Q(p)|^2$$

while the Greens functions are defined as

$$G_\mathcal{K}(P) = \frac{G_0(p)}{1 + \mathcal{K}(p)G_0(p)} \qquad \text{where} \qquad G_0(p) = \frac{4\pi}{\epsilon p^2}$$

The screening function of the system $\kappa^2(p)$ is defined as

$$\kappa^2(p) = \frac{4\pi}{\epsilon}\mathcal{K}(p)$$

We now employ the variational perturbation theory to obtain an upper variational bound to the Helmholtz free energy of the system

$$\frac{1}{V}F(\rho) \leq \sum_{k=\pm}\rho_k[\ln\rho_k\Lambda_k^{-d} - 1] + \frac{1}{2}\int_{\mathbf{p}}\left\{\ln\left[1 + \frac{\kappa^2(\mathbf{p})}{p^2}\right] - \frac{\kappa^2(\mathbf{p})}{p^2}\right\} \tag{3.40}$$

where $\int_{\mathbf{p}} \rightarrow \int \frac{p^2}{2\pi^2}dp$. From here we may find the pressure, βp, the interaction energy $\beta U/V$ and the species chemical potential, $\beta\mu$, of the system

$$\beta p = \rho\frac{\partial f(\rho)}{\partial\rho} - f(\rho)$$

$$\approx \sum_k \rho_k - \frac{1}{2}\int_{\mathbf{p}}\left\{\ln\left[1 + \frac{\kappa^2(\mathbf{p})}{p^2}\right] - \frac{\kappa^2(\mathbf{p})}{p^2 + \kappa^2(\mathbf{p})}\right\} \tag{3.41}$$

$$\frac{\beta U}{V} \approx -\frac{1}{2}\int_{\mathbf{p}}\mathcal{K}(\mathbf{p})G_l(\mathbf{p})\mathcal{K}(\mathbf{p})G_{\mathcal{K}}(\mathbf{p})$$

$$\beta\mu = \frac{\partial f(\rho,\beta)}{\partial\rho_k}$$

$$\approx \ln\rho_k\Lambda_k^d + \beta\Delta e_{\mathcal{K},k} \tag{3.42}$$

where

$$\beta\Delta e_{\mathcal{K},\alpha} = \frac{-\beta}{2}\int_{\mathbf{p}}|Q_\alpha(p)|^2 G_0(p)\mathcal{K}(p)G_{\mathcal{K}}(p)$$

$$= \frac{-\beta}{\pi\epsilon}\int_0^\infty dp\,\frac{|Q_\alpha(p)|^2\kappa^2(p)}{p^2 + \kappa^2(p)}$$

3.7.2 Splitting Theory

To deploy the Debye Hückel Hole or *Splitting* theory the screening function $\kappa^2(p)$ is coupled with the splitting parameter $\mathcal{P}(\mathbf{p})$. The form of $\mathcal{P}(\mathbf{p})$ is relatively arbitrary so for this work we will take the form of the splitting parameter to be

$$\mathcal{P}(\mathbf{p}) = (1 + \sigma^2 p^2 + \sigma^4 p^4)^{-1}$$

Therefore, using this we may rewrite the thermodynamic properties defined above as

Helmholtz free energy

$$\frac{1}{V} F(\rho) \leq \sum_{k=\pm} \rho_k [\ln \rho_k \Lambda_k^{-d} - 1] + \frac{1}{2} \int_{\mathbf{p}} \left\{ \ln \left[1 + \frac{\mathcal{P}(\mathbf{p})\kappa^2(\mathbf{p})}{p^2} \right] - \frac{\mathcal{P}(\mathbf{p})\kappa^2(\mathbf{p})}{p^2} \right\} \quad (3.43)$$

System Pressure

$$\beta p \approx \sum_k \rho_k - \frac{1}{2} \int_{\mathbf{p}} \left\{ \ln \left[1 + \frac{\mathcal{P}(\mathbf{p})\kappa^2(\mathbf{p})}{p^2} \right] - \frac{\mathcal{P}(\mathbf{p})\kappa^2(\mathbf{p})}{p^2 + \mathcal{P}(\mathbf{p})\kappa^2(\mathbf{p})} \right\} \quad (3.44)$$

Chemical Potential

$$\beta \mu \approx \ln \rho_k \Lambda_k^d + \beta \Delta e_{\mathcal{K},k} \quad (3.45)$$

3.7.3 Numerical Methods

This thesis uses the software PYTHON to evaluate the accuracy of the analytically defined formulae. The general forms of the formulae described above were tested against the analytically derived forms shown in Chapters 4 and 5. The packages Numpy and Scipy were used for each calculation and each was found to match the analytical counterpart to 16dp. Where PYTHON scripts were not able to converge quickly enough, the software

C++ was used in it's place to numerically measure against the analytical results.

3.8 Integral Equation Methods

The two main integral methods which will be used to qualify the theoretical and simulation data which will be developed in this thesis are the Hyper-netted chain theory (HNC) and the Mean Spherical Approximation (MSA).

3.8.1 MSA and RPA

We now turn our attention to the MSA and RPA methods which have been solved for the URPM by Warren et al [12] and Coslovich et al [10]. The reason we present them together is that the methods are identical for the ultrasoft system of soft spheres. Both methods provide a closure for solving the OZ relations.

This gives a less numerically demanding result than the HNC in

$$c_{\alpha\beta}(\mathbf{r}) = -\beta U_{\alpha\beta}(\mathbf{r}).$$

This can be solved for all l_B/α but can yield non-physical results such as negative pressures or $h_{\alpha\beta}(\mathbf{r}) < 1$. The symmetric properties of the URPM mean that the correlation functions of the RPA ate given by $h_{\pm\pm}(\mathbf{r}) = \pm h(\mathbf{r})$. Inserting this into the OZ equation with the RPA closure gives

$$\hat{h}(p) = \frac{-4\pi l_B exp(-\alpha^2 p^2)}{k^2 + k_0^2 exp(-\alpha^2 p^2)}$$

where $k_0 = 4\pi l_B \rho$ is the square root of the Debye wavevector. Writing $q = \alpha p$ and

$q_D = \alpha k_0$ we may determine the poles of $\hat{h}(q)$ through the solutions of

$$q^2 exp(q^2) = -q_D^2 \equiv -4\pi l_B \rho \alpha^2$$

Where the function $h(\mathbf{r})$ has asymptotic behaviour, the solutions are given through the Lambert W function, which solves $dW e^w = z$ [52]. Therefore $q^2 = W_0(-q_D^2)$ where W_0 is the principle Lambert W function. The corresponding decay length is therefore given by

$$\lambda_{RPA} = \alpha \times |W_0(-4\pi l_B \rho \alpha^2|^{-1/2}$$

It is noted that the RPA is very successful at determining the total correlation functions at higher densities however is not able to account for strong ion pairing at any density. The RPA also gives an non-physical prediction of $g_{\alpha\alpha}(r) < 0$ at low densities and temperatures.

Hyper-netted Chain Theory

The Hyper-netted chain equation is simply a closure relation to the total correlation of the system. The HNC approximation for the URPM was developed by Coslovich et al [10]. We will go through the steps of their calculations here in order to be able to benchmark the DH and Splitting approximations. We determine the pair correlation functions $g_{\alpha\beta}$, through which most thermodynamic properties are obtained through the total correlation functions [114]

$$h_{\alpha\beta}(\mathbf{r}) \equiv g_{\alpha\beta} - 1 \sim \frac{e^{-\mathbf{r}/\lambda}}{\mathbf{r}}$$

90

where λ is the screening length. The starting point of the HNC is the multi-component Ornstein-Zernike (OZ) relation which defines the direct correlation functions $c_{\alpha\beta}(r)$. Taking this in reciprocal space this relation is

$$\hat{h}_{\alpha\beta} = \hat{c}_{\alpha\beta} + \sum_{\gamma} \rho_{\gamma} \hat{c}_{\alpha\gamma} \hat{h}_{\gamma\beta}.$$

The HNC closure is defined in real space, and is

$$h_{\alpha\beta} = \exp(-\beta U_{\alpha\beta} + h_{\alpha\beta} - c_{\alpha\beta}) - 1$$

$$= \exp(h_{\alpha\beta} - \Delta c_{\alpha\beta}) - 1. \tag{3.46}$$

where $U_{\alpha\beta}$ is the pair potential between particles of species α and β. Therefore we can write $\Delta c_{\alpha\beta}) = -\beta U_{\alpha\beta} - c_{\alpha\beta}$ which represents the short-range parts of the direct correlation function. This solution can be numerically demanding and does not yield results for $l_B/\alpha \geq 10$. As this is the symmetric URPM the relations $h_{++} = h_{--}$ and $h_{++} = h_{--}$ are true, reducing the 3 coupled OZ relations into the following decoupled relation in p space.

$$\hat{h}_{\eta\eta}(p) = \frac{\hat{c}_{\eta\eta}(p)}{1 - \frac{1}{2}\hat{c}_{\eta\eta}(p)} \tag{3.47}$$

where η represents the total number and charge densities. Coslovich et al solve Equations 3.46 and 3.47 through an iterative Picard method for the thermodynamic properties of the URPM but take care to note that it is only applicable for $l_B/\alpha \leq 10$.

3.9 Conclusions

This chapter has presented different methods which can be used to approximate the electrostatic interactions in a system of mobile particles with an extended charge distribution. Firstly a general introduction to electrostatics was presented, to give a context to the statistical physics approaches which follow. We then defined the grand partition function of the grand canonical ensemble, this is used to derive the thermodynamic properties of the system through manipulation of the Helmholtz free energy. The Hubbard-Stratonovich transformation is used to display the functional integral.

However, the partition function is not easily approximated under the weak and strong coupling limits. This led to a discussion of four common methods for approximating the partition function, each with particular strengths and weaknesses. The first approach discussed, mean field theory, is used when the electrostatic correlations between the ions can be neglected, and therefore has strength in the weak coupling limit. Then a cumulant expansion is discussed which treats the large ensemble energy as a power series of the partition function. This method works well when there are not strong repulsions between the ions at small distances. We discuss using a variational perturbation theory which is designed to be used in the weak-coupling limit to convert this into a fast converging strong-coupling expansion. We evaluated this at first and second order. The splitting approximation, which combines different long and short wavelength approaches to account for a 'correlation hole' which appears around each ion, was then introduced. This employs but is not limited to the variational perturbation theory and cumulant expansion for the weak and strong coupling regions respectively. This splitting theory was then employed to develop a form of the Helmholtz free energy which is able to be interpreted for various systems. This free energy was then used to describe the URPM for translationally invariant systems. From here we were able to derive thermodynamic properties such

as the (electro)chemical potential and pressure which make up the theoretical framework for most of this thesis were defined. This section was split into two separate approaches, the Splitting theory defined above and the Debye Hückel Theory which is identical to the Splitting theory when the splitting parameter σ is zero. Finally we outlined the integral equations approaches which have been used in the literature to approximate the URPM. These were the Hyper-netted chain theory, Mean Spherical Approximation and the Random Phase Approximation. The latter two being identical due to the ultrasoft nature of the URPM. These will be used throughout as a benchmark for the Splitting and Debye-Hückel theory. This theory will be used throughout the remainder of this work, beginning with the symmetric URPM.

Chapter 4

Symmetric Electrolytes

4.1 Overview

This chapter contains a study of symmetric ultrasoft electrolytes, as defined in Chapters 2 and 3. The analysis will be broken down into two main versions of the URPM. Firstly, an analytical approach to modelling electrolytes with a Bessel smeared charge distribution will be completed with a detailed comparison between the Debye Hückel theory and the splitting theory. Secondly, electrolytes with a Gaussian smeared charge distribution will be studied and discussed using molecular dynamics simulations. As with the Bessel smeared charge section, a comparison of the Debye Hückel theory with the Splitting theory will be completed. During the analysis of the Gaussian smeared charge model, interesting results will lead to the conclusion that in order to fully understand the properties and behaviours of smeared charges, a less simplistic model must be studied.

4.2 General Formalism

To begin studying the URPM in earnest we must first consider the mathematical construct of the key thermodynamic properties which will be used in subsequent sections. These include the final forms of the screening function , κ^2, the Helmholtz free energy , $\beta F(\rho)/V$, the system pressure, βP, and the chemical potential, $\beta \mu_\pm$. Developing analytical forms of these key properties will help develop the understanding of the URPM. We begin by studying the Debye Hückel forms of the thermodynamic properties before investigating how the URPM responds to the introduction of the Debye Hückel Hole or *splitting* theory which will be a unique aspect to this particular work. This will expand upon the general theory of Chapter 3 but will introduce a specific function , $Q_\pm(r)$, which determines the charge density of the charge cloud of the URPM. We will determine the analytical forms of the key thermodynamic properties with a general charge density before introducing the Gaussian and Bessel smeared charge densities in subsequent sections.

Table 4.1: Critical points for the RPM, BSCM and GSCM are shown with references of where they were produced.

System	Method	l_B/α	$\rho\alpha^3$	Reference
RPM	DH	16.11	0.005	[2]
	DHBj	16.11	0.045	[2]
	Simulation	19.92	0.080	[52, 124]
URPM (GSCM)	RPA	26.07	0.001	[11]
	RPABj	26.07	0.0042	[93]
	Simulation	98.47	0.020	[7, 10]
URPM (BSCM)	RPA	20.85	0.0038	[11]

Table 4.1 shows the critical points for the RPM BSCM and GSCM. It is seen that the DH and RPA approximation for the RPM and URPM models respectively predict critical points at low temperatures and densities. However, including Bjerrum pairing as per Figures 2.4 and 2.5 from Fisher and Levin [2] shows similar critical temperatures but

a considerably increased critical density.

4.2.1 Choice of Charge Distribution

The choice of charge distribution is an important part of this thesis. This thesis uses a distribution of either the Bessel or Gaussian form to represent how the distribution of a charge propagates throughout the system. One expects that changing this distribution will have an arbitrary effect on the results shown throughout this thesis. This means that while the results will have a quantitative difference with different distributions, the qualitative behaviour of the system will be the same under different distributions.
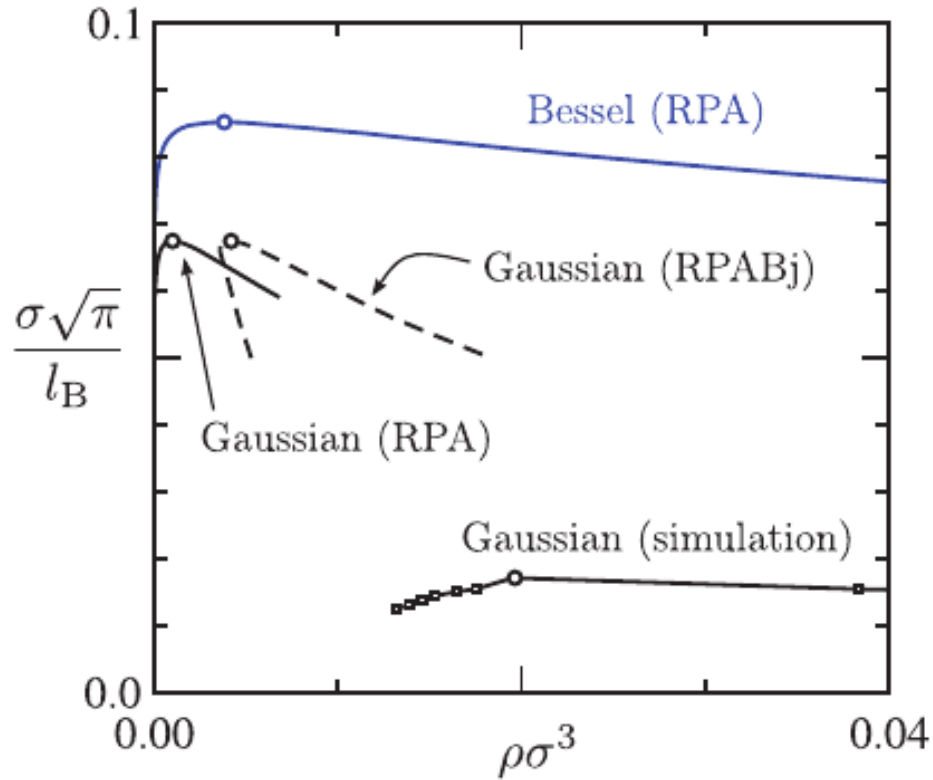
Figure 4.1: Vapour-liquid coexistence curves for the URPM where the critical points from Table. Taken from [11] where the notation used for the size of the ions is σ. Therefore $\sigma_{Warren} = \alpha$

We see the vapour liquid coexistence curves for the URPM in Figure 4.1. Here the RPA result for the BSCM has a similar critical density as the Bjerrum paired GSCM RPABj but at a higher temperature. As described above, the variance between the Gaussian and Bessel models is quantitative but there is no discernible difference in the behaviour of the two charge distributions. Now, with the addition of a specific charge cloud we are able to rewrite the general forms from Section 3.7 into analytical formulae to help our understanding of the Symmetric URPM. We will begin with a Bessel smeared charge approach and conclude with a Gaussian smeared charge in the style of Coslovich et al and Warren et al [7, 10–12].

4.3   Bessel Smeared Charge Electrolyte

We now consider an electrolyte consisting of identical cations and anions which have a Bessel charge distribution (as shown in Figure 4.2) $Q_\pm(r)$ which we define as

$$Q_\pm(\mathbf{r}) = q(2\pi^2\alpha^2 r)^{-1}K_1(r/\alpha) \qquad \longleftrightarrow \qquad \hat{Q}_\pm(\mathbf{p}) = q_k(1 + p^2\alpha^2)^{-1/2}$$

where α describes the size of the cations, K_1 is a modified Bessel unction of the second kind and anions of species k. Therefore the screening function $\kappa^2(p)$ becomes

$$\kappa^2(p) = \frac{\kappa_0^2}{(1 + p^2\alpha^2)}$$

where $\kappa_0^2 = 8\pi\rho l_B$ is the screening function for point charges. Firstly, the system will be discussed with reference to the standard Debye-Hückel Theory before modifying to include the splitting theory. This will allow us to contrast the effect of including the correlation 'hole' in the calculations. In this section, analytical forms of the thermodynamic properties electrolyte solutions consisting of symmetric cations and anions which exhibit

97
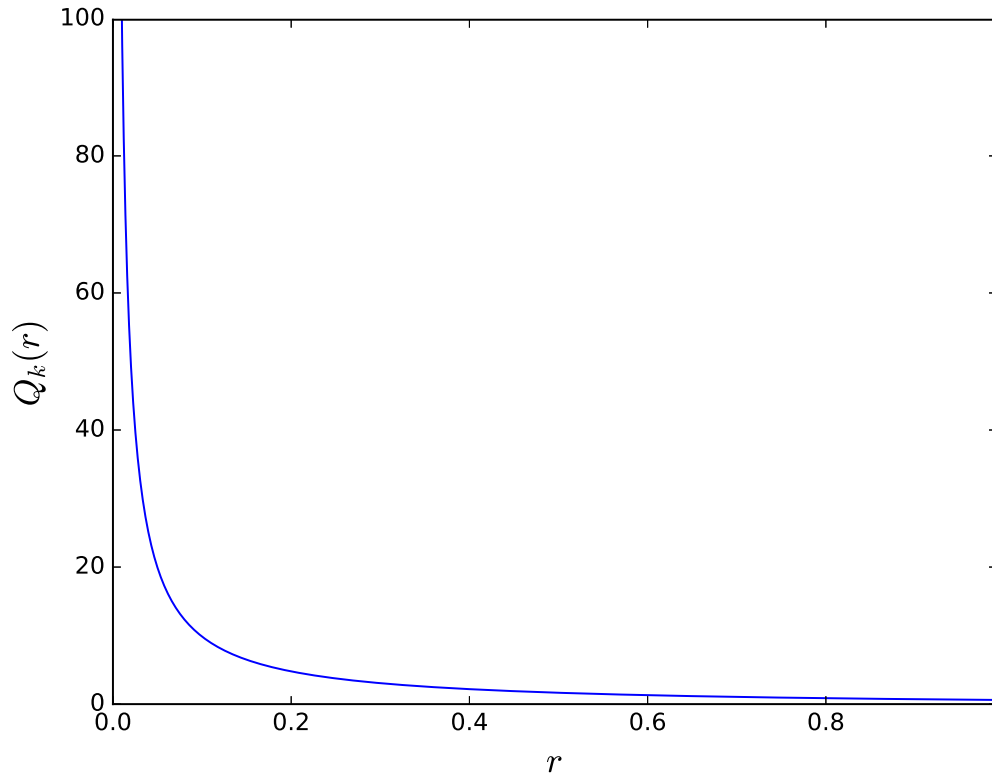
Figure 4.2: Bessel smeared charge distribution

a charge distribution of the form of a Bessel function. Firstly, the mathematical approach expanding from Section 4.2 is developed, showing how the screening function is affected by changing the charge distribution. Then we develop analytical forms for the Helmholtz free energy, internal energy, system pressure and species chemical potential which will become the building blocks for the analysis in Section 4.3.3. Firstly the system will be discussed in reference to the Debye-Hückel theory in Section 4.3.1 and is then adapted to account for the 'correlation hole' in Section 4.3.2. Using the theory developed in Section 4.2, we will examine several different systems of ions immersed in a continuum solvent. These systems will contain Bessel smeared or 'puffy' charges as shown in Figure 4.2. We will obtain analytical forms for the Helmholtz free energy, the pressure and the species chemical potentials of these systems and use numerical techniques to describe these re-

98

sults and to pursue more complicated results where analytical forms cannot be found.

4.3.1   Debye-Hückel (First Order Variational Perturbation Theory)

We may determine analytical expressions for the pressure βP and the species chemical potentials $\beta\mu_\pm$. We may rewrite the overall Debye-Hückel Helmholtz free energy defined in Equation 3.40 as

$$\beta f(\rho, \beta) \approx 2\rho \left[\ln \rho \Lambda^d - 1 - \frac{\kappa_0^2 l_B \alpha}{2} \sum_{k=0}^{2} \frac{M_k}{m_k} \right] + \frac{1}{2} \left[\frac{\alpha^{-3}}{6\pi} \sum_{k=0}^{1} (d_k^3 - g_k^3) - \frac{\kappa_0^2 \alpha^{-1}}{4\pi} \sum_{k=0}^{1} -G_k g_k \right]$$

where $-d_k^2$, $-g_k^2$ and $-m_k^2$ are the roots of the polynomials

$$x^2 + x,$$

$$x^2 + x + \kappa_0^2 \alpha^2,$$

$$(1 + x)(x(1 + x) + \kappa_0^2 \alpha^2)$$

respectively, and

$$G_k = \prod_{j \neq k}^{n} \frac{1}{g_j^2 - g_k^2}, \quad M_k = \prod_{j \neq k}^{n} \frac{1}{m_j^2 - m_k^2} \quad , g_j^2 \neq g_k^2, \quad m_j^2 \neq m_k^2$$

where $\sum_{k=0}^{n} G_k = \sum_{k=0}^{n} M_k = 0$ and $\sum_{0}^{n} d_k^2 = \sum_{0}^{n} g_k^2 = \sum_{0}^{n} m_k^2$.

We may now rewrite the pressure defined in Equation 3.41 as

$$\beta P = 2\rho - \frac{1}{2} \left[\frac{\alpha^{-3}}{6\pi} \sum_{k=0}^{1} (d_k^3 - g_k^3) - \frac{\kappa_0^2 \alpha^{-1}}{4\pi} \sum_{k=0}^{1} -G_k g_k \right] \tag{4.1}$$

and finally the system chemical potential defined in Equation 3.42 can be rewritten as

$$\beta\mu_\pm \approx 2\ln\rho\Lambda^d - \kappa_0^2 l_B \alpha \sum_{k=0}^{2} \frac{C_k}{c_k}$$

4.3.2 Splitting Theory

We now simplify the splitting theory for symmetric Bessel smeared charges. It is expected that this will give a more accurate depiction of the thermodynamic quantities of this system of identical 'puffy' charges. The overall Helmholtz free energy defined in Equation 3.43 is now written as

$$\beta f(\rho, \beta) = 2\rho \left[\ln\rho\Lambda^d - 1 - \frac{\kappa_0^2 l_B \alpha^5}{2\sigma^4} \sum_{k=0}^{4} \frac{C_k}{c_k} \right]$$
$$+ \frac{1}{2} \left[\frac{\alpha^{-3}}{6\pi} \sum_{k=0}^{3} (d_k^3 - b_k^3) - \frac{\kappa_0^2 \alpha^3}{4\pi\sigma^4} \sum_{k=0}^{3} -B_k B_k \right] \tag{4.2}$$

where $-d_k^2$, $-b_k^2$ and $-c_k^2$ are the roots of the polynomials

$$x\left(x^3 + x^2\left(\frac{\sigma^2\alpha^2 + \sigma^4}{\sigma^4}\right) + x\left(\frac{\alpha^4 + \sigma^2\alpha^2}{\sigma^4}\right) + \left(\frac{\alpha^4}{\sigma^4}\right)\right)$$
$$x^4 + x^3\left(\frac{\sigma^2\alpha^2 + \sigma^4}{\sigma^4}\right) + x^2\left(\frac{\alpha^4 + \sigma^2\alpha^2}{\sigma^4}\right) + x\left(\frac{\alpha^4}{\sigma^4}\right) + \frac{\kappa_0^2\alpha^6}{\sigma^4}$$
$$(1+x)\left(x^4 + x^3\left(\frac{\sigma^2\alpha^2 + \sigma^4}{\sigma^4}\right) + x^2\left(\frac{\alpha^4 + \sigma^2\alpha^2}{\sigma^4}\right) + x\left(\frac{\alpha^4}{\sigma^4}\right) + \frac{\kappa_0^2\alpha^6}{\sigma^4}\right)$$

100

respectively and

$$B_k = \prod_{j \neq k}^{n} \frac{1}{b_j^2 - b_k^2}, \qquad b_j^2 \neq b_k, \qquad \sum_{k=0}^{n} B_k = 0 \qquad k = 0, 1, 2, 3$$

$$C_k = \prod_{j \neq k}^{n} \frac{1}{c_j^2 - c_k^2}, \qquad c_j^2 \neq c_k, \qquad \sum_{k=0}^{n} C_k = 0 \qquad k = 0, 1, 2, 3, 4$$

$$C_k = \frac{B_k \alpha^2}{1 - b_k^2 \alpha^2}, \qquad k = 0, 1, 2, 3$$

where $-c_4^2 = -1$ and $\sum_0^3 d_k^2 = \sum_0^3 b_k^2 k = \sum_0^3 c_k^2$. The corresponding chemical potential is

$$\beta \mu_\pm = 2 \ln \rho \Lambda^d - \frac{\kappa_0^2 l_B \alpha^5}{\sigma^4} \sum_{k=0}^{4} \frac{C_k}{c_k}$$

Now we may write the pressure as

$$\beta p \approx 2\rho - \frac{1}{2} \left[\frac{\alpha^{-3}}{6\pi} \sum_{k=0}^{3} (d_k^3 - b_k^3) - \frac{\kappa_0^2 \alpha^3}{4\pi \sigma^4} \sum_{k=0}^{3} -B_k b_k \right] \qquad (4.3)$$

4.3.3 Results/Discussion
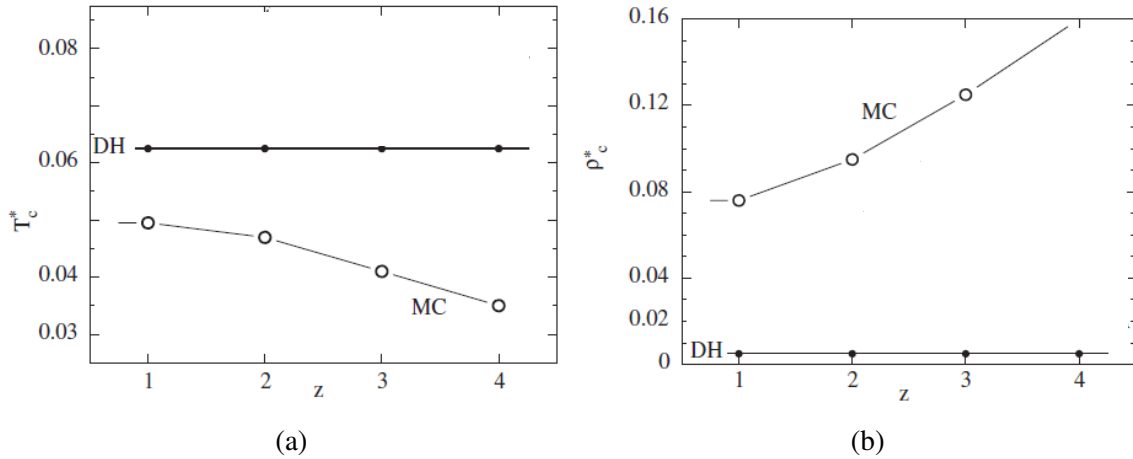
Figure 4.3: The critical (a) temperatures and (b) densities are shown for the RPM where the Debye Hückel approach is compared to Monte Carlo simulations for various values of the parameter z showing that DH theory is unchanged under different concentrations [6].

There is not a great deal of research into the smeared charge model and in particular the BSCM. To put this work in context with others we refer to Figures 4.3a and 4.3b where for the RPM we see that the Monte Carlo results for the critical temperature and density is overpredicted and underpredicted respectively by the Debye Hückel theory as a result of neglecting the effect of ion pairing [2]. Therefore, first we will examine the Debye Hückel results and then we will endeavour to use the splitting theory modification to bridge the gap between Debye Hückel theory and the Monte Carlo predictions. There is no reason that the unusual choice of a Bessel distribution will have a different effect other than facilitating the mathematical expressions.

Debye-Hückel Results
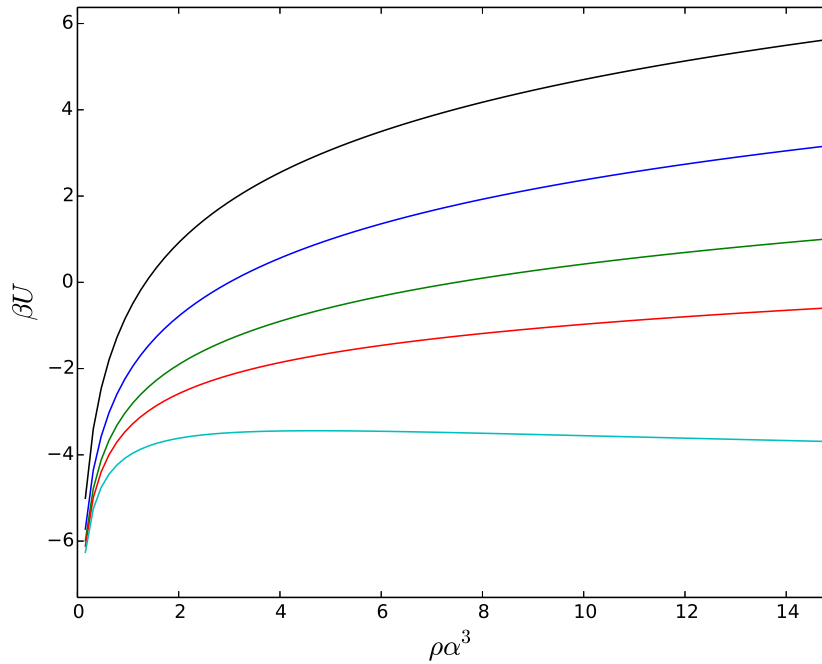
Figure 4.4: Debye-Hückel chemical potential of the symmetric Bessel charges. The black, blue, green red and light blue lines correspond to $l_B/\alpha = 1, 5, 10, 15$ and 30 respectively

Figure 4.4 shows that decreasing the temperature of the system causes the chemical potential to decrease, therefore showing, as expected that at lower temperatures the system will be less welcoming of increasing the number of particles. We see that increasing the packing fraction $\rho\alpha^3$ causes the chemical energy to become less and less negative which makes sense as the particles in the system are getting closer and closer together. We see that the chemical potential of lower temperatures seem to 'level out' earlier in terms of $\rho\alpha^3$ than higher temperatures which is a result of less interation between the ions.
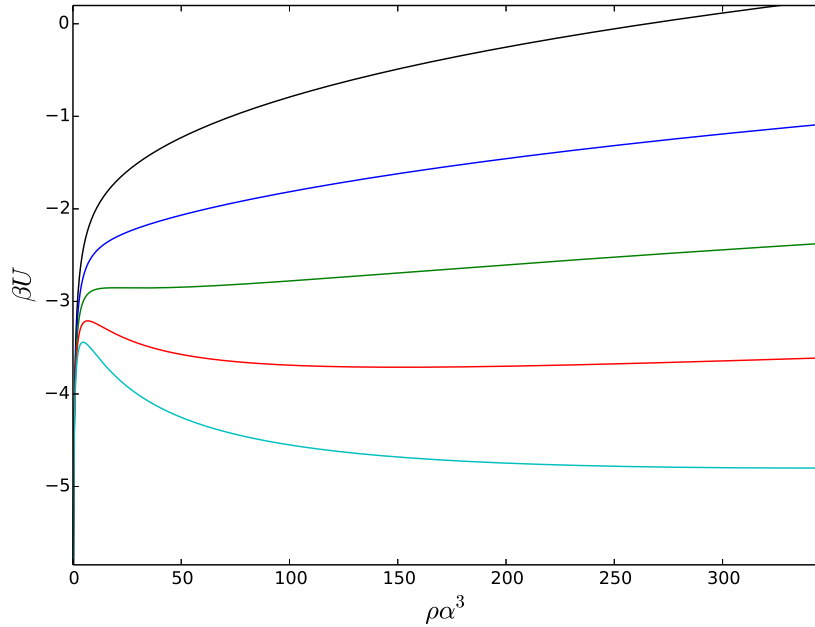
Figure 4.5: Debye-Hückel chemical potential of the symmetric Bessel charges. The black, blue, green red and light blue lines correspond to $l_B/\alpha = 20, 22.5, 25, 27.5$ and 30 respectively

However looking at much larger $\rho\alpha^3$ in Figure 4.5 we see an upper and peak of sorts forming around $\rho\alpha^3$ for $l_B/\alpha = 25, 27.5$ and 30. Here the chemical potential seems rise to a critical point before gradually sinking as $\rho\alpha^3$ becomes comparitvely massive. A possible reason for this could be the charge distributions of each of the counterions becoming more and more overlapped with the others. The packing fraction $\rho\alpha^3$ approaching unity indicates that the charge distributions are 'on top of' each other, therefore when we reach a point of $\rho\alpha^3 \gg 1$ we stop to see any grand changes as the system becomes no more or less welcoming to incoming particles. However, it makes more sense to focus on $\rho\alpha^3 < 15$ to keep this in line with other studies [7–9, 12].
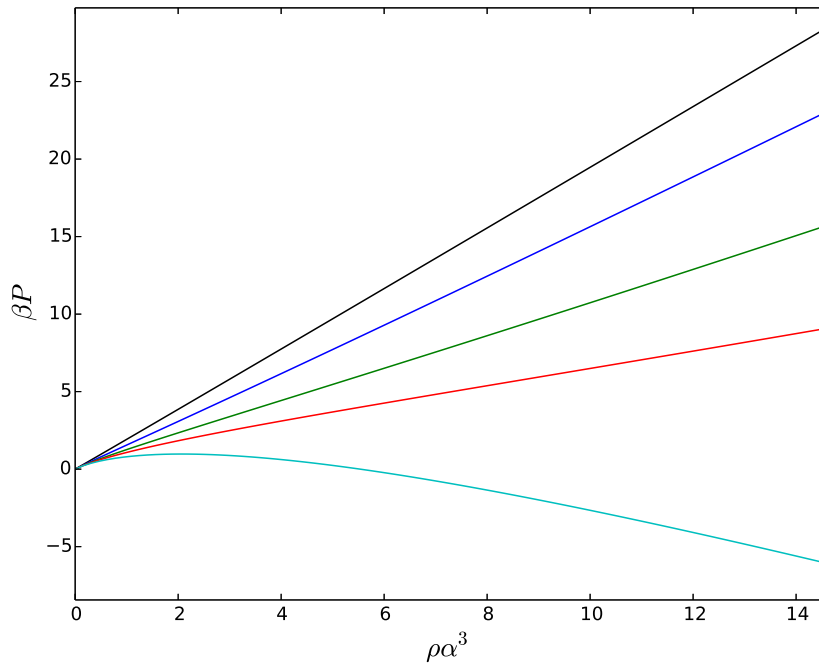
Figure 4.6: Debye-Hückel pressure of the symmetric Bessel charges. The black, blue, green red and light blue lines correspond to $l_B/\alpha = 1, 5, 10, 15$ and 30 respectively

Analysing the system pressure under the same conditions as Figure 4.4 we see that under the lowest temperature/highest l_B/α shows an increasingly negative pressure at approximately $\rho\alpha^3 > 3$. A negative pressure in this context can indicate either that there is a problem with the model or that a phase change is occurring. Due to the temperatures present it is likely that if a phase change is occurring then the ions in the system are moving from a solid phase into a liquid phase. This illustrates an interesting development as it is assumed that there will be no phase transition in the BSCM [11].
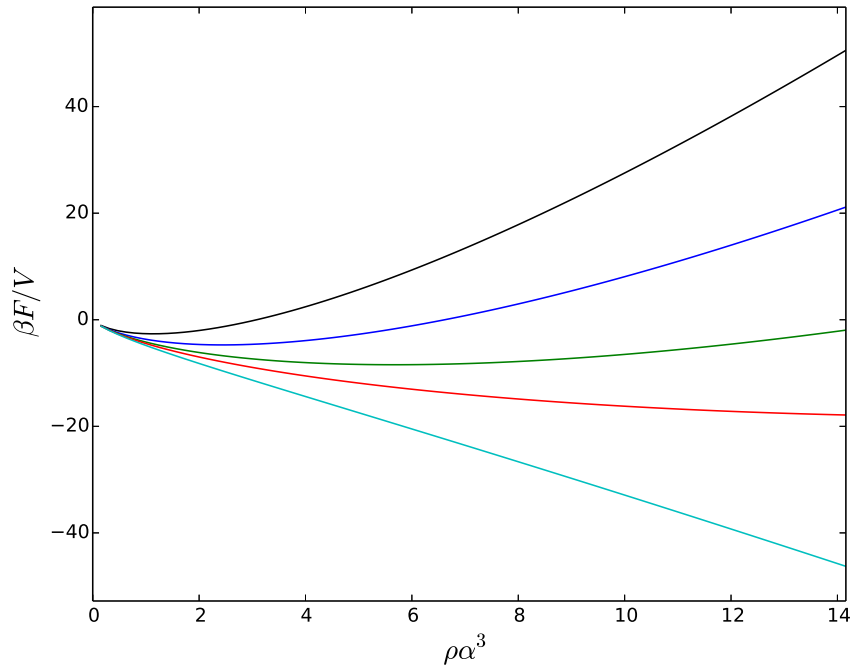
Figure 4.7: Debye-Hückel Helmholtz free energy of the symmetric Bessel charges. The black, blue, green red and light blue lines correspond to $l_B/\alpha = 1$, 5, 10, 15 and 30 respectively

Finally, we show the Debye-Hückel Helmholtz free energy in Figure 4.7 which shows an inverse trend to 4.6 where a minimum appears to form at increasing $\rho\alpha^3$'s as l_B/α increases. This is likely due it being energetically favourable for the ions in the system to be a certain distance apart. Here it seems that this minimum occurs at an approximate level where the packing fraction is equal to the strength of electrostatic interactions. Therefore as the interactions get weaker with a lower temperature/large ion size, a higher packing fraction is required which means that the ions must be pushed closer together for the system to be energetically favourable. Then once $\rho\alpha^3$ passes l_B/α the system becomes more tightly packed and it becomes less optimal. This is likely a result of the charge clouds becoming more and more overlapped with one another restricting the movement of ions around the system. However, another possible explanation could be a phase change

occurring as mentioned previously. The Debye-Hückel results show indications of phase changes in the system, we now move on to the splitting theory to examine whether the hypothesis of the splitting theory bringing the Debye-Hückel results more in line with the trends noticed in the results of Figures 4.3a and 4.3b.

Splitting Results

We now examine the effect of including the correlation hole in our calculations by comparing the splitting results to the Debye-Hückel results in the previous section. We will use an ansatz for the size of the correlation hole where it is defined as being equal to the size of each ion i.e. $\sigma = \alpha$. As defined in Section 3.6, setting the value $\sigma = 0$ returns the Debye-Hückel theory.
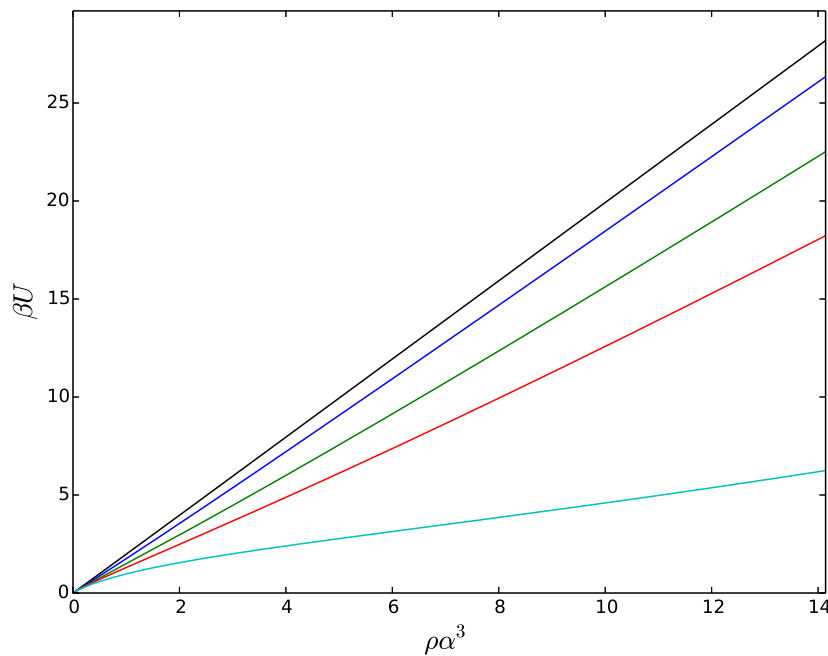
Figure 4.8: Splitting theory chemical potential of the symmetric Bessel charges. The black, blue, green red and light blue lines correspond to $l_B/\alpha = 1, 5, 10, 15$ and 30 respectively

Figure 4.8, when compared to its Debye-Hückel counterpart, Figure 4.4, shows similar trends in a higher chemical potential being returned with higher temperatures i.e. lower l_B/α's. However, one major difference we can observe is that we do not see the chemical potential 'levelling off' as the packing fraction increases, instead we see a constant rise over a similar scale to Figure 4.4. This could be because the splitting theory has the effect of keeping the oppositely charged ions a certain distance away from each other which in turn discourages ion pairs from forming in general.
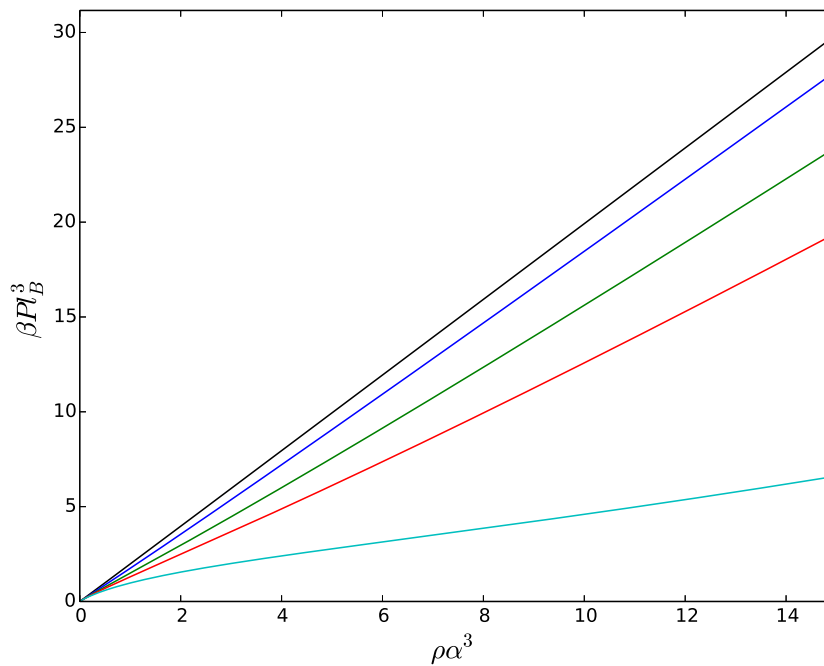
Figure 4.9: Splitting theory system pressure of the symmetric Bessel charges where the value of the splitting parameter has been set to the ansatz $\sigma = \alpha$. The black, blue, green red and light blue lines correspond to $l_B/\alpha = 1, 5, 10, 15$ and 30 respectively

Under similar conditions to Figure 4.6, we see that the splitting theory system pressure in Figure 4.9. As a direct comparison we see no negative pressure in this region, indicating that within this $\rho\alpha^3$ there is no phase change for the l_B/α mentioned. This is as expected and helps our original hypothesis as Figure 4.10 will show.
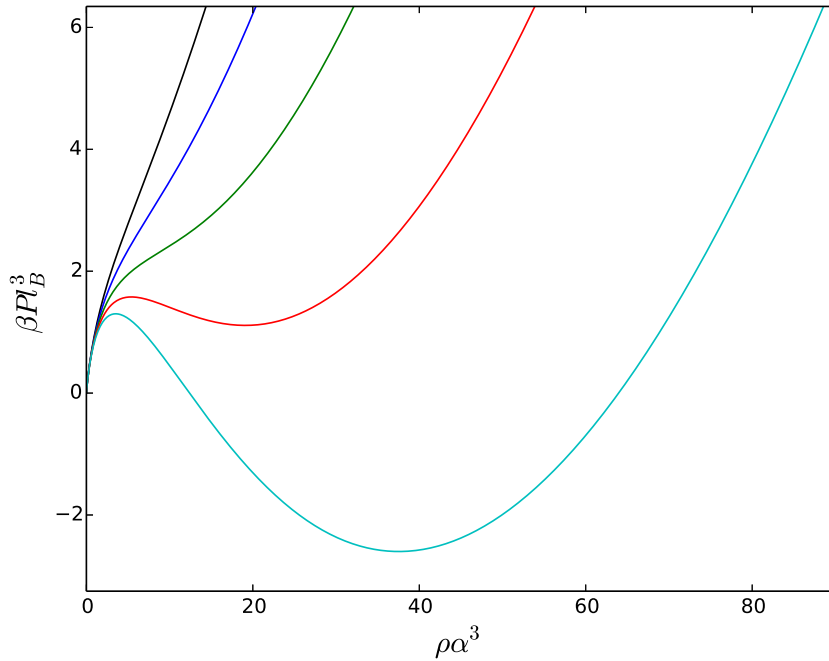
Figure 4.10: Splitting theory system pressure of the symmetric Bessel charges where the value of the splitting parameter has been set to the ansatz $\sigma = \alpha$. The black, blue, green red and light blue lines correspond to $l_B/\alpha = 1, 5, 10, 15$ and 30 respectively

Now, Figure 4.10 shows a phase change occurring at higher $\rho\alpha^3$'s and higher l_B/α's than the Debye Huckel models with which parallels may be drawn with Figures 4.3a and 4.3b where higher critical densities and lower critical temperatures are found via simulations than the Debye-Hückel results. There appears to be a phase transition here for $l_B/\alpha = 15$ and 30. Therefore, although we were unable to simulate this model, we can assume that the splitting theory is bridging the gap between the Debye-Hückel models and the simulations shown in Figures 4.3a and 4.3b. We also see that the lower temperatures mean that the phase transitions occur over a much larger range of $\rho\alpha^3$. However, it would be interesting to note how much of this is due to our choice of the size of the correlation hole, σ. Being able to optimize σ for this system would greatly help the accuracy of this model.

(a) $l_B/\alpha = 1$ (b) $l_B/\alpha = 40$

Figure 4.11: Splitting theory system pressure of the symmetric Bessel charges. Here, the size of the charges is kept constant whilst the value of the splitting parameter σ is varied. The black, blue, green red and cyan coloured lines correspond to $\sigma/\alpha = 1, 10, 30, 50$ and 100 respectively

As the value of the splitting parameter σ is relatively arbitrary we are free to choose one which best suits our calculations. We see that in Figures 4.11a and 4.11b that at much lower temperatures the choice of σ/α can be significant. Figure 4.11b shows that increasing the value of σ/α causes dramatic changes in the behaviour of the system. It is seen that increasing σ/α past 10 causes a negative pressure to be seen in the system, this makes sense as an increase in the splitting parameter of this magnitude would cause most ions in the system to be treated as energetically unfavourable to be within the splitting region, causing unpredictable results in the theoretical approach.

Figure 4.12: The Splitting theory Helmholtz free energy of the symmetric Bessel charges is shown varying against (a) $\rho\alpha^3$ and (b) σ/α The black, blue, green red and cyan coloured lines correspond to $l_B/\alpha = 1, 5, 10, 15$ and 30 respectively whilst $\sigma/\alpha = l_B/\alpha$ in (a)

This behaviour is seen further in Figures 4.12a and 4.12b. Where, setting $\sigma/\alpha = l_B/\alpha$ causes the free energy to decrease more and more as l_B/α is increased. Increasing σ/α in Figure 4.12b leads to a uniformly negative Helmholtz Free energy. As the splitting parameter increases the effect of l_B/α decreases due to all ions in the system being considered inside the splitting range.

4.4   Gaussian Smeared Charge Electrolyes

Instead of the Bessel smeared charge distribution of the BSCM, we now use the Gaussian form for both the cation and anions.

$$Q_\pm(\mathbf{r}) = q \exp\left(-\frac{r^2}{2\alpha^2}\right) \qquad \longleftrightarrow \qquad \hat{Q}_\pm(\mathbf{r}) = q \exp\left(-\frac{p^2\alpha^2}{2}\right)$$

simply replacing the Bessel charge distribution in the screening function $\mathcal{K}(p)$ allows the thermodynamic properties derived in the previous sections to be recreated. In this section the Bessel smeared charge is replaced by a Gaussian charge distribution. This allows for Molecular Dynamics (MD) simulations to approximate the system and should allow for

more detailed analysis into the behaviour of the symmetric electrolyte. Another advantage of this systems is that there has been a small amount of work done in this area which will allow us to compare and contrast our results with those in the available literature, in particular the work of Warren et al [12], which uses a combination of MC, HNC and RPA to model the GSCM at different l_B/α.

4.4.1 Simulation Details

Molecular dynamics (MD) simulations were carried out using the GROMACS 4.6.5 [125] package. All the systems consisted of simulation boxes containing 5324 molecules and were simulated for 2 ns. The particles are spread out by the use of a random number generator. In all the cases the simulation times refer to runs performed starting from equilibrated systems. The equations of motion were integrated by means of the leap-frog algorithm [126] with a time step of $5\,\mathrm{fs}$. The simulations were performed with the NVT ensemble. The Nosé-Hoover thermostat [127, 128], with a time constant of $10\,\mathrm{ps}$, is used for temperature coupling. Long-range electrostatics were treated with the particle mesh Ewald [129] (PME) method with a truncation at 5nm, and a spacing for the PME grid size of $128 \times 128 \times 128\,\mathrm{nm}$. The potentials used were as defined above for the GSCM. Finally, cubic periodic boundary conditions were used in every case.

4.4.2 Results/Discussion

We will begin by discussing $l_B/\alpha = 1$ and 10 for the most part as this will allow us to frame our discussion around the work of Warren et al [12] which also studies these values. Then after validating that our simulations and theory can replicate results shown in the literature we will endeavour to explore differing temperatures to fully examine the system. Figures 4.13 and 4.14 show MD simulations as described in Section 4.4.1 for $l_B/\alpha = 1$ and 10

respectively.
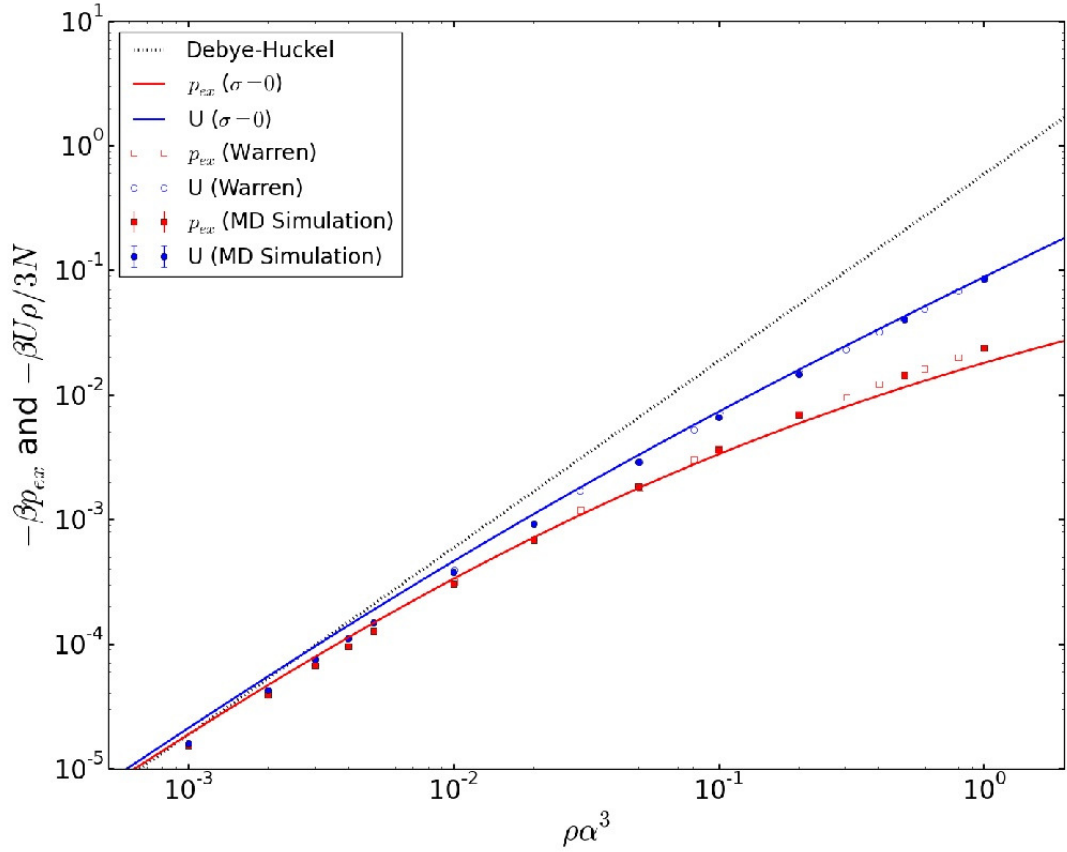
Figure 4.13: Here the excess pressure p^{ex} (red lines) and Internal energy $U/3V$ is shown for $l_B/\alpha = 1$ for Warren et al [12] (Transparent squares and circles respectively). The MD simulation work described in Section 4.4.1 is represented by the solid squares and circles respectively. The solid lines represent the Debye-Hückel theory which is identical to the Splitting theory when $\sigma = 0$

The MD simulations are seen to be in good agreement with the MC simulation work of Warren et al [12] for both the excess pressure and internal energy where $p^{ex} = U/3V$ due to Clausius' virial theorem applied to point charges interacting with the Coulomb potential [130]. We see the DH limiting law for point charges $p^{ex} = -\kappa_b^3/24\pi$, both the excess pressure and internal energy trend towards this law as $\rho\alpha^3$ decreases.
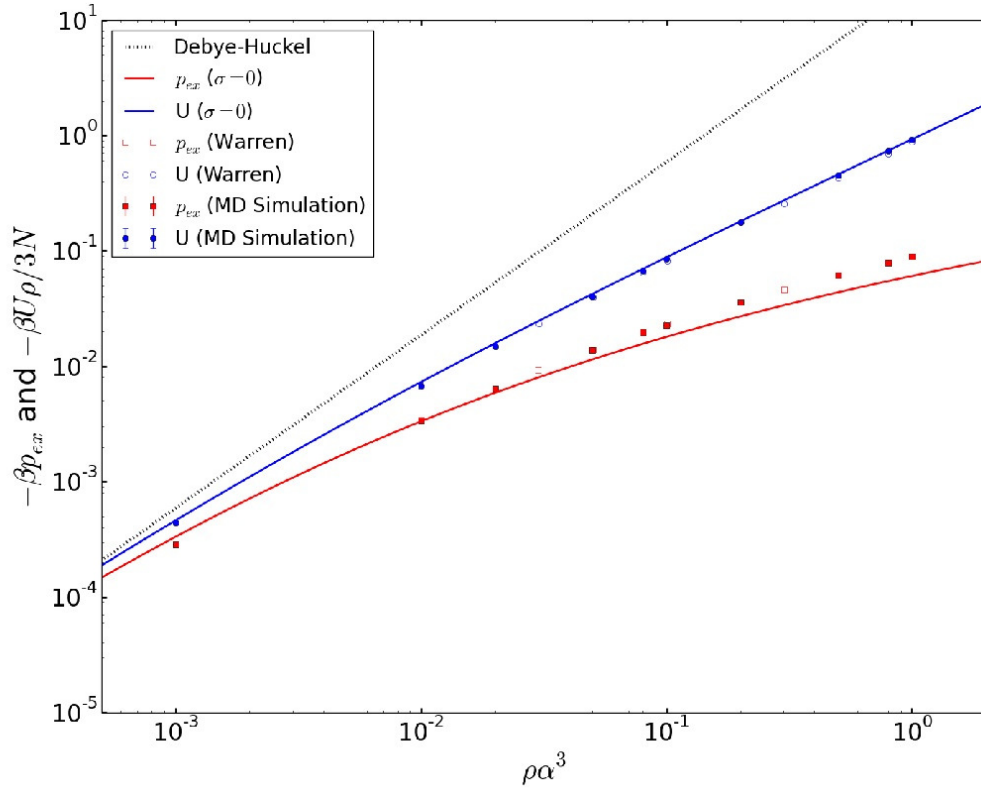
Figure 4.14: Here the excess pressure p^{ex} (red lines) and Internal energy $U/3V$ is shown for $l_B/\alpha = 10$ for Warren et al [12] (Transparent squares and circles respectively). The MD simulation work described in Section 4.4.1 is represented by the solid squares and circles respectively. The solid lines represent the Debye-Hückel theory which is identical to the Splitting theory when $\sigma = 0$

We also see the solid lines of the analytical Splitting theory derived from Section 3.7. The agreement between this, plus the MC and MD simulations gives credence to the analytical form of the URPM. As the temperature decreases, i.e. l_B/α increases from 1 to 10, we see a rise in the excess pressure as expected from the analytical formulae of the BSCM. From this point it is valuable to investigate the radial distribution functions ($g(r)$'s) of the system to examine the behaviour of the ions in the system through the simulations.
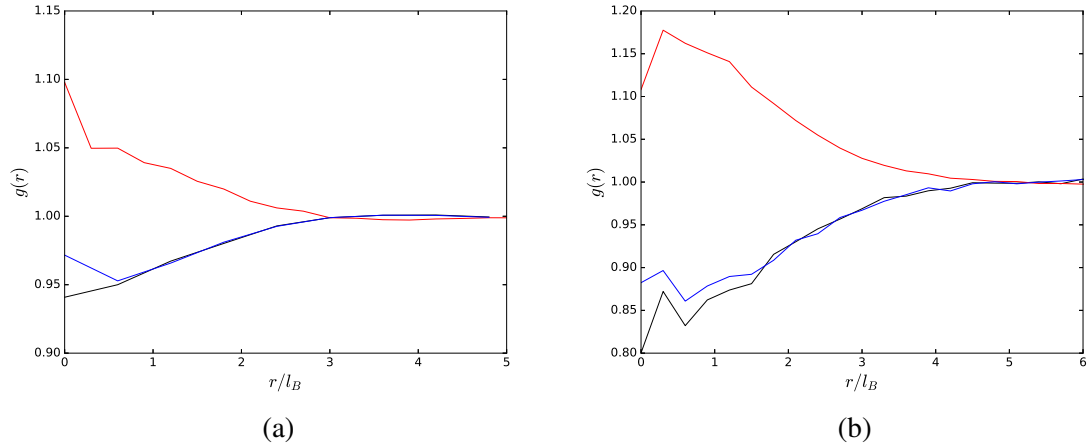
Figure 4.15: $g(r)$ for the Gaussian URPM where $l_B/\alpha = 1$ and $\rho\alpha^3 = $ (a) 1 and (b) 0.1. The red line corresponds to the $\pm$ cations and anions whilst the blue and black lines refer to the cations (+) and anions (-) respectively.

Figures 4.15 and 4.16 show the $g(r)$'s of the system at $l_B/\alpha = 1$ where $\rho\alpha^3 = 1$ and 0.1 respectively. As we are considering a symmetric electrolyte it is natural to assume that the interactions between the cations (++) would be identical to that of the anions (--) and this is shown in both Figures 4.15 and 4.16 except at the shortest distances where the rdf's become less reliable. We see that as r decreases, meaning we are considering the probability if the ions being close to one another, both the cations and anions show a lower probability of proximity to a like charged ion. This is understandable, in the RPM there would be a much stronger repulsion here due to the hard cores of that system. The penetrable ions of the URPM still have that repulsive characteristic but not at the strength of the hard core model. This repulsion appears slightly stronger at the lower density. Considering the interaction between oppositely charged ions (+-) we see that there is a light attraction between the ions at both values of $\rho\alpha^3$ observed. However, this is not enough to indicate ion pairing in the system under these conditions.
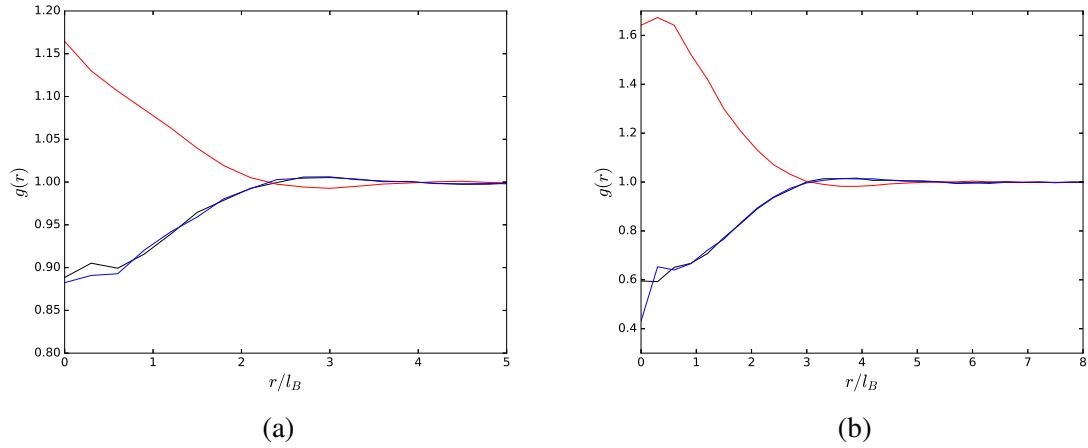
Figure 4.16: $g(r)$ for the Gaussian URPM where $l_B/\alpha = 10$ and $\rho\alpha^3 = $ (a) 1 and (b) 0.1. The red line corresponds to the $\pm$ cations and anions whilst the blue and black lines refer to the cations (+) and anions (-) respectively.

Similar behaviour is observed for $l_B/\alpha = 10$ in Figures 4.16a and 4.16b which represent $\rho\alpha^3 = 1$ and 0.1 respectively. However, at this lower temperature we see the oppositely charged ions in the system becoming closer to one another indicating that there is a higher probability of ion pairing under these conditions, again the less tightly packed the ions are in the system, the more likely the ions are to find a settled position within the system as there will be less interactions between the ions.
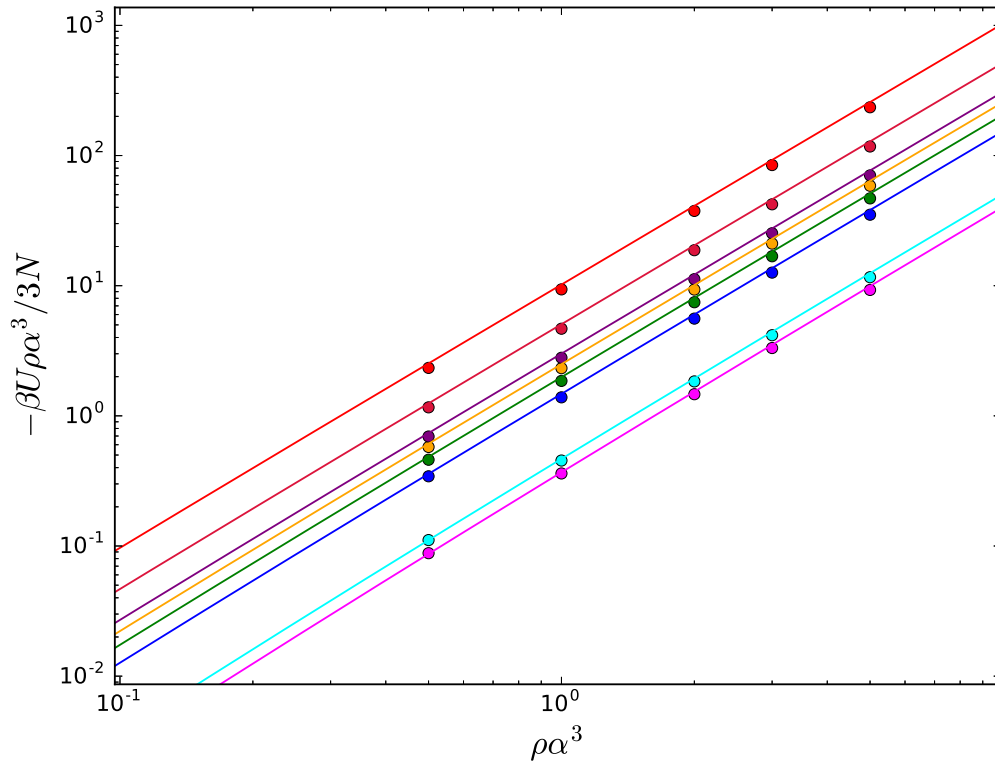
Figure 4.17: The Internal energy $U/3V$ is shown for $l_B/\alpha = 4, 5, 15, 20, 25, 30, 50$ and 100 (from bottom to top). The MD simulation work described in Section 4.4.1 is represented by the solid circles. The solid lines represent the Debye-Hückel theory which is identical to the Splitting theory when $\sigma = 0$

As Figures 4.13 and 4.14 show that the Debye-Hückel theory and the MD simulations match the MC simulations of Warren et al, [12]. Therefore we can have confidence in examining the system at lower temperatures. Figure 4.17 shows the internal energy of the URPM at $l_B/\alpha = 4, 5, 15, 20, 25, 30, 50$ and 100. It is seen that there is a consistent over-prediction in the Debye Hückel theory as the packing fraction is increased. This over prediction appears to become more pronounced as l_B/α increases. As the temperature in the system decreases, there does not appear to be a discernible change in the system with the internal energy increasing in line with the increase in l_B/α.

4.5   Conclusions

Examining the symmetric BSCM for the Debye-Hückel model shows some interesting, yet predictable results. Phase changes occurring at relatively high temperatures and low densities compared with different simulations as shown by Figures 4.3a and 4.3b. This is understandable as with the hard cores of the RPM removed, the ions are able to pass through each other and are less confined by the excluded volume effects of the RPM. The splitting theory has been deployed in the URPM for the first time with the intention of bridging the gap between the Debye Hückel theory and simulated results for the RPM. Analytical forms for the thermodynamic properties of the URPM were tested and produced valuable insights into the phase behaviour of the URPM. Notably that a phase change appears to be taking place at higher temperatures depending on the value of $\rho\alpha^3$. This phase change is potentially analogous to the one shown by Coslovich et al. Using a different charge cloud than Coslovich et al [7, 10] means that it is difficult to compare both approaches. However comparison with Warren et al [11] gives the BSCM some context. There was also no critical value for the splitting parameter σ found which suggests that a deeper investigation into the BSCM is required to ascertain the validity of the Splitting theory within this model.

Moving on to the Gaussian GSCM, very good agreement was found between this work (analytical and simulation) and the MC simulations of Warren et al [11]. There was also an examination of how the particles more around the system the the $g(r)$'s of Figures 4.15 and 4.16 where it was observed that there are light repulsions between the like charged ions and the reverse is shown in the oppositely charged ions. This behaviour is, of course, expected but it is useful to show that the ultrasoft model still has these repulsions/attractions at lower distances, just not with the same strength of the hard core models.

Figure 4.1 shows the differing critical points and vapour liquid coexistence curves for

the GSCM and BSCM. Interestingly there is a noticeable difference between the two, granted that there are only RPA results available for the BSCM. It was originally thought that changing the cloud was an arbitrary decision to aid calculations. However this, coupled with the differing phase behaviour between the RPM and the URPM, mean that further study on this system is required. The clustering phenomena alluded to by this phase behaviour is discussed in more detail in Chapter 7

Chapter 5

Asymmetric Electrolytes

5.1 Overview

Most electrolyte theories consider the individual cations and anions to be of identical size, charge and valency. Whilst this makes analytical methods for modelling electrolytes simpler to obtain than in the Symmetric Chapter 4 , it is not the most realistic model as most real life electrolytes are asymmetric. This chapter will present a short literature review on the ARPM and the beginnings of the UARPM before modifying the Debye Hückel and Splitting theories presented in chapters 3 and 4. Then we will investigate the analytical forms of the BSCM before performing simulation work with the GSCM. This chapter introduces the idea of an ultrasoft asymmetric restricted primitive model approaching the behaviour of the classical Once Component Plasma under certain conditions of asymmetric charge cloud size which will be the main focus of Chapter 6

5.2 Theory

The theory for the UARPM takes a similar form to that of the Symmetric electrolyte in Chapter 4. The main difference between the two will be that the UARPM consists of cations and anions with different properties. For simplicity we will choose to compare Smeared Charge cations with point charge anions.
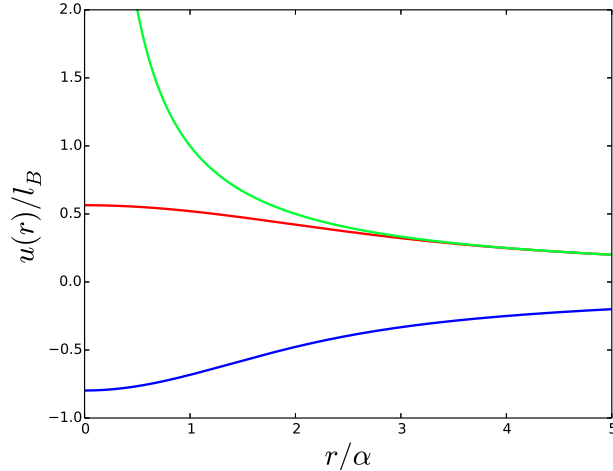
Figure 5.1: Interaction potential between: (i) two symmetric cations (red line), (ii) two anions (green line), and (iii) an asymmetric cation and a point charge anion (blue line).

Figure 5.1 shows the potential of an asymmetric cation and point charge anion and the comparison to the symmetric model. This shows that this model will also avoid the problem of point charges collapsing on top of each other [88] which motivates the URPM.

Mathematically, the main difference between this work and the symmetric URPM is that there will be two separate forms of the charge distribution; $Q_+(p)$ and $Q_-(p)$ for the positive and negative ions respectively. Therefore we may write the screening function $\mathcal{K}(p)$ as

$$\mathcal{K}(p) = \beta[\rho_+|Q_+(p)|^2 + \rho_-|Q_-(p)|^2]$$

therefore the screening function $\kappa^2(p)$ becomes

$$\kappa^2(p) = \frac{1}{2}\left[\frac{\kappa_{0+}^2 Z^2}{1 + p^2\alpha^2} + \kappa_{0-}^2\right]$$

where $\kappa_{0+}^2 = 8\pi\rho_+ l_B$, $\kappa_{0-}^2 = 8\pi\rho_- l_B$ and $\frac{\kappa_{0+}^2}{\kappa_{0-}^2} = \frac{\rho_+}{\rho_-} = \frac{1}{Z}$. Therefore the Debye-Hückel and Splitting models keep the same formulae for the thermodynamic properties (Chapter 3) with this modification to the screening function. We are now in a position to investigate the BSCM analytically and the GSCM through simulations to create an analogous work to the symmetric URPM

5.3 Bessel Smeared Charge Electrolytes

Using similar methods to section 4.3 we now adapt the URPM to consider the case of asymmetric Bessel smeared charge electrolytes. This is briefly touched upon by Coslovich et al [7] for the Gaussian smeared charge model which will be discussed in Section 5.4 but the Bessel model has not been examined in the literature. Therefore the results displayed here are novel in nature.

5.3.1 Analytical Formulae

We now consider an electrolyte consisting of cations with a Bessel charge distribution $Q_+(r)$ and anions consisting of point charges of magnitude $-q$. We define our charge distributions $Q_+(p)$ and $Q_-(p)$ as

$$Q_+(\mathbf{r}) = q(2\pi^2\alpha^2 r)^{-1} K_1(r/\alpha) \qquad \longleftrightarrow \qquad \hat{Q}_+(\mathbf{p}) = q(1 + p^2\alpha^2)^{-1/2} \qquad (5.1)$$

$$Q_-(\mathbf{r}) = -q\delta^d(\mathbf{r}) \qquad \longleftrightarrow \qquad \hat{Q}_-(\mathbf{p}) = -q \qquad (5.2)$$

where α_k describes the size of the 'puffy' cations and $\alpha = 0$ for point charges.

Debye-Hückel Theory

Firstly, the system will be discussed with reference to the standard Debye-Hückel Theory before modifying to include the splitting theory. Therefore the overall Helmholtz free energy may be written as

$$\frac{\beta F(\rho)}{V} \approx \rho_+ \left[\ln(\rho_+ \Lambda_+^d) - 1 - \frac{\kappa_{0-}^2 l_B \alpha}{4} \sum_{k=0}^{2} \frac{W_k}{w_k} \right] + \rho_- \left[\ln(\rho_- \Lambda_-^d +) - 1 - \frac{\kappa_{0-}^2 l_B \alpha}{4} \sum_{k=0}^{1} \frac{Y_k}{y_k} \right]$$
$$+ \frac{1}{2} \left[\frac{\alpha^{-3}}{6\pi} \sum_{k=0}^{1} (x_k^3 - y_k^3) - \frac{\kappa_{0-}^2}{8\alpha\pi} \sum_{k=0}^{1} \left(2 - y_k^2 \alpha^2 \right) Y_k y_k \right]$$

where $-x_k^2$, $-y_k^2$ and $-w_k^2$ are the roots of

$$x^2 + x$$
$$x^2 + x \left(1 + \frac{1}{2}\kappa_{0-}^2 \alpha^2 \right) + \frac{\alpha^2}{2} \left(\kappa_{0-}^2 + \kappa_{0+}^2 \right)$$
$$(1 + x^2) \left(x^2 + x \left(1 + \frac{1}{2}\alpha^2 \kappa_{0-}^2 \right) + \frac{\alpha^2}{2} \left(\kappa_{0+}^2 + \kappa_{0-}^2 \right) \right)$$

respectively and

$$Y_k = \prod_{j\neq k}^{n} \frac{1}{y_j^2 - y_k^2}, \quad W_k = \prod_{j\neq k}^{n} \frac{1}{w_j^2 - w_k^2} \quad , y_j \neq y_k, \quad w_j \neq w_k$$

where $\sum_{k=0}^{n} Y_k = \sum_{k=0}^{n} W_k = 0$ and $\sum_{0}^{n} a_k^2 = \sum_{0}^{n} y_k^2 = \sum_{0}^{n} w_k^2$.

The corresponding expressions for the species chemical potentials are

$$\beta\mu_+ = \ln\rho_+\Lambda_+^d - \frac{\kappa_{0-}^2 l_B \alpha}{4} \sum_{k=0}^{2} \frac{W_k}{w_k}$$

$$\beta\mu_- = \ln\rho_-\Lambda_-^d - \frac{\kappa_{0-}^2 l_B \alpha}{4} \sum_{k=0}^{1} \frac{Y_k}{y_k}$$

Now we may write the pressure as

$$\beta p \approx \rho_+ + \rho_- - \frac{1}{2}\left[\frac{\alpha^{-3}}{6\pi} \sum_{k=0}^{1}(x_k^3 - y_k^3) - \frac{\kappa_{0-}^2}{8\alpha\pi}\sum_{k=0}^{1}\left(2 - y_k^2\alpha^2\right)Y_k y_k \right] \qquad (5.3)$$

5.3.2 Splitting Theory

Modifying the above Debye-Hückel Theory to include the effects of the correlation hole discussed above yields the following results. The Helmholtz free energy is given by

$$\frac{\beta F(\rho)}{V} \approx \rho_+\left[\ln(\rho_+\Lambda_+^d) - 1 - \frac{\kappa_{0-}^2 l_B \alpha^5}{4\sigma^4}\sum_{k=0}^{4}\left(2 - c_k^2\right)\frac{C_k}{c_k} \right]$$

$$+ \rho_-\left[\ln(\rho_-\Lambda_-^d) - 1 - \frac{\kappa_{0-}^2 l_B \alpha^5}{4\sigma^4}\sum_{k=0}^{3}\left(2 - b_k^2\right)\frac{B_k}{b_k} \right]$$

$$+ \frac{1}{2}\left[\frac{1}{6\pi\alpha^3}\sum_{k=0}^{3}(a_k^3 - b_k^3) - \frac{\kappa_{0-}^2\alpha^3}{8\pi\sigma^4}\sum_{k=0}^{3}\left(2 - b_k^2\right)B_k b_k \right]$$

where $-a_k^2$, $-b_k^2$ and $-c_k^2$ are the roots of the polynomials

$$x^3 + x^2\left(\frac{\sigma^2\alpha^2 + \sigma^4}{\sigma^4}\right) + x\left(\frac{\alpha^4 + \sigma^2\alpha^2}{\sigma^4}\right) + \frac{\alpha^4}{\sigma^4}$$

$$x^4 + x^3\left(\frac{\sigma^2\alpha^2 + \sigma^4}{\sigma^4}\right) + x^2\left(\frac{\alpha^4 + \sigma^2\alpha^2}{\sigma^4}\right) + x\left(\frac{\alpha^4 + \frac{1}{2}\alpha^6\kappa_{0-}^2}{\sigma^4}\right) + \frac{\alpha^6(\kappa_{0+}^2 + \kappa_{0-}^2)}{2\sigma^4}$$

$$(x+1)\left(x^4 + x^3\left(\frac{\sigma^2\alpha^2 + \sigma^4}{\sigma^4}\right) + x^2\left(\frac{\alpha^4 + \sigma^2\alpha^2}{\sigma^4}\right) + x\left(\frac{\alpha^4 + \frac{1}{2}\alpha^6\kappa_{0-}^2}{\sigma^4}\right) + \frac{\alpha^6}{2}\left(\frac{\kappa_{0+}^2 + \kappa_{0-}^2}{\sigma^4}\right) \right)$$

respectively and $-b_0^2 \cdots - b_3^2 = -c_0^2 \cdots - c_3^2$ where $-c_4^2 = -1$ and

$$B_k = \prod_{j \neq k}^{n} \frac{1}{b_j^2 - b_k^2}, \qquad b_j \neq b_k, \qquad \sum_{k=0}^{n} B_k = 0 \qquad k = 0, 1, 2, 3$$

$$C_k = \prod_{j \neq k}^{n} \frac{1}{c_j^2 - c_k^2}, \qquad c_j \neq c_k, \qquad \sum_{k=0}^{n} C_k = 0 \qquad k = 0, 1, 2, 3, 4$$

$$\mathcal{B}_k = \frac{B_k \alpha^2}{1 - b_k^2 \alpha^2}, \qquad k = 0, 1, 2, 3$$

where $\sum_0^3 a_k^2 = \sum_0^3 b_k^2 k = \sum_0^3 c_k^2$.

The species chemical potentials are given by

$$\beta \mu_+ = \ln \rho_+ \Lambda_+^d - \frac{\kappa_{0-}^2 l_B \alpha^5}{4 \sigma^4} \sum_{k=0}^{4} \left(2 - c_k^2\right) \frac{C_k}{c_k}$$

$$\beta \mu_- = \ln \rho_- \Lambda_-^d - \frac{\kappa_{0-}^2 l_B \alpha^5}{4 \sigma^4} \sum_{k=0}^{3} \left(2 - b_k^2 \alpha^2\right) \frac{\mathcal{B}_k}{b_k}$$

Now we may write the pressure as

$$\beta p \approx \rho_+ + \rho_- - \frac{1}{2} \left[\frac{1}{6 \pi \alpha^3} \sum_{k=0}^{3} (a_k^3 - b_k^3) - \frac{\kappa_{0-}^2 \alpha^3}{8 \pi \sigma^4} \sum_{k=0}^{3} \left(2 - b_k^2\right) \mathcal{B}_k b_k \right]$$

5.3.3   Results/Discussion

To qualify our choice of σ in the splitting parameter, typically we would require a stationary point in the free energy, where

$$\frac{\partial \beta F / V}{\partial \sigma} = 0.$$

However, Figures 5.2a and 5.2b show no stationary points, other temperatures/densities have been investigated without any success. Therefore throughout we will use an ansatz of equating the correlation hole to the size of the charge cloud i.e. $\sigma = \alpha$. Figure 5.2a

shows a negative free energy which decreases as $\frac{l_B}{\alpha}$ increases before eventually levelling off.
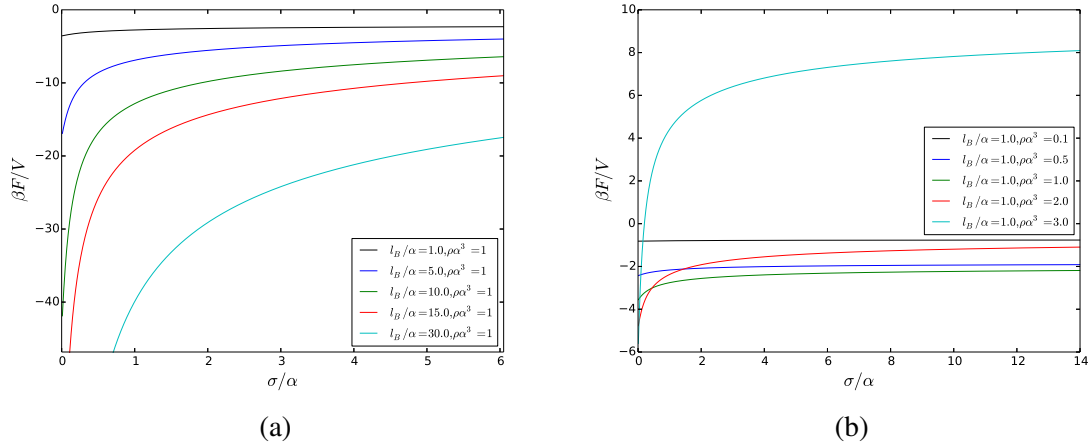
Figure 5.2: Free energy as a function of σ with a constant $\rho\alpha^3$ (a) and l_B/α (b), x axis - σ/α, y axis - $\frac{\beta F}{V}$

Using the ansatz value for σ, we may examine the chemical potential as a function of $\rho\alpha^3$. In Figures 5.3a, 5.3b, 5.4a and 5.4b, we see that as $\frac{l_B}{\alpha}$ decreases, so does its contribution to the chemical potential, leaving the ideal gas term as the major contribution to the chemical potential.
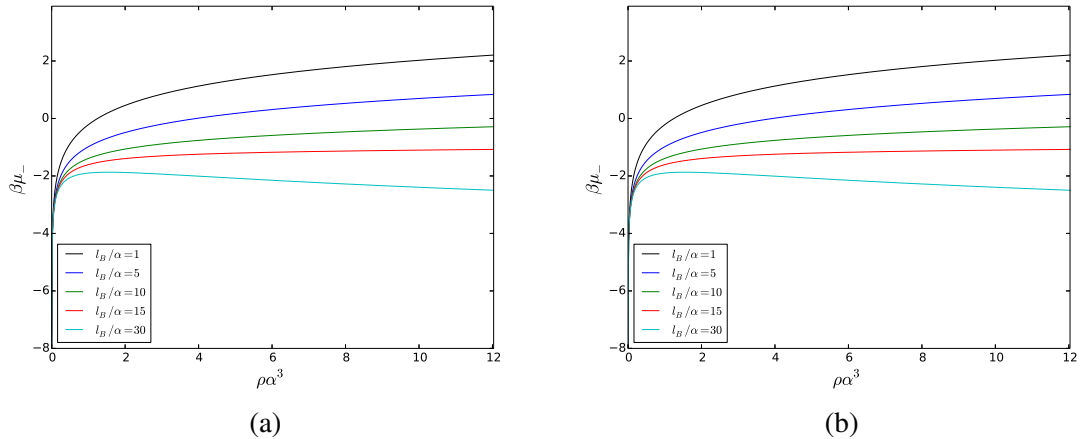
Figure 5.3: Chemical potential of puffy (a) and point (b) charges with the Debye Hückel theory.

However, Figures 5.4a and 5.4b show that increasing $\frac{l_B}{\alpha}$ has less of an effect with the splitting theory, as compared to the DH theory, while the ideal gas contribution still has the greatest influence on the chemical potential. Using the splitting theory gives a lower chemical potential overall.
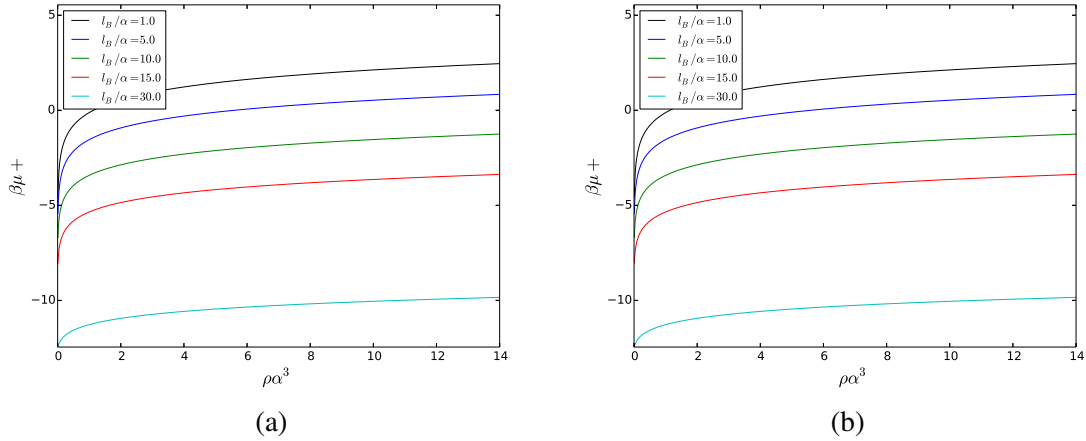
Figure 5.4: Chemical potential of puffy (a) and point (b) charges with the Splitting theory

The Debye-Hückel expression for the pressure shows that for all $\frac{l_B}{\alpha}$, the pressure is negative and is constantly decreasing indicating an non-physical system as shown in Figure 5.5a. However, once σ is introduced to the calculations we see a positive, rising pressure as $\rho_+ \alpha^3$ increases. Figure 5.5b shows the pressure increasing as the size of the puffy charges increases but the effect of this decreases as α gets larger as would be expected because as $\rho \alpha^3$ approaches 1 the charges consume all free space within the system.
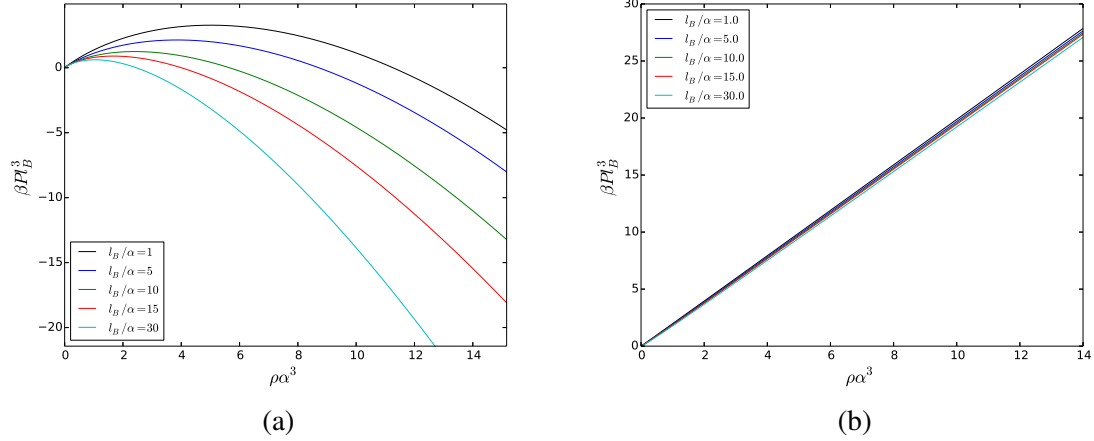
Figure 5.5: The Debye Hückel (a) and Splitting (b) pressures of the Bessel URPM. Here $\sigma = \alpha$

It is clear from Figure 5.5a that the DH theory cannot give a stable prediction of the behaviour of more complicated systems and the decrease of pressure with density indicates that the systems wants to phase separate (e.g. vapour-liquid co-existence)

5.4 Gaussian Smeared Charge Electrolyte

Moving on to the GSCM, we are able to present a brief theoretical approach followed by simulation data measured against, where possible, numerical methods such as the HNC, RPA and a numerical approach to the above theory.

5.4.1 General Formalism

The difference between this model and the BSCM is that the cations have a Gaussian charge distribution.

$$Q_+(\mathbf{r}) = q \exp\left(-\frac{r^2}{2\alpha^2}\right) \qquad \longleftrightarrow \qquad \hat{Q}_+(\mathbf{r}) = q \exp\left(-\frac{p^2\alpha^2}{2}\right),$$

while the anions are point charges

$$Q_-(\mathbf{r}) = -q\delta^d(\mathbf{r}) \qquad \longleftrightarrow \qquad \hat{Q}_-(\mathbf{p}) = -q.$$

Our standard Greens function is defined as

$$G(p) = \frac{4\pi}{p^2} \quad \longleftrightarrow \quad G(r) = \frac{1}{r} \quad \longleftrightarrow \quad G(r,r') = \frac{1}{|r-r'|}$$

whilst employing the Ewald method of 'splitting' requires us to define a G_l and a G_s to represent the long and short range interactions respectively. Using the Gaussian smeared charge model (GSCM) these Greens functions are defined as

$$G_l(p) = \frac{4\pi}{p^2} e^{-p^2\alpha^2} \quad \longleftrightarrow \quad G_l(r) = \frac{1}{r} erf\left(\frac{r}{2\alpha}\right)$$
$$G_s(p) = \frac{4\pi}{p^2}\left(1 - e^{-p^2\alpha^2}\right) \quad \longleftrightarrow \quad G_s(r) = \frac{1}{r} erfc\left(\frac{r}{2\alpha}\right)$$

This allows us to take a series approach to the pair potential of the chemical potential as shown in 5.6

$$\beta u(r) = \frac{l_B}{r} \mathrm{erf}(r/\alpha) \approx \frac{2l_B}{\alpha\sqrt{\pi}} \left[1 - \frac{1}{3}\left(\frac{r}{\alpha}\right)^2 + \frac{1}{10}\left(\frac{r}{\alpha}\right)^4 \cdots \right].$$
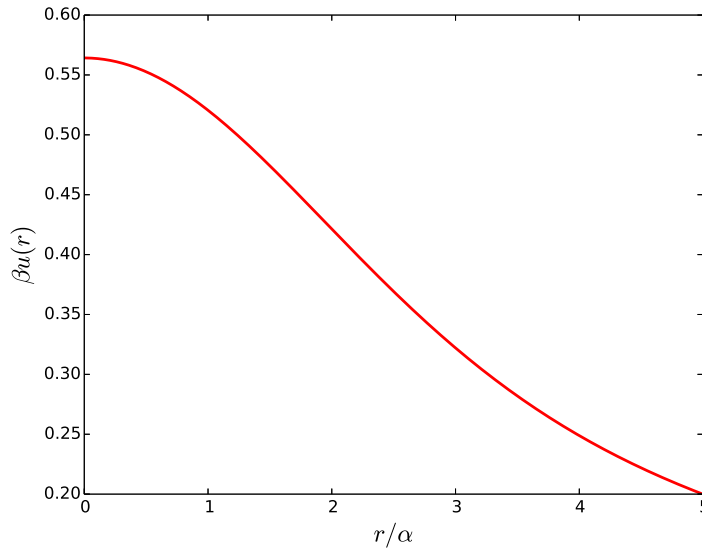
Figure 5.6: Pair potential for $l_B/\alpha = 1$

for the most part, however, we must use numerical and simulation methods

Simulation Details

Molecular dynamics (MD) simulations were carried out using the GROMACS 4.6.5 [125] package. All the systems consisted of simulation boxes containing 5324 molecules and were simulated for 2 ns. The particles are spread out by the use of a random number generator. In all the cases the simulation times refer to runs performed starting from equilibrated systems. The equations of motion were integrated by means of the leap-frog algorithm [126] with a time step of 5 fs. The simulations were performed with the NVT ensemble. The Nosé-Hoover thermostat [127, 128], with a time constant of 10 ps, is used for temperature coupling. Long-range electrostatics were treated with the particle mesh Ewald [129] (PME) method with a truncation at 5nm, and a spacing for the PME grid size of $128 \times 128 \times 128$ nm. The potentials used were as defined above for the GSCM. Finally, cubic periodic boundary conditions were used in every case.

5.4.2 Results/Discussion

The complicated nature of these analytical formulae mean that we now consider the numerical results of the HNC and RPA compared with the GROMACS simulations. Simulations were completed for various temperatures but for brevity results for $l_B/\alpha = 1$ will be shown.
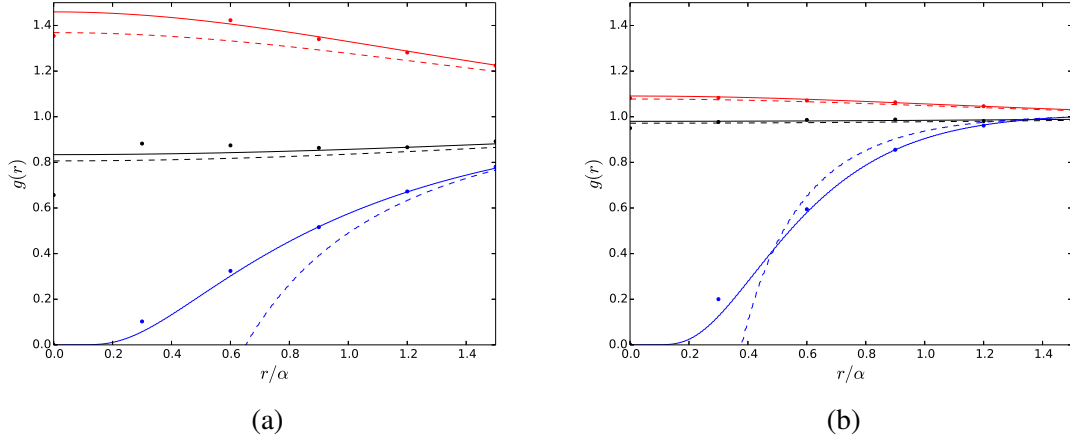
Figure 5.7: Radial distribution function for $l_B/\alpha = 1$ where the packing fraction $\rho\alpha^3 =$ (a) 0.050 and (b) 1.0. GROMACS (dots), HNC (solid line) and MSA (dashed line) results are compared where point -point (–) are blue, puffy-point (+-) are puffy-puffy (++) are red.

As $\rho\alpha^3$ increases towards and past 1 which is the point at which the smeared ion clouds will start to overlap one another, one expects the $g(r)$ of the puffy-puffy (++) interactions to increase towards 1 as shown in Figure 5.7b. Interestingly, we also see a trend which shows the $g(r)$ of the puffy-point (+-) interactions decreasing towards 1. In the much studied RPM model, the observed liquid-vapour phase transition occurs due to the formation of ion-ion pairs which condense under the influence of attractive forces. This is true for the symmetric URPM also [7, 10] where the soft penetrable cores allow ions to form increasingly strong bonds as the temperature is decreased. However, in the UARPM, the repulsive forces from the point charges are stronger than the binding attraction between

oppositely charged smeared and point charges. In the RPM and URPM, at low temperatures both fluids consist of predominantly ion pairs but the hard cores of the RPM prevent ions coming closer that α to one another. This gives a strict lower limit to the dipole strength [11] which does not exist for smeared charges. Therefore, it is entirely possible that the dipole-dipole attraction does not become strong enough in this case to cause condensation.

As the puffy ions are penetrable, when they begin to overlap each another the individual puffy ions will become indistinguishable from other puffy ions from the point of view of a nearby point charge. This is what leads to the postulation of a link between the UARPM and the classical one component plasma. In comparison to the numerical results, the HNC appears to fit the simulations well with some issues at very short distances whilst the RPA seem to under-predict the rdf, particularly at lower $\rho\alpha^3$ i.e. Figure 5.7a. An existing issue with the RPA is that it gives (unseen on Figures 5.7a and 5.7b) an non-physical negative rdf for the point-point interactions (- -).
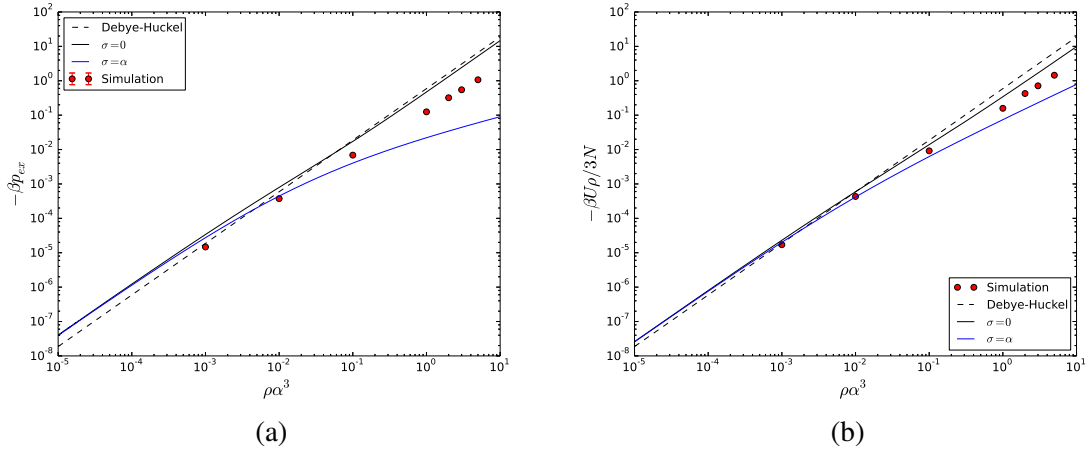
Figure 5.8: Numerical and simulation data for (a) the excess system pressure and (b) the internal energy of the system for $l_B/\alpha = 1$ as the packing fraction $\rho\alpha^3$ is increased. Also included is the standard Debye Hückel prediction

Figures 5.8a and 5.8b show GROMACS predictions for the pressure and interaction energy compared with the standard DH theory and predictions of the variational splitting theory for the system excess pressure and internal energy respectively. Two values for σ are shown, the ansatz of $\sigma = \alpha$ and $\sigma = 0$ which returns the modified DH theory. It is seen that as the packing fraction $\rho\alpha^3 \to 1$ and beyond that the splitting theory begins to deviate from the simulation results whilst as $\sigma = 0$ the numerical result follows that of the standard DH theory which is expected, the implication about the optimal value of σ could be somewhere between 0 and α.
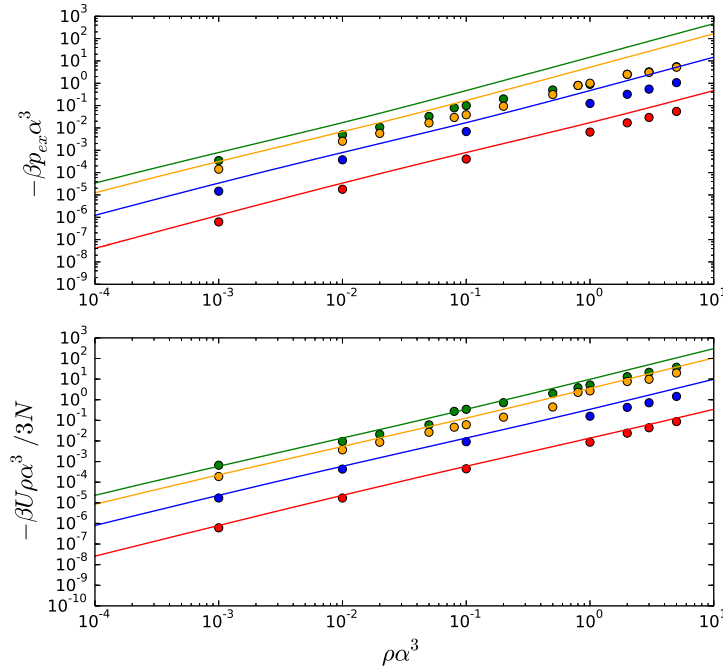
Figure 5.9: Internal energy and excess pressure of GROMACS simulations (Coloured Circles) as the packing fraction $\rho\alpha^3$ is increased. The lines are the Debye-Huckel theory for asymmetric electrolytes. The red, blue, yellow and green lines correspond to $l_B/\alpha = 0.1, 1, 5$ and 10 respectively

Figure 5.9 shows how different values of l_B/α behave as the packing fraction is increased. The simulations on the whole show an underprediction in the Debye-Hückel results. The higher values of $l_B/\alpha = 5, 10$ do not follow the same linear pattern as lower

two values studied. Interestingly, the values for both $l_B/\alpha = 5$ and 10 are very similar, if not identical at this point. This converging of the two different temperatures onto a unified direction indicates a structural change in the electrolytes under these conditions, particularly because this change is not present at higher temperatures. This is due to the afore mentioned clustering occurring in this region. At the point of cluster formation the internal energy become more negative as the system settles into this new clustered form. However, to fully ascertain what is happening in the system under these conditions it is useful take stock of how the system behaves dynamically.

5.4.3   Dynamic Results
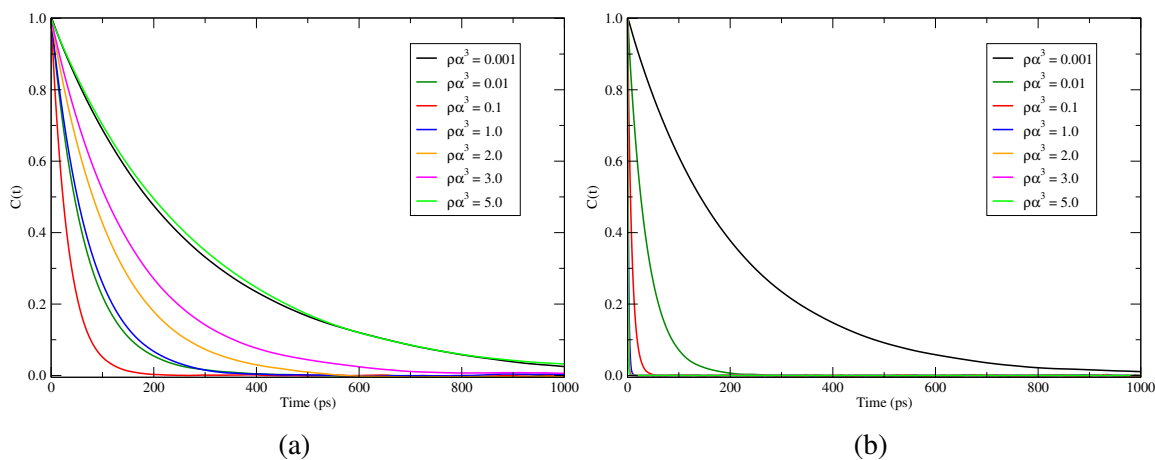
Figure 5.10: Simulation data for the auto-correlation function of (a) the smeared charges and (b) the point charges for $l_B/\alpha = 1$ as the packing fraction $\rho\alpha^3$ is increased.

The dynamic behaviour of the UARPM offers some clues as to what is happening in this model. Figures 5.10a and 5.10b show the velocity auto-correlation function for the puffy and point charges respectively derived from the GROMACs simulations.. This describes how the velocity of the ions changes over time. For the puffy charges, there is clearly a transition occurring around $\rho\alpha^3 = 0.1$. The velocity decorrelates faster as $\rho\alpha^3$ is increased up to 0.1 whereas past this density, the opposite is observed. Linking this back to Figures

5.7b and 5.7a we see the rdf of the UARPM at $l_B/\alpha = 1$ under go a change as $\rho\alpha^3$ increases. Here the puffy-puffy ions interact with one another less in the higher density. This could be what causes the strange reversal in the velocity decorrelation in Figure 5.10a. For the point charges, we see that past $\rho\alpha^3 = 0.1$ there is an almost instant drop in the velocity correlation function meaning the point charges are locked into position after this value.
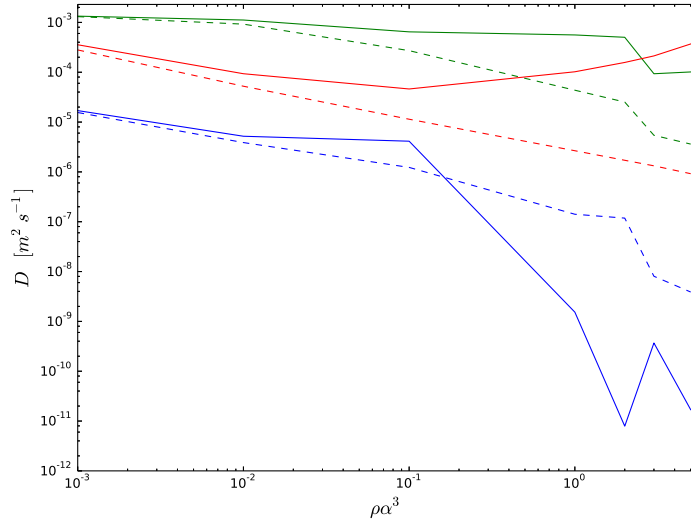
Figure 5.11: Simulation data for the Self-diffusion coefficient with the green, red and blue lines corresponding to $l_B/\alpha = 0.1, 1$ and 5 respectively. The solid lines represent the smeared charges while the dashed line represents the point charges.

Figure 5.11 shows the self diffusion coefficient for the UARPM at $l_B/\alpha = 0.1, 1, 5$. A massive drop in the self diffusion coefficient of puffy ions is observed in $l_B/\alpha = 5$ as $\rho\alpha^3$ becomes greater than 1. This is due to observed clustering in this model at lower temperatures. This clustering has become a prevalent part of the UARPM and is seen under several different conditions however the diffusion coefficient of the point charges do not seem as affected. Therefore it is essential that we are able to link the UARPM to a well studied model such as the OCP to validate our results. We expect that as the smeared charge becomes sufficiently large in comparison to the point charges that the system will

approach the behaviour of the OCP. Due to the inconsistencies in the literature on the effect of size and charge asymmetry on the ARPM this will serve as a useful tool to validate our results.

5.5   Conclusions

Throughout this chapter we have examined the UARPM through analytical, numerical and simulation methods. The BSCM results for the UARPM follow the results from Section 4.3 whereby the splitting theory results seem to bridge the gap displayed in Figures 4.3a and 4.3b where simulation results of critical points for a system phase change between solid and liquid occurs at lower temperatures and higher densities than the Debye-Hückel model. The splitting theory brings the results more in line with these simulations but they are only being used as a general guide as no specific simulations pertaining to the UARPM have been published. While the splitting theory gives a relatively good approximation, it is worth noting that there is a more advanced form of the splitting which would take into account a two component system where the interactions of different charges bound together contribute to the system. Employing this would allow more complicated systems to be studied and would hopefully yield accurate, stable results in comparison to the Debye-Hückel theory.

The GSCM results show that as l_B/α and $\rho\alpha^3$ increase, the system appears to undergo a phase change. The simulations show clusters forming in the system which are not predicted by the theoretical approaches. Figure 5.9 shows this occurring at $l_B/\alpha = 5$ and 10 where the internal energy of both systems equate after a certain point implying that both systems have found a similar equilibrium. Figure 5.11 shows a massive drop in the diffusion coefficient which indicates that the system is moving towards an equilibrium state. This transition is an intriguing part of the Symmetric and Asymmetric URPM and

warrants a separate discussion to investigate the validity and properties of this clustering phenomena. One of the critical components in this model is connecting it to the simulation work completed by others, as mentioned in the literature review there have been inconsistent results in the ARPM so far which would usually be used to frame the discussion of the UARPM. As mentioned above, an analogous system is the classical one component plasma which consists of point charges surrounded by a neutralising background charge. We postulate that the smeared charges of the UARPM may replicate this neutralising effect on a point charge meaning that the clustering observed in the UARPM at the high density-low temperature limit may be analogous to the freezing transition of the OCP. Clearly, an understanding of the OCP and it's behaviour, particularly around freezing, is required to frame our discussion on the UARPM clustering.

Chapter 6

One Component Plasma

6.1 Overview

Moving on from the UARPM, we note that there are apparent phase changes in the low temperature-high density limit. This behaviour is puzzling and therefore we must endeavour to link this to the behaviour of a well studied system such as the One Component Plasma. The OCP, while a system consisting of point charges surrounded by a uniform neutralising background, can be analogous to the asymmetric system of point charges surrounded by a smeared charge of size α. As discussed in Section 2.3.3, the OCP is defined by the Coulomb coupling parameter, Γ (Equation 2.1). This coupling parameter Γ is a function of ρl_B so, as the OCP does not consider the size of the particles α, increasing Γ decreases the temperature and increases the density of the system. Therefore it is a useful analogy to the UARPM low temperature-high density limit.

This chapter will detail the behaviour and theories associated with the OCP before linking results in the literature to the Gaussian UARPM. This section will expand this idea to consider various forms of asymmetry within the UARPM in comparison to the OCP and Asymmetric Restricted Primitive model (ARPM). Therefore we will attempt to forge

a link between the freezing point of the OCP at high Γ with the observed phase changes in the UARPM at high l_B/α and $\rho\alpha^3$.

Empirical Formulae

To build a picture of how the OCP behaves under different conditions, we first must investigate the mathematical grounding of this system and how we can relate this to the asymmetric ultrasoft model. As the OCP has been well studied in the literature, we are able to walk through the Empirical formulae which define the OCP. Therefore we can frame the discussion of linking the UARPM to this model. The Helmholtz Free energy of the OCP as developed by Hasegawa [13] is given by

$$
\frac{\beta F}{N} = \begin{cases} a\Gamma + 4\left(b\Gamma^{1/4} - c/\Gamma^{1/4}\right) + d\ln\Gamma - [a + 4(b-c) + 0.4363] & 1 < \Gamma < 180 \\ -0.6244\Gamma^{3/2} + 0.2126\Gamma^2 - 0.0245\Gamma^{5/2} & \Gamma < 1 \end{cases}
$$

based on the Monte Carlo experimental results of Slattery et al [14] where $a = -0.89774, b = 0.95043, c = 0.18956, d = -0.81487$.
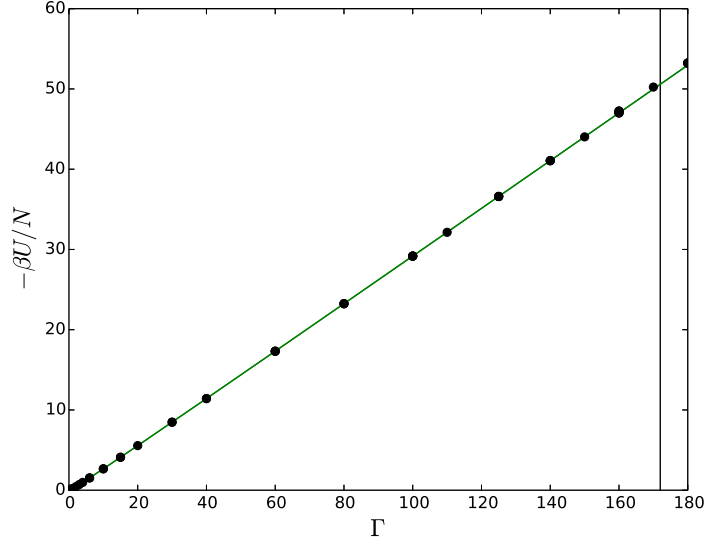
Figure 6.1: Empirical Internal energy from Hasegawa [13] (solid line) shown with the simulation results from Slattery et al [14] (black circles) as the coupling parameter Γ is increased. The vertical line shows the observed freezing point as $\Gamma > 172$ [15, 16]

From here, formulae for the internal energy and the excess pressure may be developed through $\partial \beta F / \partial \beta = U$

$$\frac{\beta U}{N} = a\Gamma + b\Gamma^{1/4} + c\Gamma^{-1/4} + d = \frac{\beta P_{ex}}{3} \qquad 1 < \Gamma < 180 \qquad (6.1)$$

where the excess pressure is given by βP_{ex}. This internal energy is shown in Figure 6.1 where the relationship between the internal energy and the freezing point of the OCP is shown [15, 16]. These formulae are developed from the MC simulations and are taken as the definitive solution to the OCP, however, as our interest lies in the theoretical approaches and how these have been used to approximate the OCP thus far.

Theoretical Approaches

The OCP has been extensively covered by integral equation theory [84, 131–133]. The hypernetted-chain (HNC) approximation has been used in regions of high coupling $(1 <$

$\Gamma < 50)$ to provide reasonably accurate results when compared to the simulation work [131, 134, 135]. Other examples of this include the mean spherical approximation [84, 133], the reference HNC approximation [136] and the hybrid HNC and Percus-Yevick closures [137]. These methods, while accurate, are intrinsically complex and computationally expensive which has led to the need for a more transparent physical representation of the system. From here, the simplicity of the Debye-Hückel theory becomes an attainable basis to develop a clear physical picture of the OCP. DH theory forces the ions to arrange themselves in such a way as to screen the long-range Coulomb interactions. Fixing a mobile ion at the origin, we may describe the OCP in the manner of Tamashiro et al [138]. Beginning with the Poisson equation.

$$\nabla^2 \psi(\mathbf{r}) = -\frac{4\pi}{\epsilon} q(\mathbf{r})$$

where a Boltzmann distribution is used to describe the arrangement of the mobile ions

$$q(\mathbf{r}) = q\rho_+ exp[-\beta q \psi(\mathbf{r})] = q\rho_-$$

where ρ_+ and ρ_- are the density of the mobile ions and the uniform neutralising background respectively. The correlation function can be expressed in terms of the potential of mean force as

$$g(r) = e^{-\beta q \psi(r)}$$

We now employ a linearisation of the exponential term of under the weak coupling limit giving

$$q(\mathbf{r}) = \frac{\epsilon \kappa_0^2}{4\pi} \psi(\mathbf{r})$$

where the inverse Debye screening is defined as $\kappa_0^2 = 4\pi l_B \rho_+$. Integrating the resulting Helmholtz equation $\nabla^2 \psi(\mathbf{r}) = \kappa_0^2 \psi(\mathbf{r})$ produced a Yukawa potential. However, the problem with this theory comes when examining the thermodynamic limit for Coulomb systems caused by normalising the Yukawa potential. This physical restriction that $q(\mathbf{r}) \geq -q\rho_-$ contradicts the resulting charge density distribution

$$q(\mathbf{r}) = -\frac{q\kappa_0^2}{4\pi r} e^{-\kappa_0 r}$$

as r decreases in the region around the fixed ion. Therefore the linearisation of the Boltzmann factor is not justified at short distances as the strong electrostatic repulsion results in a massive electrostatic energy. This problem requires a theory to differentiate between the long and short range interactions and clearly a solution to the non linear Poisson-Boltzmann equation.

Debye-Hückel Hole Theory

There have been several attempts at producing a more simple approach to the model. The most studied being the hole-corrected DH theory first postulated by Nordholm [56] where it was noted that there was a 'correlation hole' formed around the central ion. Nordholm noticed like-charged ions causing a strong repulsion which kept ions outside of the 'hole' due to the enormous amount of electrostatic energy which would be spent to penetrate it. There has been some trouble in creating an empirical parameter σ to describe the size of this correlation hole [56, 139]. It is defined within this approach as

$$\sigma = \frac{a[\omega(\Gamma) - 1]}{\sqrt{3\Gamma}}$$

where

$$\omega(\Gamma) = [1 + (3\Gamma)^{3/2}]^{1/3}$$

Inside the correlation hole, $r \leq \sigma$, the electrostatic potential satisfies the Poisson equation with a uniform background charge density so that $q_h = -q\rho$. Therefore

$$\psi_<(r) = \frac{q}{\epsilon r} + \frac{2\pi q\rho r^2}{3\epsilon} + \phi$$

while outside the hole, $r > \sigma$

$$\psi_>(r) = \frac{4\pi q\rho\sigma e^{-\kappa(r-\sigma)}}{\epsilon \kappa^2 r}$$

Now, setting $\psi_>(\sigma) = \psi_<(\sigma)$ to satisfy the condition of continuity of electrolytes we may determine the induced potential ϕ as

$$\phi = -\frac{1}{2\beta q}\left[(1 + (3\Gamma)^{3/2})^{2/3} - 1\right]$$

The resulting electrostatic free energy is then defined as

$$\frac{\beta F}{N} = \frac{1}{4}\left[1 - \omega^2 + \frac{2\pi}{3\sqrt{3}} + \ln\left(\frac{\omega^2 + \omega + 1}{3}\right) - \frac{2}{\sqrt{3}}\tan^{-1}\left(\frac{2\omega + 1}{\sqrt{3}}\right)\right]$$

This theory shows that at low temperatures the size of the correlation hole can be compared to the Wigner-Sitz radius as the ions are at their furthest from their neighbours. Then as the temperature increases so does the kinetic energy, σ decreases and the particles become less scattered. Then as the temperature increases the electrostatic repulsion becomes comparable to the thermal energy and as such, the size of the correlation hole becomes analogous to the Bjerrum length. Now, to compare to the empirical formulae we

can determine the internal energy of the DHH theory.

$$\begin{aligned}
\frac{\beta U}{N} &= \frac{\partial \beta F/N}{\partial \beta} \\
&= \frac{\partial \beta F/N}{\partial \omega} \frac{\partial \omega}{\partial \Gamma} \frac{\partial \Gamma}{\partial \beta} \\
&= \frac{3\Gamma\sqrt{\Gamma}}{8\beta(3\Gamma^{3/2}+1)^{2/3}} \left[-2\omega + \frac{2\omega+1}{\omega^2+\omega+1} - \frac{4}{9[(2\omega+1)^2+3]} \right]
\end{aligned}$$
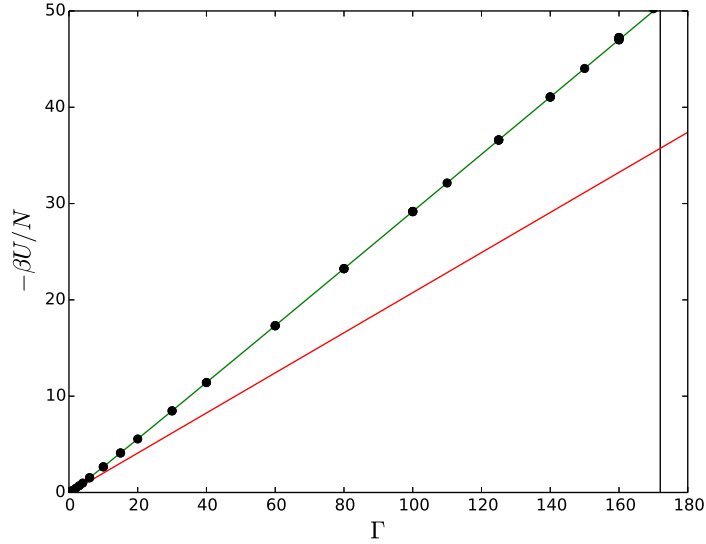
Figure 6.2: Internal energy for the DHH (red line) as the coupling parameter Γ is increased. The vertical line shows the observed freezing point as $\Gamma > 172$ [15, 16], the Empirical Internal energy from Hasegawa [13] (green line) is also shown with the simulation results from Slattery et al [14] (black circles) .

Therefore Figure 6.2 shows that the DHH theory does not approximate the OCP very well, particularly as the coupling parameter increases, this was noted by Levin [6] who states there is less than a 10% difference in between the DHH and MC simulations until $\Gamma \approx 80$ thereby capturing the prominent behaviour of the OCP. However, as this work is concerned with higher values of Γ and possibly the freezing transition which occurs at these values we must attempt to use other means to approximate the OCP.

Other Splitting Theories

As the issue with the DH theory is the short range interactions, the next logical step is to split the Coulomb interactions into a long and short range contribution where each part is defined by a different approximation scheme. There have been several works which use the splitting approach detailed in Section 2.3.1. These works find good agreement with simulation data but do not consider the high Γ limit/crystalline phases [66–69]. Another related theory is the Gaussian Field theory (GFT) which includes a high wave vector cut-off [140, 141]. If this cut off is chosen appropriately then there is excellent agreement between simulations.

6.2 UARPM application to the One Component Plasma

The crystalline phase of the OCP has been seen at $\Gamma \approx 180$. [14, 17, 87]. Therefore if we wish to discover the phase behaviour of the UARPM of Chapter 5, particularly the high density-low temperature limit then we consider the one component plasma (OCP) of point charges where the Debye-Hückel expression for the internal energy is

$$\frac{\beta U}{N} = -\frac{\kappa^3}{8\pi\rho_-} = -\frac{\sqrt{3}}{2}\Gamma^{3/2}$$

where $\kappa^2 = 4\pi\rho l_B = \frac{3}{l_B^2}\Gamma^3$, $\Gamma = (\frac{4\pi}{3}\rho_- l_B^3)^{1/3}$ and ρ_- is the density of the point charges. The 'splitting' model has been shown to work very well with the OCP [142] and forging a link between the UARPM and the OCP with give validation to the theoretical approach detailed above. Using Equation 6.1 for the empirical Internal energy and excess pressure we are able to adapt the simulation data from Figure 5.9 to show the behaviour of the asymmetric electrolyte in comparison to the OCP simulation results.
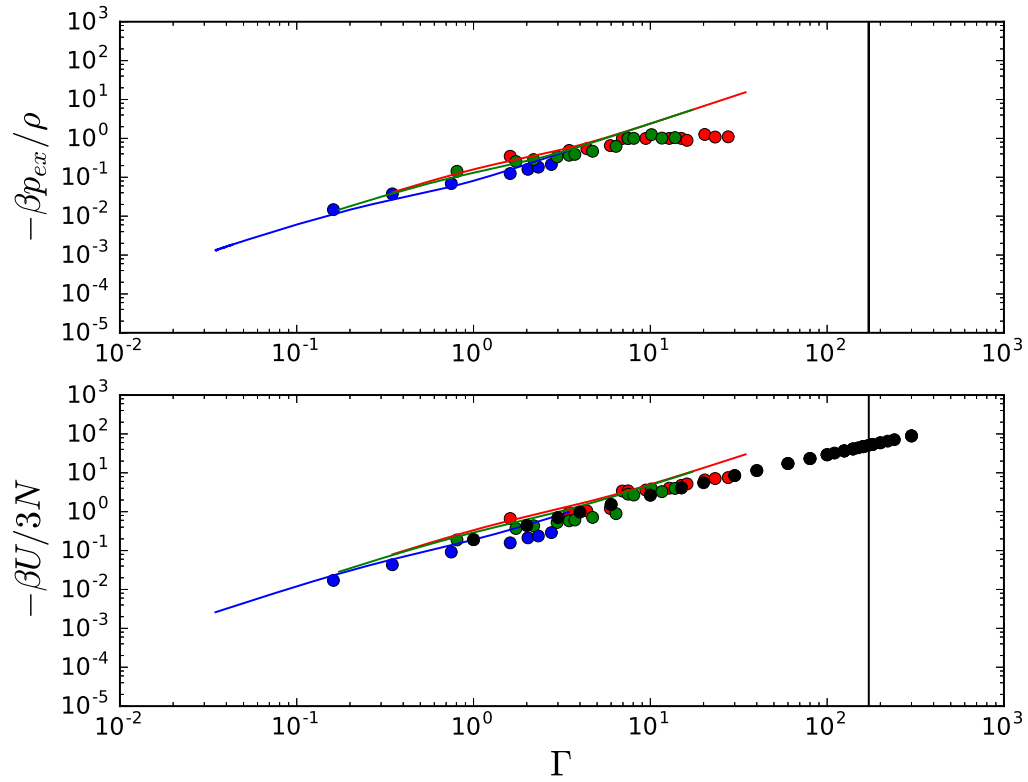
Figure 6.3: Internal energy and excess pressure of GROMACS simulations (Coloured Circles) compared to OCP simulation results (Black circles) from references [14, 17] as the coupling parameter Γ is increased. The coloured lines are the Debye-Huckel theory for asymmetric electrolytes where the blue, green and red lines correspond to $l_B/\alpha = 1, 5$ and 10 respectively. The vertical black line shows the observed freezing transition of the OCP
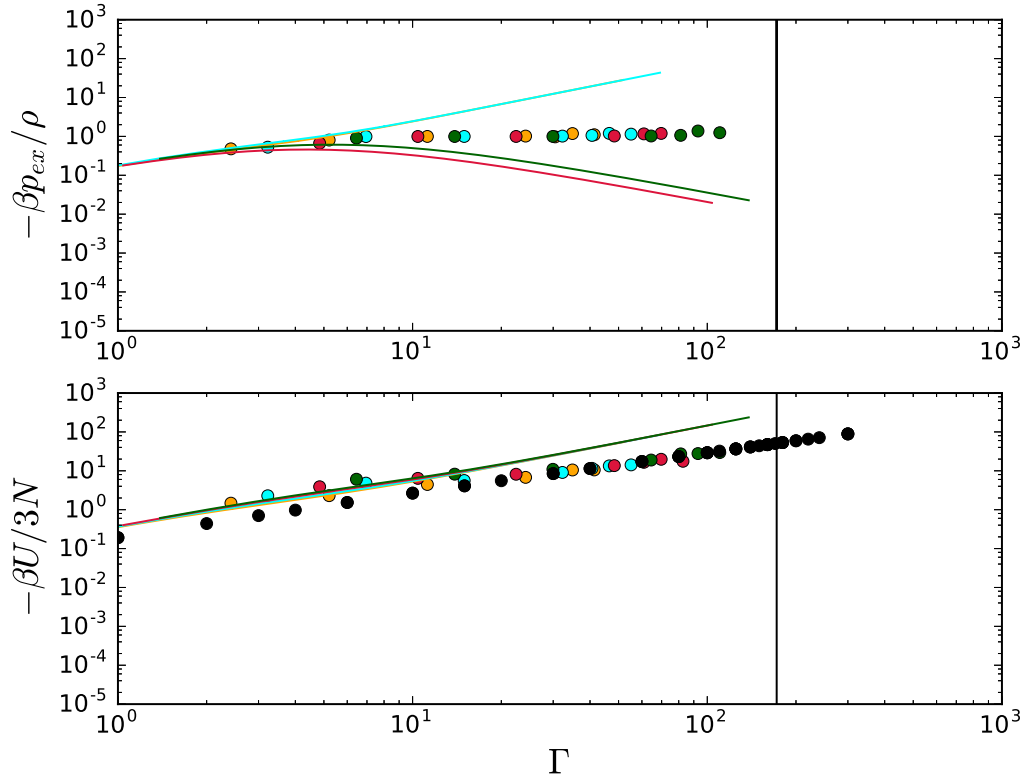
Figure 6.4: Internal energy and excess pressure of GROMACS simulations (Coloured Circles) compared to OCP simulation results (Black circles) from references [14, 17] as the coupling parameter Γ is increased. The coloured lines are the Debye-Huckel theory for asymmetric electrolytes where the yellow, cyan, red and green lines correspond to $l_B/\alpha = 15, 20, 30$ and 40 respectively. The vertical black line shows the observed freezing transition of the OCP

Figures 6.3 and 6.4 show the effect of different choices of l_B/α on the UARPM approaching the behaviour of the OCP. Here it is seen that as clusters form in the simulation data (approximately $\Gamma = 70$ for $l_B/\alpha \geq 5$) the internal energy value jumps to a more negative result before settling onto the theoretical OCP predictions. A possible reason for this could be that as the clusters form in the system then the overlapping charge clouds of the puffy ions become the neutralising background charge for the surrounding point charges. Also shown on Figures 6.3 and 6.4 is the observed freezing transition of the OCP. This takes place at higher values of Γ than the observed clustering. Provisionally, this is

an encouraging result as we would expect the UARPM to predict a more negative internal energy due to the added repulsive interaction between the puffy charges. In the OCP, the background is fixed therefore these interactions are negated. A possible extension to this would be the inclusion of the negative self energy of both the smeared and point charges which could possibly bring the GROMACS data more into line with the MC results from the literature. The radial distribution function for the OCP is defined by Levin [6] as

$$g(r) = e^{-\beta\phi(r)} \quad \text{where} \quad \phi(r) = \frac{qe^{-\kappa r}}{\epsilon r} \quad \text{and} \quad \kappa = 4\pi\rho l_B$$
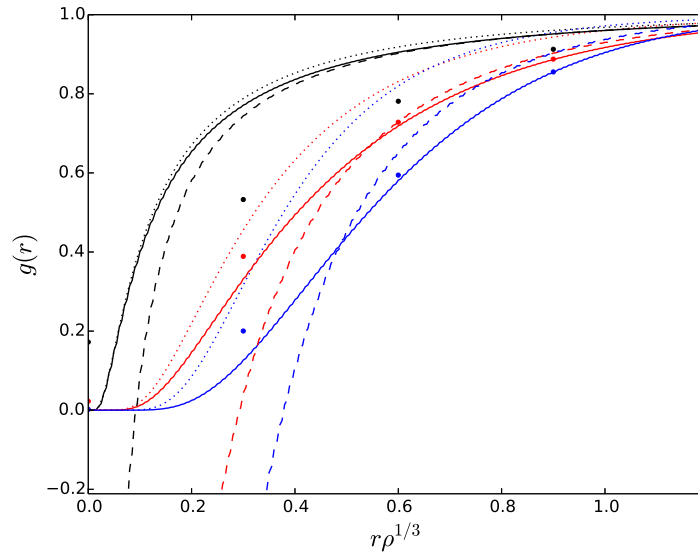
Figure 6.5: Radial distribution function for $\rho\alpha^3 = 1$. GROMACS (thick dots), HNC (solid line), MSA (dashed line) results are compared for point-point (–) charges. The black, red and blue represents $l_B/\alpha = 0.1, 0.5$ and 1 respectively. Also included is the rdf of the OCP[6] shown here as the dotted line

Figure 6.5 shows that as l_B/α increases toward unity, the radial distribution function of the UARPM tends towards that of the OCP as defined above. Increasing l_B/α further causes marked clustering at this density which skews the results somewhat. The DH theory over predicts the strength of the electrostatic interactions whilst the splitting theory has

been shown to work very well for the OCP in previous works [142], here it is seen that at high values of the plasma coupling parameter, the size of the correlation hole, σ is approximately proportional to the spacing between the counter-ions i.e. l_B/Γ. Heyes et al produced an interesting work on the OCP with possible links to this theory [143]. This could also be used to validate further study of the UARPM's link to the OCP.

6.3 Conclusion

This chapter has introduced the empirical MC forms of the OCP and a brief discussion of the theoretical and numerical approaches to studying the OCP. The main goal however, was to draw an analogy between the UARPM and the OCP, particularly in the low temperature-high density or high Γ limit. The simulation results of the GSCM UARPM offer a good indication that this is indeed possible as Figures 6.3 and 6.4 indicates. As Γ increases we see the internal energy of the UARPM simulations suffer a drop which brings it into line with the empirical internal energy of Equation 6.1. As stated above this comes at lower values of Γ than the OCP freezing transition, possibly due to the repulsive interaction between the puffy charges in the system which are not present in the OCP. Therefore the conclusion we are working towards is the UARPM undergoing a freezing transition similar to that of the OCP into a crystalline structure. To make such a link more concrete we must examine the behaviour of these clusters, how they behave under different conditions and whether they can be classed as a bcc crystal as with the frozen OCP.

Chapter 7

Clustering

7.1 Overview

The clustering phenomena seen in the smeared charge models asks more questions than it answers in this study of electrolytes. There are clearly defined reports of clustering in the RPM and OCP models [2] as discussed in Chapter 2. It is seen in Figure 2.2, that the RPM undergoes a phase change from vapour-liquid-crystalline solid. Depending on the temperature and density of the system, this solid can take the form of an fcc or bcc crystal as defined in Section 2.5. Therefore, we are aware of the potential impacts and applications which this clustering phenomena could lead to. Our comparison of the OCP and the Asymmetric electrolyte in Chapter 6 led us to the idea of the UARPM approaching the simulated OCP of Brush and Slattery et al [14, 17]. Given the known freezing transition of the OCP into a bcc Wigner crystal at low temperatures or high densities [15, 16, 86], the phase transitions observed in the UARPM as shown in Figures 6.3 and 6.4 as Γ increases towards the OCP freezing transition offer us an insight into the behaviour of the UARPM. Computationally, we observe this phase change or clustering behaviour through the aggregation of the ions in the MD simulation model, the details of which are described

in Section 4.4.1. This chapter will examine the simulation models of the URPM and UARPM. The observed clustering and pair behaviour shown under different temperatures and densities will be used to determine whether we are able to observe any crystalline behaviour in the ultrasoft model.

7.2 Asymmetric Electrolyes

As noted in Chapters 5 and 6 we observe interesting behaviour in the ultrasoft model. Clusters are seen to form under certain values of l_B/α and change number, density and shape as the simulation time goes on. This section will consider the UARPM focusing on a select l_B/α and $\rho\alpha^3$ pictorially and will follow cluster formation from start to finish. We will then perform cluster analysis on these systems to show how the clusters vary with the thermodynamic properties. The asymmetric electrolyte, as described in Chapters 5 and 6 is seen to approach the OCP and in particular the freezing transition of the OCP as described in Figures 6.3 and 6.4, as the value of l_B/α increases (i.e. a decrease in the system temperature) along with the value of the packing fraction $\rho\alpha^3$. Interestingly we see this transition happening at higher values of Γ than the OCP freezing point of Brush and Slattery[14, 17].
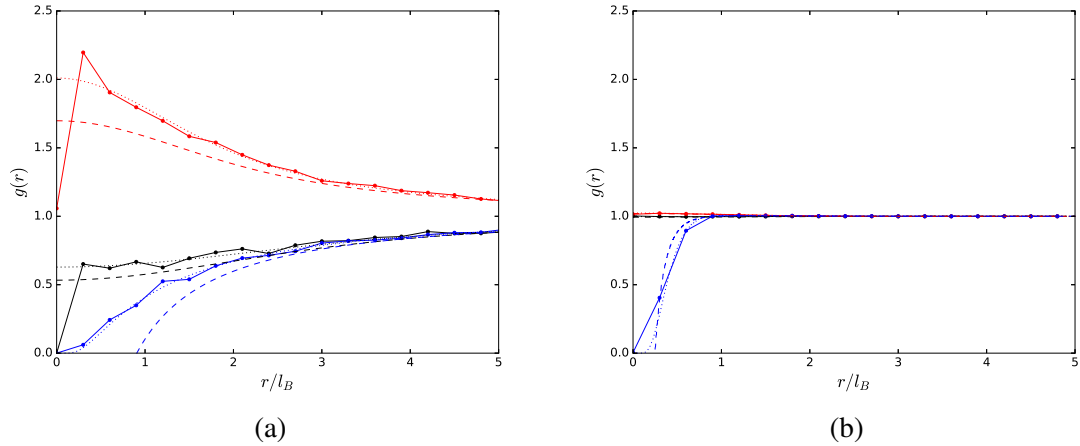
Figure 7.1: Radial distribution function for $l_B/\alpha = 1$ where the packing fraction $\rho\alpha^3 =$ (a) 0.001 and (b) 5.0. GROMACS (lines with dots representing the simulation points), HNC (dotted line) and MSA (dashed line) results are compared where point -point (–) are blue, puffy-point (+-) are black and puffy-puffy (++) are red.

For $l_B/\alpha < 4$ we see uniform behaviour in the ion-pairing/clustering as $\rho\alpha^3$ is changed. Figures 7.1a and 7.1b shows the pair behaviour at $l_B/\alpha = 1$ and $\rho\alpha^3 = 0.001$ and 5 respectively. At the lower density, Figure 7.1a, we see peaks in the rdf of the puffy-puffy (++) ions around $r/l_B \approx 0.3$ which may be due to statistical noise. This indicates that the smeared charges in the system are, on average, close to one another. As expected we see that the point-point (−−) interactions are very low as $r/l_B \to 0$ due to the strong repulsion of the point ions. The puffy-point (+−) display an interesting repulsion at low distances which is not as strong as the point-point (−−) interactions (as per the design of the ultrasoft system). All three results show reasonable agreement with the HNC and MSA approximations. Comparing this with the increase in the packing fraction in Figure 7.1b, we see similar behaviour in the point-point interactions although the repulsive drop happens at lower distances than Figure 7.1a, this is expected due to the increased density of the system where by at higher distances the probability of interacting with other ions becomes uniform. This uniformity is continued through as $r/l_B \to 0$ for the puffy-puffy and puffy-point interactions with a slightly higher probability for puffy-puffy interactions

likely due to penetrable nature of the spheres.

Comparing the two densities through the pair correlation functions is a very useful tool. However, it is also helpful to examine a snapshot configuration of the ions in the system.

<div align="center">(a)   (b)</div>
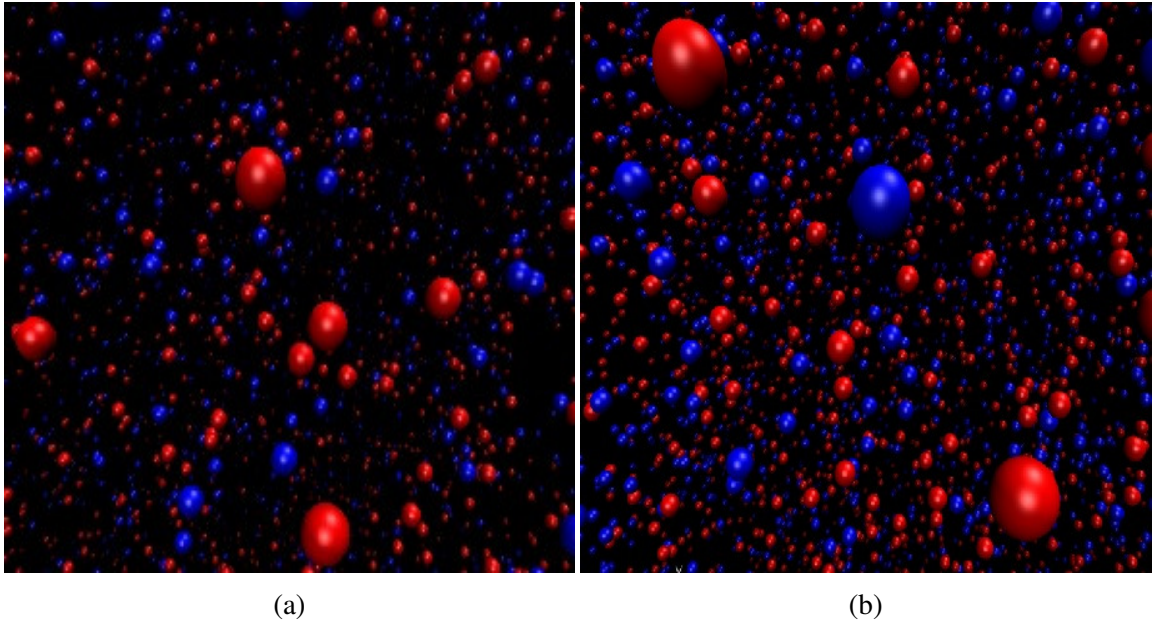
Figure 7.2: Image of an asymmetric cluster where the puffy and point charges are represented by the blue and turquoise spheres respectively. Here, $l_B/\alpha = 1$ and (a) $\rho\alpha^3 = 0.001$ and (b) $\rho\alpha^3 = 5.0$

Figures 7.2a and 7.2b show the visual representation of two states of the system in question. At $l_B/\alpha \leq 4$ it can be difficult to discern the differences pictorially, however they are a useful tool in contrasting the behaviour at lower temperatures. Figure 7.2b shows the ions in the system spread out uniformly which matches our analysis.

However, once the temperature is decreased (i.e. l_B/α is increased), we begin to see clustering behaviour in all values of $\rho\alpha^3$ examined. We will focus on $l_B/\alpha = 5$ for brevity. Figures 7.3a and 7.3b show the pair correlation functions for $l_B/\alpha = 5$ and $\rho\alpha^3 = 0.001$ and 1 respectively.
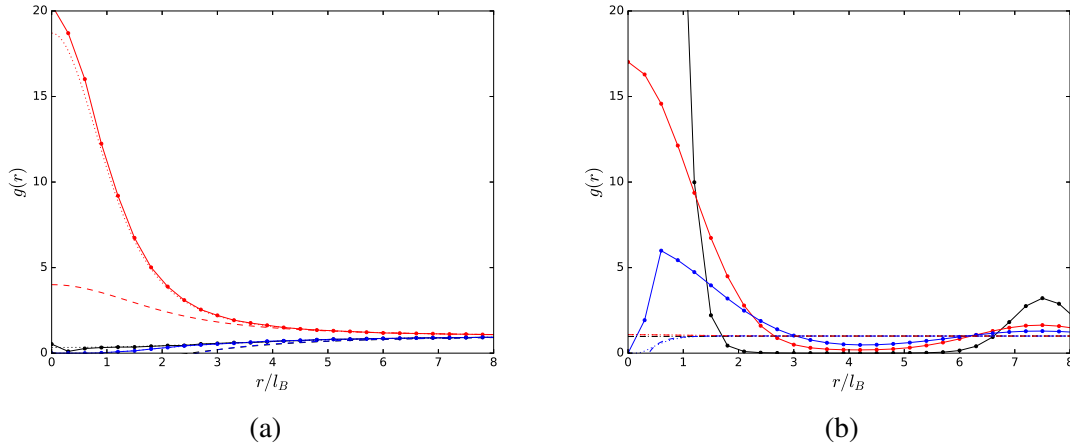
Figure 7.3: Radial distribution function for $l_B/\alpha = 5$ where the packing fraction $\rho\alpha^3 = $ (a) 0.001 and (b) 1.0. GROMACS (lines with dots representing the simulation points), HNC (dotted line) and MSA (dashed line) results are compared where point -point (–) are blue, puffy-point (+-) are black and puffy-puffy (++) are red.

These have a sharp contrast to the $l_B/\alpha = 1$ case studied previously. Figure 7.3a, shows a massive peak at $r/l_B = 0$ for the puffy-puffy correlations suggesting that at low distances the penetrable ions are tightly packed. This result has good agreement with the HNC approximation but the MSA predicts a much lower peak. The puffy-point and point-point behaviour shows repulsion at low distances comparable with the higher temperature result. This implies a cluster with the puffy ions located near each other in the centre and the point charges on the outside.

Figure 7.3b, shows the higher density system where similar behaviour is seen in the puffy-puffy interactions. What is striking here is the massive peak in the puffy-point inter-actions at low distances. The implication is that whilst the puffy ions stay tightly packed to one another, there are also high amounts of point charges embedded in the smeared charges at low distances. Moving further away from the origin we see a precipitous drop in the puffy point interactions until $r/l_B \approx 7.5$, where there is a smaller peak in the puffy-point interactions. This suggests separate structures of puffy-point interactions separated by certain distances within the system. Another interesting result here is the peak in the

point-point charge interactions at $r/l_B \approx 0.6$ followed by a sharp drop as $r/l_B \to 0$ meaning that the point charges surround one another upto a point but become very repulsive, as expected, at very short distances. It is worth noting here, that there is not good agreement here between the simulations and the HNC/MSA which has been noted by Coslovich et al [10] and Warren et al [11] for the symmetric URPM.

We now turn to the pictorial representation of the system to allow us to visualise the behaviour seen above where Figure 7.4a and 7.4b show us this clustering behaviour.

<div style="text-align:center">(a)   (b)</div>
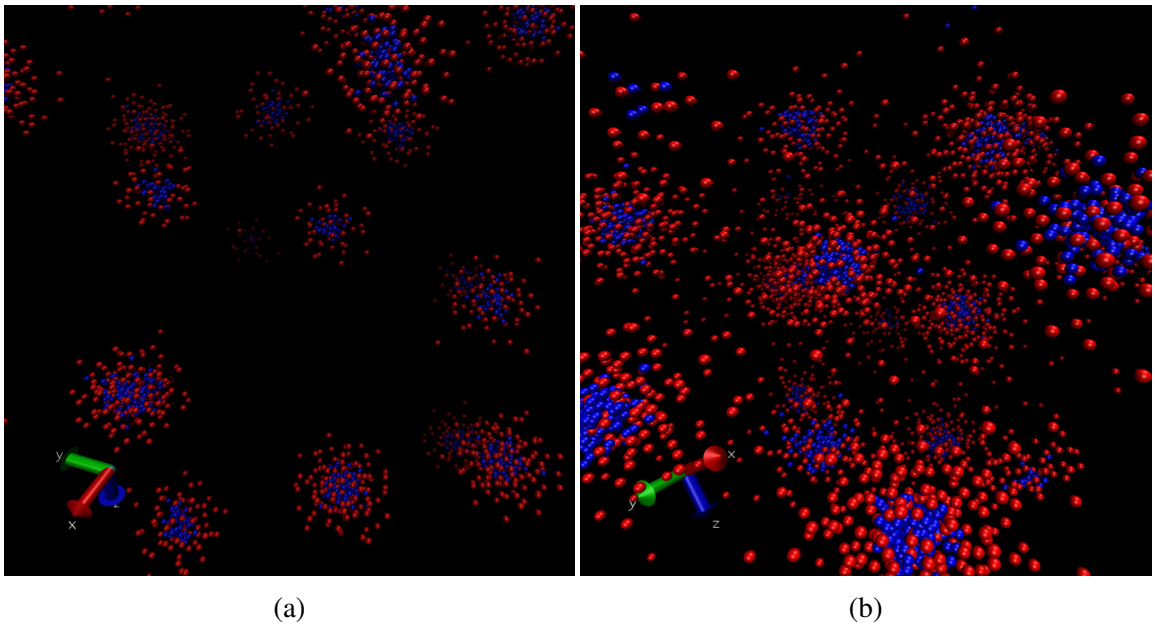
Figure 7.4: Image of an asymmetric cluster where the puffy and point charges are represented by the blue and turquoise spheres respectively. Here, $l_B/\alpha = 5$ and $\rho\alpha^3 = $ (a) 0.001 and (b) 1.0

Figure 7.4a shows several clusters formed in the system. These clusters consist of a core of like charged smeared charge ions surrounded by a *cloud* of point charges. Interestingly, there appears to be some point charges embedded in the smeared charge central cluster which are, in conjunction with the surrounding point charge cloud, keeping the smeared charges in place. The lower density of the system in comparison to Figure 7.4b likely leading to the large gaps in the system

Increasing the density of the system in Figure 7.4b leads to similar behaviour, albeit on a larger scale where the system consists of fewer clusters but the clusters are much larger and therefore closer together. This is indicative of the rdf behaviour discussed previously with the gap in between clusteres likely accounting for the spike in puffy-point interactions at $r/l_B \approx 7.5$ in Figure 7.3b. Therefore we have seen a pattern of cluster size increasing as $\rho\alpha^3$ increases thereby lowering the amount of clusters in the system.

(a)   (b)
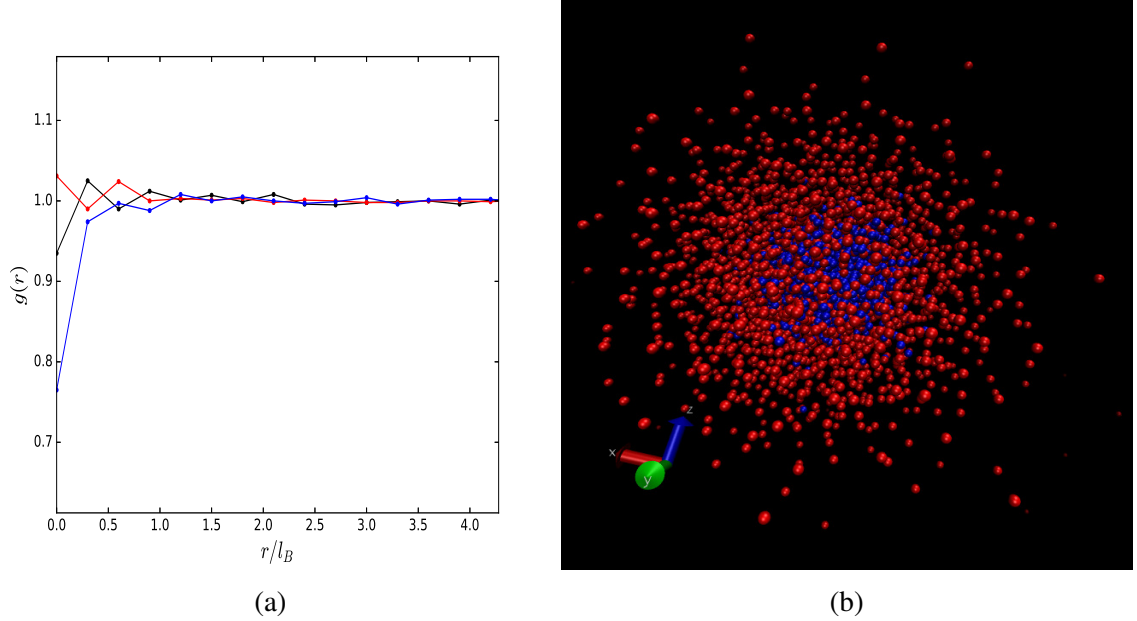
Figure 7.5: (a) Radial distribution function for $l_B/\alpha = 5$ where the packing fraction $\rho\alpha^3 = 5$. GROMACS (lines with dots representing the simulation points), HNC (dotted line) and MSA (dashed line) results are compared where point-point (–) are blue, puffy-point (+-) are black and puffy-puffy (++) are red. (b) Image of an asymmetric cluster where the puffy and point charges are represented by the blue and turquoise spheres respectively. Here, $l_B/\alpha = 5$ and $\rho\alpha^3 = 5$

Figures 7.5a and 7.5b shows the packing fraction increased to $\rho\alpha^3 = 5$. This has the effect (replicated in further simulations performed on systems with $l_B/\alpha \geq 4$) of reducing the amount of clusters in the system to a single cluster containing all of the ions in the system either as part of the smeared charge nucleus or the point charge cloud. The rdf of this system, shown in 7.5a shows almost uniform behaviour throughout the system

aside from the repulsive point-point charge behaviour. this is likely due to the density of the system being so high that the probabilities of being close to other ions in the system become close to unity.

Table 7.1 shows how different sizes of clusters are formed depending on l_B/α and $\rho\alpha^3$. The size we consider here is the total number of ions contained in a single cluster, positive and negative. It is seen clearly that increasing the packing fraction leads to a reduction in the maximum size and number of the clusters in the system. This is due to each ion in the system becoming closer to one another due to the increase of the packing fraction. Therefore, the space between clusters seen at lower values of $\rho\alpha^3$ where each cluster is unaffected by the other ions in the system is reduced as $\rho\alpha^3$ increases.

Table 7.1: Clustering details for several l_B/α and $\rho\alpha^3$ for the UARPM, the ratio described here represents the ratio of smeared charges to point charges in the system at the final timestep.

l_B/α	$\rho\alpha^3$	No of Clusters	Max Cluster Size (No of Ions)	Ratio $(+/-)$
4	1	20	8	1.666
4	2	2	4531	1.008
4	3	1	5160	1.007
4	5	1	5310	1.005
5	0.1	27	12	1.400
5	1	16	567	1.069
5	2	8	717	1.084
5	3	2	3971	1.006
5	5	1	5313	1.004
10	0.1	16	578	1.035
10	1	18	516	1.132
10	2	9	773	1.050
10	3	2	3868	1.001
10	5	2	4444	1.001
15	0.1	30	294	1.070
15	1	8	975	1.010
15	2	4	2693	1.002
15	3	2	2929	1.001
15	5	2	3104	1.001

Examining the ratio of smeared $(+)$ to point $(-)$ charges shows the clusters to be formed of almost identical number of smeared and point charges with there being slightly more smeared charges in each cluster. Therefore the core of smeared charges seen at the centre of each cluster is rendered amost charge neutral by the surrounding point charge cloud. A lower amount of ions in a cluster leads toa slightly higher ratio of smeared to point charges but this is likely due to the decrease in overall number of ions in the cluster rather than a trend in the system.

To examine this clustering phenomena further, we turn to the dynamic properties of the system discernible from the simulation model. Figures 7.6a and 7.6b show the velocity auto-correlation (VACF) functions for the puffy and point charges respectively for $\rho\alpha^3 = 0.001, 1$ and 5.

(a)   (b)
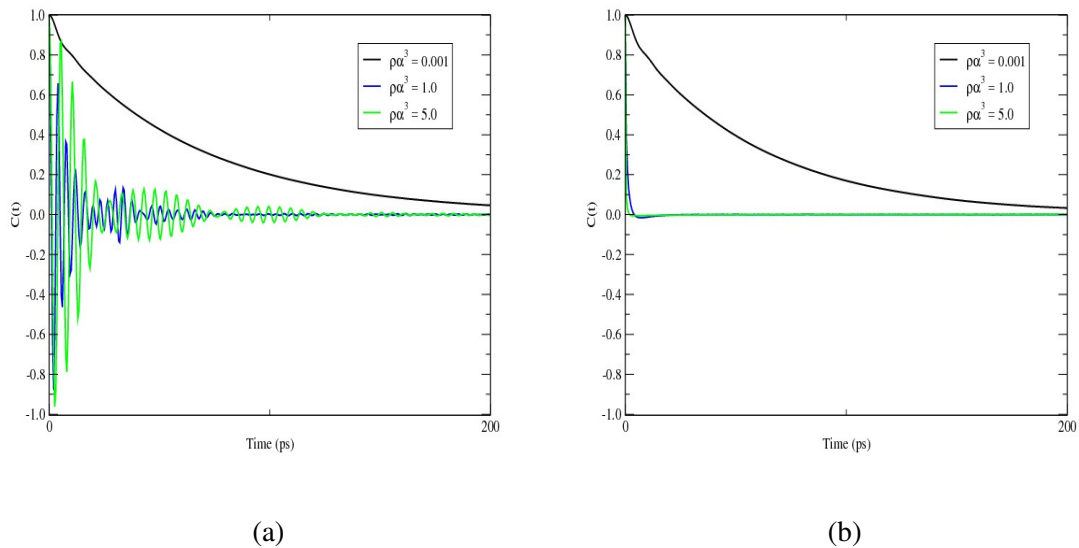
Figure 7.6: Simulation data for the auto-correlation function of (a) the smeared charges and (b) the point charges for $l_B/\alpha = 5$ as the packing fraction $\rho\alpha^3$ is increased.

For $\rho\alpha^3 = 0.001$ we see a steady decrease in velocity showing the the velocity decorrelating with time, which is the same as saying the atom 'forgets' its initial velocity. Therefore the forces acting upon the puffy and point charges in this scenario are small but not

negligible.

When $\rho\alpha^3 = 1$ or 5 we see very different behaviour to the low density model. In the increased density models we see stronger inter-ionic forces as the system ions are packed much closer together. In these circumstances the ions tend to seek out locations where there is a near balance between repulsive forces and attractive forces, since this is where the atoms are most energetically stable. As the system tends towards stability, the ions cannot escape easily from their positions. Their motion is therefore an oscillation; the ions vibrate backwards and forwards, reversing their velocity at the end of each oscillation. This is reflected in the oscillatory behaviour of Figure 7.6a and 7.6b. The oscillations will not be of equal magnitude however, but decay in time, due to the diffusive motion acting on the ions. So what we see is a function resembling a damped harmonic motion. The interesting idea here is that while the puffy ions are, by definition, penetrable at low distances (See Figure 5.1). The clustered structures of Figures 7.4a, 7.4b and 7.5b appear to how tightly packed smeared charges being kept in places by the surrounding 'hive' point charges meaning the original oscillatory nature of the VACF for puffy charges could be due to the smeared charges trying to escape these initial structures but being locked into place eventually by the neutralising surrounding force of the point ions.The VACF of the point charges in Figure 7.6b show an almost instant drop into an equilibrium which suggests that the 'hive' point ions are reasonably stable through out the initial struggles of the puffy ions to escape the cluster structure.

Figure 7.7 shows this diffusive motion through the self diffusion coefficient of the system for both puffy and point ions, we see that an increase in $\rho\alpha^3$ causes a large drop in the diffusion coefficient for both the puffy and point ions although the drop in the latter is less steep.

159
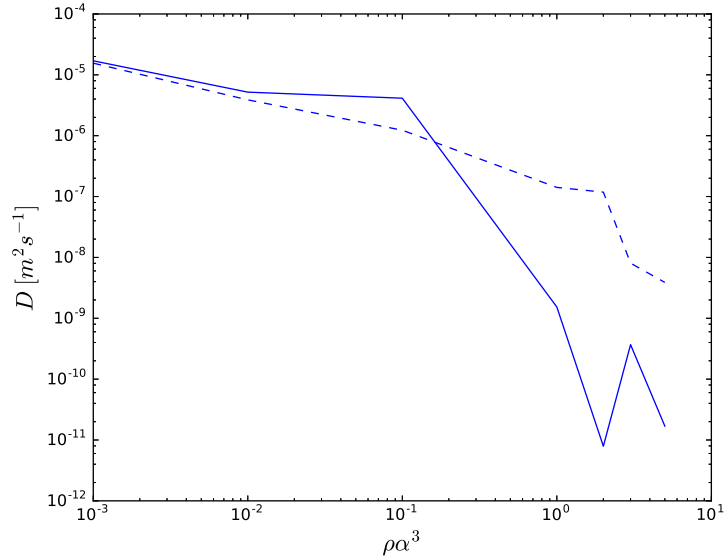
Figure 7.7: Diffusion coefficient of an asymmetric electrolyte where $l_B/\alpha = 5$. The solid line represents the smeared charges while the dashed line represents the points charges.

This drop coincides with the appearance of clusters within the system where the particles are not mixing in the steadily decreasing fashion seen at lower densities. The implication here is that the ions in the system become fixed in the cluster forms quickly and therefore do not mix with the other ions or clusters in the system as much as the lower densities. In a way this is counter-intuitive as one would imagine that as the packing fraction is increased, so would the mixing properties of the ions in the system.
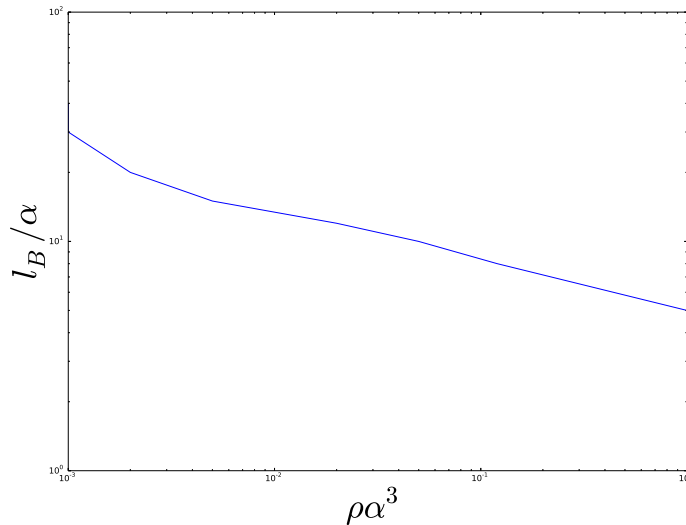
Figure 7.8: Transition of UARPM from pair to clustering behaviour.

Figure 7.8 shows the transition points for each of the models studies which display clustering. This shows that there is a clear correlation between $\rho\alpha^3$, l_B/α and cluster formation. An interesting future project could continue this to the colder temperatures seen in the URPM to establish a link to the unexplained like-charge attraction seen at high l_B/α and $\rho\alpha^3$.

7.3 Symmetric Electrolytes and Possible Artifacts

As noted in Chapter 4, the URPM shows interesting behaviours, particularly at the low temperature limit. Simulation results for higher temperatures i.e. $l_B/\alpha \leq 100$ show faint ion pairing at all densities examined. Figures 7.9a and 7.9b show the radial distribution functions for the URPM at $l_B/\alpha = 80$ and $\rho\alpha^3 = 0.001$ and 1.0 respectively. Here we observe that at $\rho\alpha^3 = 0.001$ there is a much less stable rdf, than seen at higher values of the packing fraction, particularly at low values of r/l_B. The rdf for like charges (++) and (−) are, as expected relatively similar to one another due to the make up of the symmetric

system. While the $\rho\alpha^3 = 0.001$ result is not as stable as $\rho\alpha^3 = 1.0$ we do see a peak of sorts in the like charged ions rdf at $r/l_B \approx 1.25$ indicating that there is a large amount of like charges ions close to one another at this distance. This peak also coincides with the (off graph) peak of the oppositely charged ions. indicating that the are large amounts of dipolar pairs but that there may also be trimers and upper order pairings in the system.
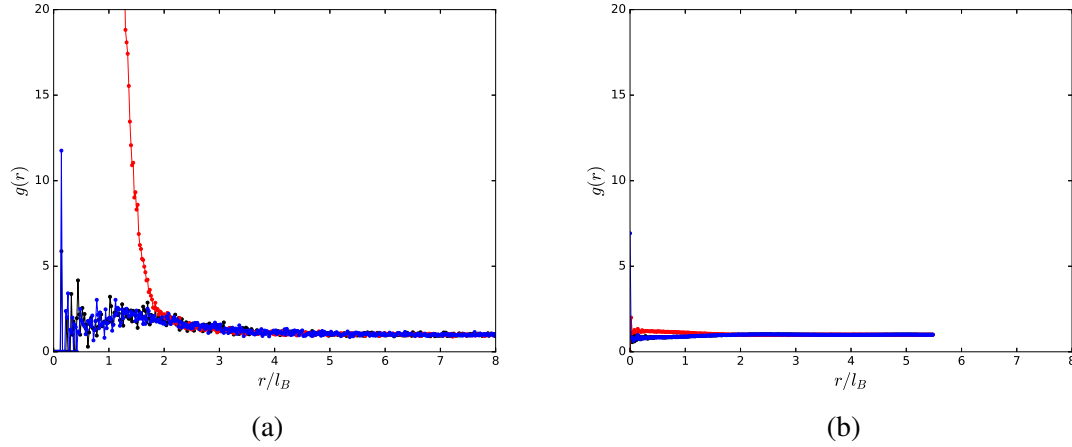
Figure 7.9: Radial distribution function for $l_B/\alpha = 80$ where the packing fraction $\rho\alpha^3 =$ (a) 0.001 and (b) 1.0. GROMACS (lines with dots representing the simulation points), HNC (dotted line) and MSA (dashed line) results are compared where (–) are blue, (+-) are black and (++) are red.

This behaviour is not replicated in Figure 7.9b which shows almost uniform behaviour for the (++), (–) , and (+-) interactions, implying that there is no clear pairing in the system. However when examining the images of the system in Figures 7.10a and 7.10b we see that when $\rho\alpha^3 = 1.0$ there are clear ion pairings. This disparity between the observed action of the ions and the pair is likely due to the tightly packed nature of the simulations as $\rho\alpha \to 1$
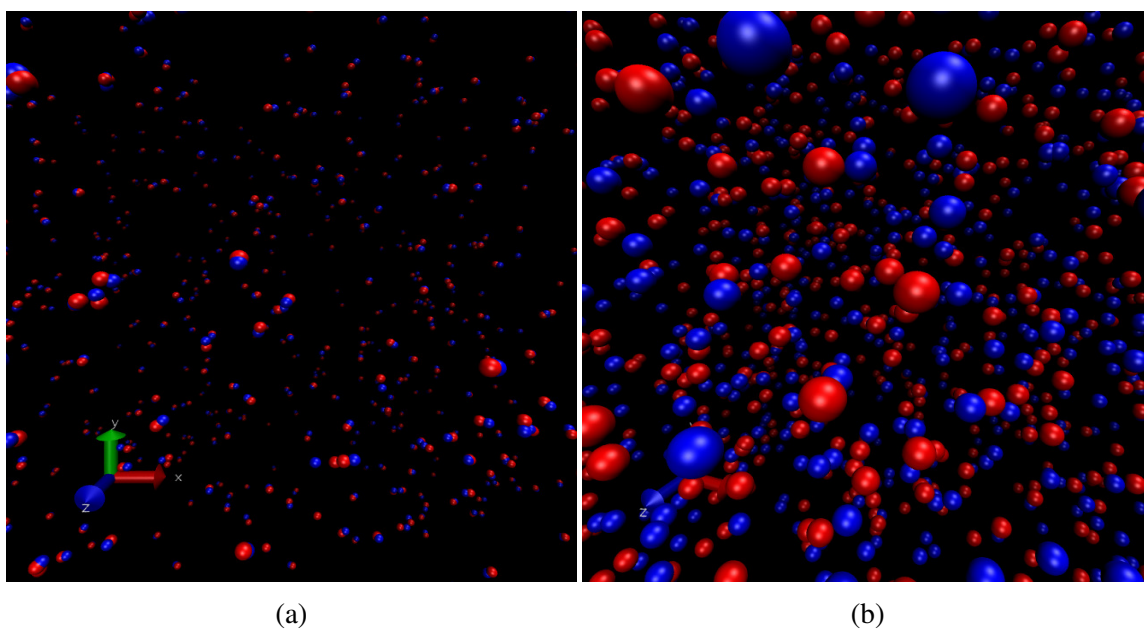
Figure 7.10: Image of an symmetric cluster where the puffy and point charges are represented by the blue and turquoise spheres respectively. Here, $l_B/\alpha = 80$ and $\rho\alpha^3 = $ (a) 0.001 and (b) 1.0

Taking much lower temperatures (i.e. $l_B/\alpha > 100$) we begin to see changes in how the system behaves as the packing fraction, $\rho\alpha^3$, is increased. A more extreme example of this is seen in Figures 7.11a and 7.11b where the system begins to show strange behaviour. The radial distribution function in Figure 7.11a shows spikes in the $(++)$ and $(--)$ interactions at $r/l_B \geq 3$ which indicate there is a structure taking form within the system. What makes this result more interesting is the different behaviour between the $(++)$ and $(--)$ ions, there are less spikes in the pair correlation function of the positive ions but these spikes are larger than the negative ions. THis behaviour may be down to the natural displacement of the ions in the system over time but it is strange to see such different behaviour in a symmetric electrolyte.

Investigating this behaviour further by looking at the image of the system in Figure 7.11b we see interesting behaviour by the symmetric ions in the system. Pairing still appears to be the predominant action of the ions but the distribution of ions around the

system is much less sparse than see in lower values of l_B/α and $\rho\alpha^3$. The ions seem to be, in general closer together but there is a large space in the centre of the simulation 'box' which is further indication that the system is forming some form of structure.

(a)   (b)
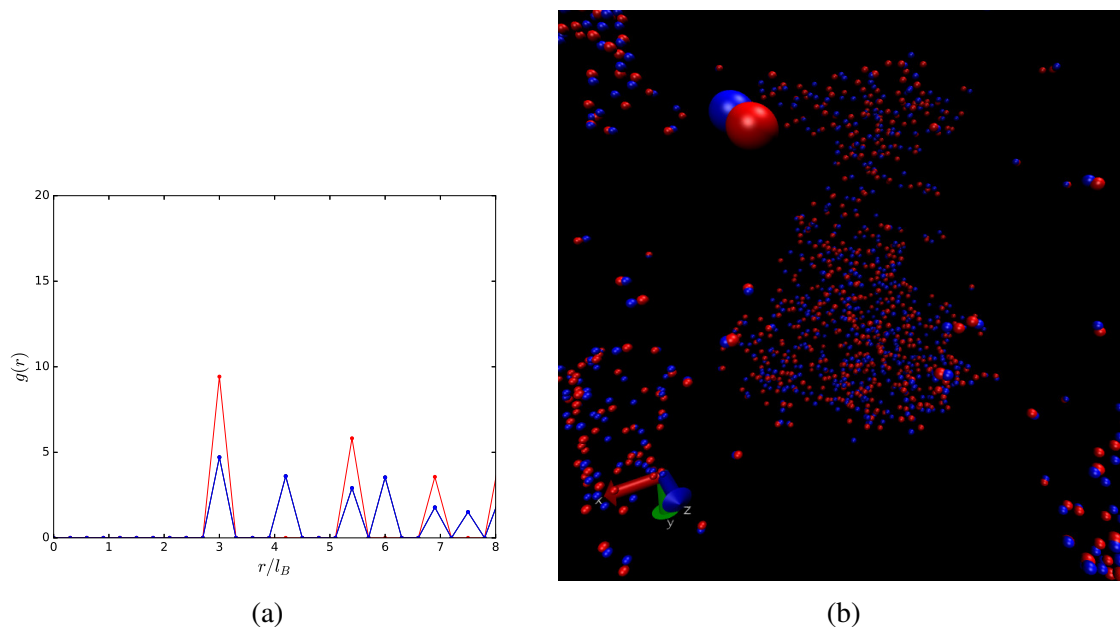
Figure 7.11: Simulation data for $l_B/\alpha = 500$ and $\rho\alpha^3 = 0.050$ showing (a) Radial distribution function with GROMACS (lines with dots representing the simulation points), HNC (dotted line) and MSA (dashed line) results are compared where ($-$) are blue, ($+$-) are black and ($++$) are red and (b) Image of an symmetric cluster where the puffy and point charges are represented by the blue and turquoise spheres respectively.

Increasing $\rho\alpha^3$ towards unity reveals puzzling behaviour in the system. Figure 7.12b shows the ions in the system clustering but interestingly the clusters here are purely like charged ions where the $+$ and $-$ ions are kept apart on the whole. Here the like charged ions in the system appear to be forming rods separated from the oppositely charged rods. Another interesting facet of this result is that these like-charged rods appear in a flat structure at on end of the box.

(a)   (b)
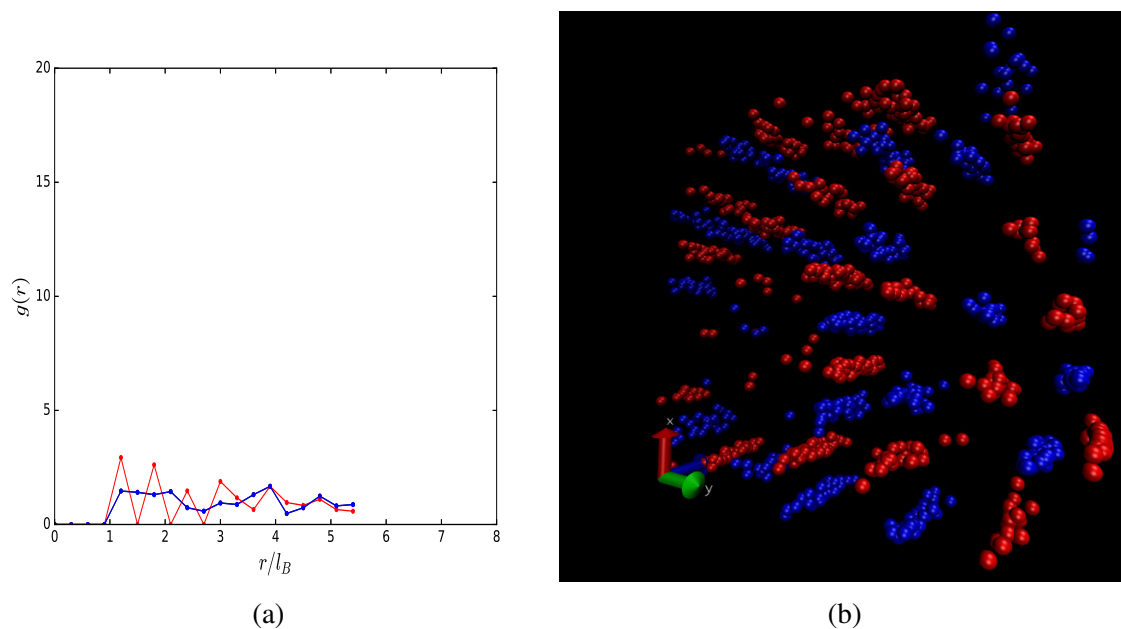
Figure 7.12: (a) Radial distribution function for $l_B/\alpha = 500$ where the packing fraction $\rho\alpha^3 = 1$. GROMACS (lines with dots representing the simulation points), HNC (dotted line) and MSA (dashed line) results are compared where the negatively charged smeared charges (−) are blue, positive charges (++) are red and the oppositely charged ions (+-) are black. (b) Image of an symmetric cluster where the positive and negative charges are represented by the blue and turquoise spheres respectively. Here, $l_B/\alpha = 500$ and $\rho\alpha^3 = 1$

The rdf of this system in Figure 7.12a doesn't elucidate matters completely as we see differing behaviour from the (++) ions to the (−) ions. This is seen at several values of $l_B/\alpha > 100$ but only when the packing fraction reaches unity. This is seen further in the dynamics of the system where Figure 7.13 shows the self diffusion coefficient of the URPM. At $l_B/\alpha = 80$ and 500 we see similar behaviour up until the packing fraction approaches unity. Before this point the diffusion coefficient appears to have hit a minima before rising but at the lower temperatures where the puzzling behaviour of Figure 7.12b leads to a precipitous drop in the diffusion coefficient.
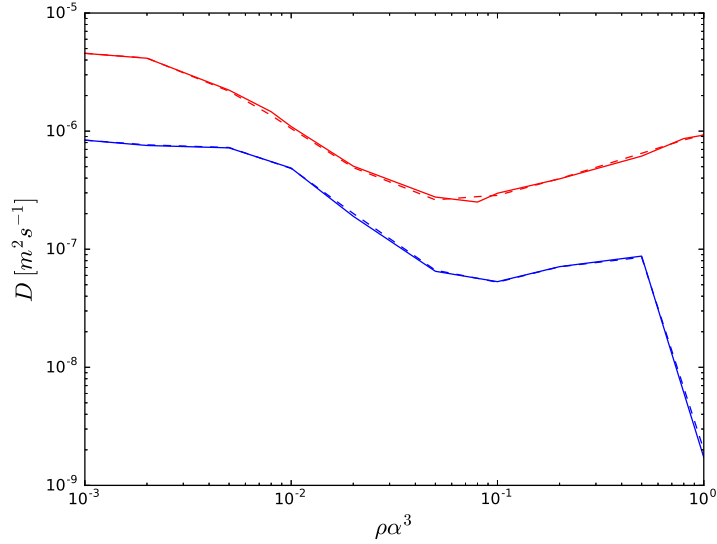
Figure 7.13: Diffusion coefficient of the URPM where the red and blue lines correspond to $l_B/\alpha = 80$ and 500 respectively

This unexplained behaviour, while interesting, leads to a discussion of possible artifacts in the system. Taking temperatures as low as $l_B/\alpha \geq 100$ can cause unexpected results. Using a different simulation approach, Warren et al [11] noted the presence of computational artifacts at $l_B/\alpha \geq 30$. Also, increasing $\rho\alpha^3 \to 1$ causes the ions to overlap with one another which may cause issues with the influence of each ion over one another. There is also the potential that increasing the box size of the simulations will lead to more stable results.

7.4 Conclusions

This chapter has presented analysis on the striking clustering behaviour seen in different fashions in the symmetric and asymmetric models. The radial distribution functions and limited dynamics analysis were used to explain the motion and relative distribution of the ions through the system.

The clustering in the asymmetric electrolyte takes on an interesting form as the temperature drops past $l_B/\alpha = 4$. We see marked clustering in this model where the puffy and point charges exhibit some interesting inter-ion behaviour. Figures 7.2a, 7.4b and 7.5b show clusters consisting of tightly packed puffy ions held together by a combination of a small number of point charges embedded in the aggregated puffy ions and a surrounding 'hive' made up of the remaining point charges. One possible explanation for presence of the singular point charges embedded in the puffy ions could be the tightly packed puffy charges performing a similar repulsive action on the point charges as the point 'hive' enacts on the aggregated puffy charges. Furthermore we see that as the packing fraction $\rho\alpha^3$ increases, so does the size of the clusters thereby reducing the amount of clusters in the system. This behaviour is shown most strikingly in Figure 7.5b where there remain one highly dense structure consisting of all of the ions in the system.

The HNC and MSA methods were used to benchmark the asymmetric rdf studies but as noted by Coslovich et al [10] and Warren et al [11] for the symmetric URPM, these methods fail to produce a satisfactory solution as l_B/α increases and as $\rho\alpha^3$ increases. Therefore the results shown, particularly the like charge clustering of Figure 7.12b are subject to a scrutiny beyond the current scope of this work. Therefore a prudent investigation of a further work would be the validity and stability of the clustering noted in this chapter.

Chapter 8

Conclusions and Future Work

In this final chapter, the main findings of this work are summarised and discussed before recommendations are made for further study.

8.1 Conclusions

Electrostatic interactions play a part in most biological processes and yet their behaviour in many situation is still unexplained. Electrolytes have been studied for over 100 years through theory, experiment and simulation work with vast arrays of different approaches being used throughout the years.

The objective of this thesis has been to study the behaviour of electrolytes with purely Coloumbic interactions present. We have studied the literature in Chapter 2, from the much studied Primitive Model and it's Restricted counterpart to the main focus of this thesis - the Ultrasoft Restricted Primitive Model. This model is a simplification of the Primitive and Restricted Primitive models. It is thought that removing the hard cores from the primitive models and replacing them with a penetrable smeared charge will reduce the complexity of the thermodynamic properties of the system by removing the hard core excluded volume calculations which represent much of the complexity of the hard core mod-

els. This was achieved by smearing the charge of each ion, firstly with a Bessel function which decreases towards 0. This charge smearing was chosen to reduce the complexity of the Helmholtz free energy calculations. This Bessel Smeared Charge Model is studied for both symmetric and asymmetric electrolytes where we were able to develop analytical forms for the free energies and in turn the various thermodynamic properties of the system such as the system pressure, (electro) chemical potential and internal energy. We then used Molecular Dynamics simulations to model the ultrasoft system under a Gaussian charge distribution. Changing the charge cloud should, in theory have no physical significance but it was noted by Warren et al [11] that differing approximations such as the RPA and HNC show different critical characteristics between the different charge clouds.

In the Symmetric Electrolyte studied in Chapter 4 we study the URPM which consists of equally sized and charged cations and anions with a smeared charge distribution. Using the analytical expressions for the thermodynamic properties of the system we were able to examine the behaviour of the Debye-Hückel and Splitting theory in depth. It was seen that the Bessel smeared charge model exhibits phase behaviour occurring at relatively high temperatures and low densities compared with the RPM, this is a consequence of the removal of the hard cores from the RPM. The Splitting model gives a result seemingly between the URPM and RPM models however it was not possible to optimise the Splitting parameter σ therefore an ansatz value of equating the value of the splitting parameter to the diameter of the ions, α. The Gaussian smeared charge simulations achieved good agreement under the MC simulations in the literature when studying the excess pressure and internal energy of the system. This allowed us to expand the theory in the low temperature-high density limit which is previously unstudied through this approach.

Chapter 5 adapts this simplified model to include the added complexity of an Asymmetric electrolyte. In this instance we considered a model of positive smeared charges in a continuum with an equal number of negatively charged point charges. This gives

a more realistic picture of electrolytes than the symmetric model. The Bessel smeared charge model was examined using the analytical formulae developed in Chapter 3 before moving on to the Gaussian smeared model. The pair correlation functions of this model shows good agreement with the integral equation theories MSA and HNC as defined in Chapter 3. Increasing l_B/α and $\rho\alpha^3$ in the molecular dynamics simulations shows signs of a structural change within the electrolyte, this clustering is qualified by the postulation of a link between the asymmetric smeared charge model and the classical one-component plasma (OCP) which forms Chapter 6. Here the OCP is introduced as a reasonable proxy for an asymmetric electrolyte where the neutralising background of the OCP is replaced with the smeared charges around the point charges of the UARPM. We see the UARPM approaching the simulation behaviour of the OCP as the value of the coupling parameter Γ is increased. The simulation data here also shows signs of the structural changes seen throughout the UARPM.

Chapter 7 studies the clustering in the symmetric and asymmetric models. For the UARPM, when $l_B/\alpha \geq 4$ we see clusters forming in the system with an unexpected structure. The positively charged smeared ions of the asymmetric system form a tightly packed nucleus in the centre of each cluster. This nucleus is surrounded by an almost equal number of negatively charged point charges which form a sort of hive around the positive centre. As $\rho\alpha^3$ increases we see a decrease in the number of clusters in the system with a corresponding increase in size of each cluster. This behaviour is novel to this project and represents a real opportunity for further study, particularly into lower temperatures and other forms of asymmetry.

8.2 Future Work

This work can lead to a number of future projects, in particular the clustering found in the asymmetric ultrasoft model. This work has focused on a specific form of asymmetry with a system consisting of smeared charge cations and point charge anions. However, there is a wealth of options in terms of charge and size asymmetry which can be considered, this could lead to a deeper understanding of the clustering phenomena described in Chapter 7. There has been a number of studies of size and charge asymmetric RPM models and an analogy between these and the ultrasoft model could lead to a deeper understanding on the effect of asymmetry on electrolytes, this is of particular reference as asymmetry is electrolytes is a more realistic physical model, albeit more complicated.

The forms of charge smearing chosen in Chapters 4 and 5 was applied to spherical ions, this model may be adapted to include ions with a positional dependency such as disks or rods with the charge smeared over the surface of each. This added complexity in the model is detailed in brief in Appendix B where this initial forms of the charged disks model are described.

Chapter 7 displayed complicated behaviour with particular attention being paid the Symmetric electrolyte which showed like-charged clusters forming at extremes of l_B/α and $\rho\alpha^3 = 1$. This behaviour and the accompanying pair correlation functions do not elucidate matters completely as to the implications and validity of this behaviour. A valid further study would be to investigate this like charged clustering in a rigorous fashion.

Nomenclature

α The size of the smeared charges of the URPM

α_k The size of the ion of species k

α_{RPM} The hard sphere diameter of ions within the Restricted Primitive Model

$\beta\mu_\eta$ The dimensionless system chemical potential

βP The dimensionless system pressure

β Reciprocal of the thermodynamic temperature

ϵ Dielectric constant of a dielectric continuum

$\frac{\beta F(\rho)}{V}$ The dimensionless Helmholtz Free Energy

Γ The Coulomb coupling parameter

κ The Debye screening length

$\langle \cdot \rangle$ thermal average

$\mathcal{P}(\mathbf{p})$ The splitting parameter which tunes out short wavelengths

Ω The orientation of an ion located at the origin

ρ_η The density of a particle of type η

ρ_c Critical density

$\Sigma(\mathbf{r})$ a fixed background charge

a The Wigner-Seitz radius which determines the mean spacing between the ions

$i\hat{\psi}$ Instantaneous electric potential

k_B Boltzmann's constant

l_B Bjerrum length

N The total number of ions in an electrolyte solution

q The charge of a cation or anion

$Q(r)$ The charge density of the URPM charge cloud

r The distance between ions

T The temperature of a system of ions

T_c Critical temperature

$u_{ij}(r)$ The pair distribution function of two ions i and j, separated by distance r

V The volume of an electrolyte solution

Bibliography

[1] AP Hynninen, ME Leunissen, A van Blaaderen, and M Dijkstra. Cuau structure in the restricted primitive model and oppositely charged colloids. *Phys. Rev. Lett.*, 96(1):018303, 2006.

[2] Michael E. Fisher and Yan Levin. Criticality in ionic fluids: Debye-hückel theory, bjerrum and beyond. *Physical Review Letters*, 1993.

[3] AK Sabir, LB Bhuiyan, and CW Outhwaite. Influence of ion size and valence on classical ionic criticality. *Mol. Phys.*, 93, 3:405–409, 1998.

[4] R. R. Netz and H. Orland. Field theory for charged fluids and colloids. *Europhys. Lett.*, 45:726, 1999.

[5] Yan Levin and Michael E. Fisher. Criticality in the hard-sphere ionic fluid. *Physica A*, 164(220), 1995.

[6] Yan Levin. Electrostatic correlations: from plasma to biology. *Reports on Progress in Physics*, 65:1577–1632, 2002.

[7] D. Coslovich, J.-P. Hansen, and G. Kahl. Clustering, conductor-insulator transition and phase separation of an ultrasoft model of electrolytes. *Soft Matter*, 7:1690, 2011.

[8] D.M. Heyes and G. Rickayzen. Clustering of continuous distributions of charge. *Mol. Phys.*, 112:13981404, 2014.

[9] J.-M. Caillol and D. Levesque. Liquid-vapor transition and critical behavior of the ultrasoft restricted primitive model of polyelectrolytes : A monte carlo study. *J. Chem. Phys*, 140, 21:214505, 2014.

[10] D. Coslovich, J.-P. Hansen, and G. Kahl. Ultrasoft primitive model of polyionic solutions: Structure, aggregation, and dynamics. *J. Chem. Phys*, 134:244514, 2011.

[11] Patrick B. Warren and Andrew J. Masters. Phase behaviour and the random phase approximation for ultrasoft restricted primitive models. *J. Chem. Phys*, 138, 2013.

[12] P. Warren, A. Vlasov, L. Anton, and A. J. Masters. Screening properties of gaussian electrolyte models, with application to dissipative particle dynamics. *J. Chem. Phys*, 138:29407, 2013.

[13] M Hasegawa. Freezing of the classical one-component plasma: analyses of the non-perturbative density-functional theories. *J. Phys. Condensed Matter*, 4:5493, 1992.

[14] W. L. Slattery, G. D. Doolen, and H. E. DeWitt. *Phys. Rev. A*, 26:2255, 1982.

[15] S. M. Stishov. Does the phase transition exist in the one-component plasma model? *Journal of Experimental and Theoretical Physics Letters*, 67(1):90–94, January 1998.

[16] C. N. Likos and N. W. Ashcroft. Self-consistent theory of freezing of the classical one-component plasma. *Physical Review Letters*, 69(316), 1992.

[17] Sg Brush, Hl Sahlin, and E Teller. Monte carlo study of a 1-component plasma .i. *J. Chem. Phys.*, 45:2102, 1966.

[18] H Boroudjerdi, YW Kim, A Naji, RR Netz, X Schlagberger, and A Serr. Statics and dynamics of strongly charged soft matter. *Physics Reports- Review section of Physics Letters*, 416, Issues 3-4:129–199, 2005.

[19] T.D Yager, C.T. McMurray, and K.E. VanHolde. Salt-induced release of dna from nucleosome core particles. *Biochemistry*, 28(5):2271–2281, 1989.

[20] Kyle J. M. Bishop, Christopher E. Wilmer, Siowling Soh, and Bartosz A. Grzybowski. Nanoscale forces and their uses in self-assembly. *Small*, 5(14):1600–1630, 2009.

[21] R. A. Curtis and L. Lue. Electrolytes at spherical dielectric interfaces. *J. Chem. Phys.*, 123:174702, 2005.

[22] P. Debye and F. Hückel. The theory of electrolytes. i. lowering of freezing point and related phenomena. *Physik. Z.*, 24, 1923.

[23] J.H. van't Hoff. Theory of dilute solutions. *Chem. Ber.*, 10:669, 1877.

[24] Svante Arrhenius. Ionization theory. *Z. Phys. Chem.*, 1:631, 1887.

[25] G. Gouy. Sur la constitution de la charge electique a la surface d'un electrolyte. *J. Phys. Radium 9*, 9:468–475, 1910.

[26] D. L. Chapman. A contribution to the theory of electroencapillarity. *Philos*, 25:475–481, 1913.

[27] W. G. McMillan and J. E. Mayer. The statistical thermodynamics of multicomponent systems. *J. Chem. Phys*, 13(276), 1946.

[28] N. Bjerrum. Kgl. dan. vidensk. selsk. *Mat-fys. Medd*, 7:1, 1926.

[29] M.R Wright. *An Introduction to Aqueous Electrolyte Solutions*. Wiley., 2007.

[30] Jean-Pierre Simonin, Olivier Bernard, and Lesser Blum. Real ionic solutions in the mean spherical approximation. 3. osmotic and activity coefficients for associating electrolytes in the primitive model. *J. Phys. Chem. B*, 102(22):4411–4417, 1998.

[31] Zareen Abbas, Elisabet Ahlberg, and Sture Nordholm. Monte carlo simulations of salt solutions: Exploring the validity of primitive models. *J. Chem. Phys B*, 113(17):5905–5916, 2009.

[32] B. Hribar Lee and V. Vlachy. Thermodynamic properties of charge asymmetric mixed electrolytes in the primitive model. *J. Mol. Liq*, 118(163-169), 2005.

[33] P.N. Vorontsov-Velyaminov, A.M. Elyashevich, and L.A. Morgenshtern et al. Investigation of phase transitions in argon and coulomb gas by monte-carlo method using an isothermically isobaric ensemble. *High Temperature*, 8(261), 1970.

[34] P.N. Vorontsov-Velyaminov and V.P. Chasovskikh. Critical-point in an ionic system from results of a mathematical experiment - comparison with salt melts. *High Temperature*, 13(6):1071–1076, 1975.

[35] J.-J. Weis and D. Levesque. Solid phase diagram of a classical electronic bilayer. *Phys. Rev. B*, 63:045308, 2001.

[36] Yu. V. Kalyuzhnyi, M. F. Holovko, and V. Vlachy. Highly asymmetric electrolytes in the associative mean-spherical approximation. *J. Stat. Phys*, page 100:243, 1999.

[37] G. Patey. The interaction of two spherical colloidal particles in electrolyte solution. an application of the hypernettedchain approximation. *J Chem. Phys.*, 72(5763), 1980.

[38] S Kjellander, R. & Marcelja. Correlation and image charge effects in electric double-layers. *Chemical Physics Letters*, 112:49–53, 1984.

177

[39] R. Kjellander and S. Marcelja. Double-layer interaction in teh primitive model and the corresponding poisson-boltzmann description. *J Chem. Phys.*, 90(7):1230–1232, 1986.

[40] G Stell, KC Wu, and B Larsen. Critical-point in a fluid of charged hard spheres. *Phys. Rev. Lett.*, 37(21):1369–1372, 1976.

[41] AZ Panagiotopoulos. Molecular simulation of phase-equilibria - simple, ionic and polymeric fluids. *Fluid Phase Equil.*, 92:313, 1994.

[42] G. Orkoulas and A.Z. Panagiotopoulos. Free-energy and phase-equilibria for the restricted primitive model of ionic fluids from monte-carlo simulations. *J Chem. Phys.*, 101(2):1452–1459, 1994.

[43] A.Z. Panagiotopoulos. Monte carlo methods for phase equilibria of fluids. *Condensed Matter*, 12(R25), 2000.

[44] A.Z. Panagiotopoulos. Critical parameters of the restricted primitive model. *J. Chem. Phys*, 2002.

[45] QL Yan and JJ de Pablo. Hyper-parallel tempering monte carlo: Application to the lennard-jones fluid and the restricted primitive model. *J Chem. Phys.*, 111(21):9509–9516, 1999.

[46] G Orkoulas and A.Z. Panagiotopoulos. Phase behavior of the restricted primitive model and square-well fluids from monte carlo simulations in the grand canonical ensemble. *J Chem. Phys.*, 110(3):1581–1590, 1999.

[47] Y Guissani and B Guillot. Coexisting phases and criticality in nacl by computer-simulation. *J Chem. Phys.*, 101(1):490–509, 1994.

[48] YC Kim and M. Fisher. Discretization dependence of criticality in model fluids: A hard-core electrolyte. *Phys. Rev. Lett.*, 92(18):185703, 2004.

[49] A. Bruce and N. Wilding. Scalingfields and universality of the liquid-gas critical-point. 68(2):193–196, 1992.

[50] NB Wilding and AD Bruce. Density-fluctuations and field mixing in the critical fluid. *J. Phys. Condensed Matter*, 4(12):3087–3108, 1992.

[51] J. Caillol. A monte-carlo study of the liquid-vapor coexistsence of charged hard spheres. *J Chem. Phys.*, 100(3):2161–2169, 1994.

[52] JM Caillol, D Levesque, and JJ Weis. Critical behavior of the restricted primitive model revisited. *J. Chem. Phys*, 116(24):10794–10800, 2002.

[53] B Smit, K Esselink, and D Frenkel. Solid-solid and liquid-solid phase equilibria for the restricted primitive model. *Molecular Physics*, 87(1):159–166, 1996.

[54] C Vega, F Bresme, and JLF Abascal. Fluid-solid equilibrium of a charged hard-sphere model. *Phys. Rev. E.*, 54(3):2746–2760, 1996.

[55] F Bresme, C Vega, and JLF Abascal. Order-disorder transition in the solid phase of a charged hard sphere model. *Phys. Rev. Lett.*, 85(15):3217–3220, 2000.

[56] Sture Nordholm. Simple analysis of the thermodynamic properties of the one-component plasma. *Chem. Phys. Lett.*, 105(3):302–7, 1984.

[57] R. D. Coalson and A. Duncan. Systematic ionic screening theory of macroions. *J. Chem. Phys.*, 97(8):5653–5661, OCT 15 1992.

[58] R. R. Netz and H. Orland. Beyond Poisson-Boltzmann: Fluctuation effects and correlation functions. *Eur. Phys. J. E*, 1(2-3):203–214, 2000.

[59] R. P. Feynmann. *Statistical Mechanics: A Set of Lectures*. Addison-Wesley, Redwood CA, 1972.

[60] R. R. Netz and H. Orland. Variational charge renormalization in charged systems. *Eur. Phys. J.*, 11:310–311, 2003.

[61] M. M. Hatlo, R. A. Curtis, and L. Lue. Electrostatic depletion forces between planar surfaces. *J. Chem. Phys.*, 128(16):164717, 2008.

[62] B. I. Shklovskii. Screening of a macroion by multivalent ions: Correlation-induced inversion of charge. *Phys. Rev. E*, 60(5):5802–5811, Nov 1999.

[63] A. G. Moreira and R. R. Netz. Binding of similarly charged plates with counterions only. *Phys. Rev. Lett.*, 87(7):078301, 2001.

[64] A Naji, M Kanduc, J Forsman, and R Podgornick. Perspective: Coulomb fluids-weak coupling, strong coupling, in between and beyond. *J. Chem. Phys*, 139(15), 2013.

[65] Ladislav Samaj and Emmanuel Trizac. Counterions at highly charged interfaces: From one plate to like-charge attraction. *Phys. Rev. Lett.*, 106:078301, Feb 2011.

[66] Y-G Chen, C. Kaur, and J.Weeks. Connecting systems with short and long ranged interactions. *J. Phys. review*, 108:19874, 2004.

[67] Yng-Gwei Chen and John D. Weeks. Local molecular field theory for effective attractions between like charged objects in systems with strong coulomb interactions. *Proc. Nat. Acad. Sci. (USA)*, 103:7560–7565, 2006.

[68] Christian D. Santangelo. Computing counterion densitites at intermediate coupling. *Phys. Rev. E*, 73:041512, 2006.

[69] Marius M. Hatlo and Leo Lue. A field theory for ions near charged surfaces valid from weak to strong couplings. *Soft Matter*, 5:125–133, 2009.

[70] M. M. Hatlo and L. Lue. Electrostatic interactions of charged bodies from the weak- to the strong-coupling regime. *EPL (Europhysics Letters)*, 89(2):25002, 2010.

[71] Leo Lue and Per Linse. Macroion solutions in the cell model studied by field theory and Monte Carlo simulations. *J. Chem. Phys.*, 135(22):224508, 2011.

[72] L. Lue and P. Linse. Ions confined in spherical dielectric cavities modeled by a splitting field-theory. *J Chem. Phys.*, 142(144902), 2015.

[73] PJ. Camp and GN. Patey. Ion association and condensation in primitive models of electrolyte solutions. *J. C*, 111(19):9000–9008, 1999.

[74] AZ Panagiotopoulos and ME Fisher. Phase transitions in $2:1$ and $3:1$ hard-core model electrolytes. *Phys. Rev. Lett.*, 88, 4(045701), 2002.

[75] E. Gonzalez-Tovar. Critical parameters of asymmetric primitive model electrolytes in the mean spherical approximation. *Mol*, 97(11):1203–1206, 1999.

[76] Christopher W. Outhwaite, Miguel Molero, and Lutful B. Bhuiyan. Primitive model electrolytes in the modified poisson-boltzmann theory. *J. Chem. Soc., Faraday Trans. 2*, 89:1315–1320, 1993.

[77] M.N. Tamashiro, Yan Levin, and Marcia C. Barbosa. Debye-hückel-bjerrum theory for charged colloids. *Physica A*, 258:341–351, 1998.

[78] JM Romero-Enrique, G Orkoulas, AZ Panagiotopoulos, and ME Fisher. Coexistence and criticality in size-asymmetric hard-core electrolytes. *Physical Review Letters*, 85, 21:4558–4561, 2000.

[79] Robert Penfold, Bo Jonsson, and Margaret Robins. A simple analysis of thermodynamic properties for classical plasmas: Ii. validation. *Journal of Statistical Mechanics*, 2005.

[80] Young C. Kim, Michael E. Fisher, and Athanassios Z. Panagiotopoulos. Universality of ionic criticality: Size- and charge-asymmetric electrolytes. *Physical Review Letters*, 95, 2005.

[81] Jean-Nol Aqua, Shubho Banerjee, and Michael E. Fisher. Criticality in charge-asymmetric hard-sphere ionic fluids. *Phys. Rev. E*, 72:041501, 2005.

[82] O.V. Patsahan and T.M. Patsahan. Phase equilibria of size- and charge-asymmetric primitive models of ionic fluids: the method of collective variables. *Condensed Matter*, 13, 2:23004, 2010.

[83] Jos Alejandre, Fernando Bresme, and Minerva Gonzlez-Melchor. Interfacial properties of charge asymmetric ionic liquids. *Mol. Phys.*, 107:357–363, 2010.

[84] M J Gillan. A simple model for the classical one-component plasma. *J. Phys. C: Solid State Phys*, 7:L1–L4, 1974.

[85] EE Salpeter. Energy and pressure of a zero-temperature plasma. *Astrophysical Journal*, 134(3):669–682, 1961.

[86] E Wigner. On the interaction of electrons in metals. *Physical Review*, 46:1002–1011, 1934.

[87] M Baus and JP Hansen. Statistical-mechanics of simple coulomb-systems. *Physics Reports- Review section of Physics Letters*, 59, 1:1–94, 1980.

[88] M. E. Fisher and D. Ruelle. The stability of many-particle systems. *J. Math. phys*, 7:260, 1966.

[89] R. D. Groot. Electrostatic interactions in dissipative particle dynamics - simulation of polyelectrolytes and anionic surfactants. *J. Chem. Phys*, 118:11265, 2003.

[90] M. Gonzalez-Melchor, E. Mayoral, M. E. Velazquez, and J. Alejandre. Electrostatic interactions in dissipative particle dynamics using the ewald sums. *J. Chem. Phys*, 125:224107, 2006.

[91] B. Philipp, H. Dautzenberg, K.J. Lonow, J.Koetz, and W.Dawydoff. *Prog. Polym. Sci*, 14:81, 1989.

[92] HM Buchhammer, M Mende, and M Oelmann. Formation of mono-sized polyelectrolyte complex dispersions: effects of polymer structure, concentration and mixing conditions. *Colloids And Surfaces A-Physiochemical and Engineering Aspects*, 218:151–159, 2003.

[93] A. Nikoubashman, J.-P. Hansen, and G. Kahl. Mean-field theory of the phase diagram of ultrasoft, oppositely charged polyions in solution. *J. Chem. Phys*, 137:094905, 2012.

[94] Matej Kandu, Ali Naji, Jan Forsman, and Rudolf Podgornik. Attraction between neutral dielectrics mediated by multivalent ions in an asymmetric ionic fluid. *J. Chem. Phys*, 137:174704, 2012.

[95] Gregor Trefalt, Istvan Szilagyi, and Michal Borkovec. Poissonboltzmann description of interaction forces and aggregation rates involving charged colloidal particles in asymmetric electrolytes. *Journal of Colloid and Interface Science*, 406:111–120, 2013.

[96] Yu. P. Monarkha and V. E. Syvokon. A two-dimensional wigner crystal. *Low Temperature Physics*, 38, 12:1067–1095, 2012.

[97] B. I. Shklovskii. Wigner crystal model of counterion induced bundle formation of rodlike polyelectrolytes. *Phys. Rev. Lett.*, 82:3268–3271, Apr 1999.

[98] ML Henle and PA Pincus. Equilibrium bundle size of rodlike polyelectrolytes with counterion-induced attractive interactions. *Phys. Rev. E*, 71, 2005.

[99] Ghee Hwee Lai, Rob Coridan, Olena V. Zribi, Ramin Golestanian, and Gerard C. L. Wong. Evolution of growth modes for polyelectrolyte bundles. *Phys. Rev. Lett.*, 98:187802, 2007.

[100] Jay X. Tang, Shuen Wong, Phong T. Tran, and Paul A. Janmey. Counterion induced bundle formation of rodlike polyelectrolytes. *Berichte der Bunsengesellschaft for physikalische Chemie*, 100(6):796–806, 1996.

[101] JX Tang, T Ito, T Tao, P Traub, and PA Janmey. Opposite effects of electrostatics and steric exclusion on bundle formation by f-actin and other filamentous polyelectrolytes. *Biochemistry*, 36:12600–12607, 1997.

[102] JX Tang and PA Janmey. The polyelectrolyte nature of f-actin and the mechanism of actin bundle formation. *Journal of Biological Chemistry*, 271, 15:8556–8563, 1996.

[103] C Guaqueta, LK Sanders, GCL Wong, and E Luijten. The effect of salt on self-assembled actin-lysozyme complexes. *Biophysical Journal*, 90, 12:4630–4638, 2006.

[104] LK Sanders, C Guaqueta, TE Angelini, JW Lee, SC Slimmer, E Luijten, and GCL Wong. Structure and stability of self-assembled actin-lysozyme complexes in salty water. *Phys. Rev. Lett.*, 95, 10:108302, 2005.

[105] AP Lyubartsev, JX Tang, PA Janmey, and L Nordenskiold. Electrostatically induced polyelectrolyte association of rodlike virus particles. *Phys. Rev. Lett.*, 81, 24:5465–5468, 1998.

[106] JC Butler, T Angelini, JX Tang, and GCL Wong. Ion multivalence and like-charge polyelectrolyte attraction. *Phys. Rev. Lett.*, 91, 2:028301, 2003.

[107] A Suzuki, M Yamazaki, and T Ito. Osmoelastic coupling in biological structures-formation of parallel bundles of actin-filaments in a crystalline-like structure caused by osmotic-stress. *Biochemistry*, 28, 15:6513–6518, 1989.

[108] P Podgornik, DC Rau, and VA Parsegian. Parametrization of direct and soft steric-undulatory forces between dna double-helical polyelectrolytes in solutions of several different anions and cations. *Biophysical Journal*, 66, 4:962–971, 1994.

[109] VA Bloomfield. Condensation of dna by multivalent cations - considerations on mechanism. *Biopolymers*, 31, 13:1471–1481, 1991.

[110] VA Bloomfield. Dna condensation. *Current Opinion in Structural Biology*, 6, 3:334–341, 1996.

[111] M. Stevens. Bundle binding in polyelectrolyte solutions. *Phys. Rev. Lett.*, 82, 1:101–104, 1999.

[112] I Prigogine and R Defay. Chemical thermodynamics. *Longmans Green*, 1954.

[113] J. D. Jackson. Classical electrodynamics. *John Wiley and Sons Ltd*, 1962.

[114] Jean-Pierre Hansen and Ian Ranald McDonald. *Theory of Simple Liquids*. Academic Press, London, 2nd edition, 2006.

[115] R. L. Stratonovich. A method for the computation of quantum distribution functions. *Dokl. Akad. Nauk SSSR*, 115(6):1097–1100, 1957.

[116] J. Hubbard. Calculation of partition functions. *Phys. Rev. Lett.*, 3:77–78, Jul 1959.

[117] P. Weiss. Radium. *J. Phys.*, 6:667, 1907.

[118] Ali Naji, Swetlana Jungblut, André G. Moreira, and Roland R. Netz. Electrostatic interactions in strongly coupled soft matter. *Physica A: Statistical Mechanics and its Applications*, 352(1):131 – 170, 2005.

[119] Hagen Kleinert. *Path Integrals in Quatum Mechanics, Statistics, and Polymer Physics*. World Scientific, Singapore, 2nd edition, 1995.

[120] Alexandre Diehl, Marcia C. Barbosa, and Yan Levin. Sine-gordon mean field theory of a coloumb gas. *Phys. Rev. E*, 56(1):619–622, 1997.

[121] Leo Lue. A variational field theory for solutions of charged, rigid particles. *Fluid Phase Equil.*, 241:236–247, 2006.

[122] Yng-Gwei Chen, C. Kaur, and J.D. Weeks. Connecting systems with short and long ranged interactions:local molecular field theory for ionic fluids. *J. Phys. Chem. B*, 108:19874–19884, 2004.

[123] Marius M. Hatlo and Leo Lue. The role of image charges in the interactions between colloidal particles. *Soft Matter*, 4:1582–1596, 2008.

[124] E Luijten, ME Fisher, and AZ Panagiotopoulos. Universality class of criticality in the restricted primitive model electrolyte. *Phys. Rev. Lett.*, 88(18):185701, 2002.

[125] Berk Hess, Carsten Kutzner, David van der Spoel, and Erik Lindahl. Gromacs 4: Algorithms for highly efficient, load-balanced, and scalable molecular simulation. *J. Chem. Theory Comput.*, 4(3):435–447, 2008.

[126] R.W Hockney, S.P Goel, and J.W Eastwood. Quiet high-resolution computer models of a plasma. *J. Comput. Phys.*, 14(2):148 – 158, 1974.

[127] Shuichi Nose. A molecular dynamics method for simulations in the canonical ensemble. *Mol. Phys.*, 52(2):255–268, 1984.

[128] William G. Hoover. Canonical dynamics: Equilibrium phase-space distributions. *Phys. Rev. A*, 31:1695–1697, 1985.

[129] Tom Darden, Darrin York, and Lee Pedersen. Particle mesh ewald: An n [center-dot] log(n) method for ewald sums in large systems. *J. Chem. Phys.*, 98(12):10089–10092, 1993.

[130] R Clausius. On a mechanical theorem applicable to heat. *Philios Mag*, 40:122–127, 1870.

[131] JF Springer, MA Pokrant, and FA Stevens. Integral equation solutions for classical electron gas. *J. Chem. Phys*, 58, 11:4863–4867, 1973.

[132] R. J. F. Leote de Carvalho, R. Evans, and Y. Rosenfeld. Decay of correlations in fluids: The one-component plasma from debye-hckel to the asymptotic-high-density limit. *Phys. Rev. E*, 59(1435), 1999.

[133] RG Palmer. *J. Chem. Phys*, 73:1980, 2009.

[134] Hugh E. DeWitt. Asymptotic form of the classical one-component plasma fluid equation of state. *Phys. Rev. A*, 14(1290), 1976.

[135] KC Ng. Hypernetted chain solutions for classical one-component plasma up to gamma=7000. *J. Chem. Phys*, 61, 7:2680–2689, 1974.

[136] F Lado, SM Foiles, and NW Ashcroft. Solutions of the reference hypernetted-chain equation with minimized free-energy. *Phys. Rev. A*, 28, 4:2374–2379, 1983.

[137] FJ Rogers and DA Young. New, thermodynamically consistent, integral-equation for simple fluids. *Phys. Rev. A*, 30, 2:999–1007, 1984.

[138] M.N. Tamashiro, Yan Levin, and Marcia C. Barbosa. The one-component plasma: A conceptual approach. *Physica*, 268:24–49, 1999.

[139] MC Barbosa, M Deserno, and C Holm. A stable local density functional approach to ion-ion correlations. *Europhys. Lett.*, 52(1):80–86, 2000.

[140] A. G. Moreira and R. R. Netz. One-component-plasma: Going beyond Debye-Hückel. *Eur. Phys. J. D*, 8(1):145–149, 2000.

[141] NV Brilliantov. Accurate first-principle equation of state for the one-component plasma. *Contributions to Plasma Physics*, 38(4):489–499, 1998.

[142] Marius M. Hatlo, Argyrios Karatrantos, and Leo Lue. One-component plasma of point charges and of charged rods. *Phys. Rev. E*, 80(6):061107, 2009.

[143] D. M. Heyes and G. Rickayzen. Continuous distributions of charges: Extensions of the one component plasma. *J. Chem. Phys*, 140:024506, 2014.

Appendix A - Publication

Chapter 2

A Field Theory Approach for Modeling Electrostatic Interactions in Soft Matter

Paul Duncan,[a] Marius M. Hatlo,[b] and Leo Lue[a]

[a]*Department of Chemical and Process Engineering, University of Strathclyde, James Weir Building, 75 Montrose Street, Glasgow G1 1XJ, UK*
[b]*Institute for Theoretical Physics, Utrecht University, Leuvenlaan 4, 3584 CE Utrecht, The Netherlands*
leo.lue@strath.ac.uk

2.1 Introduction

Field theoretic approaches have been particularly useful in studying colloidal and biological systems, in which long-range electrostatic interactions are important. For weakly coupled systems, the field theoretic methods reduce to the commonly known Poisson-Boltzmann (PB) theory [Chapman (1913); Gouy (1910)], which has been shown to be very accurate for these systems and has been used with great success to understand and solve numerous problems in soft matter. However, in recent decades, focus has turned toward strongly coupled systems, where highly charged surfaces or multivalent counterions introduce strong correlations, that cannot be treated by a mean field theory or approaches in which

the fluctuations are assumed to be weak (e.g., loop expansions). These correlations are important in many systems [Levin (2002); Naji *et al.* (2005); Messina (2009)] and can lead to many effects that cannot be explained by the PB theory, such as attraction between like-charged surfaces.

This work reviews a general field theoretic method to describe the behavior of systems interacting with electrostatics. This approach allows approximations that yield fairly accurate predictions, from the weak coupling regime, in which mean field theories work well, to the strong coupling regime, as well as in between. In addition, these approximations can, in principle, be systematically improved. The method provides a single, unified theoretical approach that is applicable to systems of arbitrary geometries and particles with general shapes and charge distributions. The method is, in general, in good agreement with Monte Carlo simulations, may be systematically improved, and is mathematically similar to the Poisson-Boltzmann theory.

In the next section, we present this general theoretical framework, introducing physical motivation and mathematical details. Then, in the Section 2.3, we discuss the application of the theory to various systems. Finally, the main aspects of the theory are summarized in Section 2.4.

2.2 Basic Formalism

In this work, we consider a system of mobile particles with an extended charge distribution that are immersed in a spatially varying continuum dielectric $\epsilon(\mathbf{r})$. The charge density of a particle of type α that is located at the origin and is in an orientation Ω is $Q_\alpha(\mathbf{r}, \Omega)$. In addition, there may also be a fixed background charge $\Sigma(\mathbf{r})$.

The total electrostatic energy of the system is

$$E_{\text{elec}} = \frac{1}{2} \int d\mathbf{r} d\mathbf{r}' \mathcal{Q}(\mathbf{r}) G_0(\mathbf{r}, \mathbf{r}') \mathcal{Q}(\mathbf{r}') \tag{2.1}$$

where G_0 is the Green's function of the Poisson equation

$$-\frac{1}{4\pi} \nabla \cdot [\epsilon(\mathbf{r}) \nabla G_0(\mathbf{r}, \mathbf{r}')] = \delta^d(\mathbf{r} - \mathbf{r}'), \tag{2.2}$$

and $\mathcal{Q}(\mathbf{r})$ is the total charge density of the system

$$\mathcal{Q}(\mathbf{r}) = \sum_{\alpha,k} Q_\alpha(\mathbf{R}_{\alpha,k}, \Omega_{\alpha,k}) + \Sigma(\mathbf{r}), \tag{2.3}$$

where $\mathbf{R}_{\alpha,k}$ and $\Omega_{\alpha,k}$ are the position and orientation, respectively, of the kth particle of type α. Physically, $G_0(\mathbf{r}, \mathbf{r}')$ is the electrostatic potential at a position $\mathbf{r}$ due to a unit point charge located at $\mathbf{r}'$; it dictates how the electrostatic potential emanates from a charge.

Formally, the grand partition function of this system can be written exactly as an integral over all the positions and orientations of the particles in the system [Hansen and McDonald (2006)]; however, the direct evaluation of the resulting integral is intractable for most systems. Liquid state approaches to evaluating the partition function (e.g., hypernetted chain theory) focus on the particles in the system and how to develop approximations for correlations between them. These approaches work well in capturing the short-range correlations and fluctuations that occur in the system.

Another perspective is to use a field theoretic approach. In this case, the focus is no longer on the particles in the system but rather on collective modes, such as the density or an effective one-body interaction potential generated by the particles. Mathematically, this is done by representing the grand partition function as a functional integral over an interaction field through the use of the Hubbard–Stratonovich transformation [Stratonovich (1957); Hubbard (1959)]. In the case of our system of charged particles, the grand partition function Z_G becomes

$$Z_G[\gamma, \Sigma] = \left\langle Z_G^{\text{ref}}[\gamma - qi\psi] \exp\left[-\int d\mathbf{r}\Sigma(\mathbf{r})i\psi(\mathbf{r})\right] \right\rangle_0 \tag{2.4}$$

where $\psi(\mathbf{r})$ is a Gaussian random field with mean zero and a spatial correlation of $\beta G_0(\mathbf{r}, \mathbf{r}')$ (where $\beta = 1/(k_B T)$, k_B is the Boltzmann constant, and T is the absolute temperature), the angle brackets denote the average with respect to ψ, and Z_G^{ref} is the grand partition function of the system without electrostatic interactions. The partition function of a system with electrostatic interactions is the same as the partition function of the same system without electrostatic interactions, but with the particles coupled to a randomly fluctuating Gaussian field with a covariance given by the Green's function of the Poisson equation.

This transformation is formally exact, but the resulting functional integral is just as intractable as the original, particle-based partition function. Several different approximation schemes have been developed to evaluate this functional integral, including the mean-field approximation, loop expansions, and variational methods. These approximation schemes are better able to handle the long wavelength correlations that occur in the system.

Neither the particle-based theories nor the functional integral formulations lead to a theory that works well when the system contains highly charged particles (e.g., colloidal particles). For these systems, fluctuations at both short and long wavelengths become important. At short length scales, oppositely charged particles interact strongly with each other, forming bound objects, whereas at large length scales, these composite objects screen and interact through effective electrostatic forces. To describe these systems, very successful *ad hoc* approaches have been developed, such as the strong coupling expansion [Shklovskii (1999); Moreira and Netz (2000)] and dressed colloid theories [Colla and Levin (2010); Lu and Denton (2010)], in which the charge of the colloids is renormalized due to counterion binding. However, we are interested in developing an approach in which this binding arises naturally from the theory, without explicitly putting it into the theory. This is important when the electrostatic interaction leads to binding and aggregation over multiple length scales (e.g., binding of counterions onto charged rods that can themselves bundle to form larger objects that organize).

2.2.1 *Splitting*

Particle-based approaches work well for describing short wavelength correlations, whereas field theory based approaches work well for long wavelength correlations. The idea behind our approximation scheme is to divide the fluctuations of the system into short and long wavelength contributions and to treat each of these contributions in an appropriate approximation [Hatlo and Lue (2009, 2010)].

To achieve this, the Green's function is divided as $G_0 = G_s + G_l$, where $G_l = \mathcal{P}G_0$, $G_s = (1 - \mathcal{P})G_0$, and $\mathcal{P}$ is an operator that projects

out the long wavelength components of a function. The precise form of $\mathcal{P}$ is fairly arbitrary, but in most of our work, we use $\mathcal{P} = [1 - \sigma^2 \nabla^2 + \sigma^4 \nabla^4]^{-1}$, where σ is the splitting parameter and is a length that separates short and long wavelength phenomena.

The Hubbard–Stratonovich transformation is performed separately for both G_s and G_l, which leads to functional integrals over the associated random fields ψ_s (correlated at short wavelengths) and ψ_l (correlated at long wavelengths). The averages over these fields are performed using different approximations, which are described in the next sections.

2.2.2 *Short Wavelength Field*

The short wavelength field ψ_s is strongly fluctuating, and we approximate averages over it using a truncated cumulant expansion. The resulting expression becomes equivalent to a virial series in which the particles interact with an effective one-body potential

$$u_\alpha(\mathbf{R}, \Omega) = \sum_\alpha \int d\mathbf{r}\, Q_\alpha(\mathbf{r} - \mathbf{R}, \Omega)\Sigma(\mathbf{r})$$
$$+ \sum_\alpha \frac{\beta}{2} \int d\mathbf{r} d\mathbf{r}'\, Q_\alpha(\mathbf{r} - \mathbf{R}, \Omega)\Delta G_0(\mathbf{r}, \mathbf{r}')Q_\alpha(\mathbf{r}' - \mathbf{R}, \Omega)$$
$$- \sum_\alpha \frac{\beta}{2} \int d\mathbf{r} d\mathbf{r}'\, Q_\alpha(\mathbf{r} - \mathbf{R}, \Omega)G_l(\mathbf{r}, \mathbf{r}')Q_\alpha(\mathbf{r}' - \mathbf{R}, \Omega)$$

$$(2.5)$$

and a two-body potential, given by the short wavelength contribution of the electrostatics

$$v_{\alpha\alpha'}(\mathbf{R}, \Omega, \mathbf{R}', \Omega') = \int d\mathbf{r} d\mathbf{r}'\, Q_\alpha(\mathbf{r} - \mathbf{R}, \Omega)G_s(\mathbf{r}, \mathbf{r}')Q_{\alpha'}(\mathbf{r}' - \mathbf{R}', \Omega'),$$

as well as other nonelectrostatic interactions present in the system.

2.2.3 *Long-wavelength Field*

A single configuration of the long-wavelength field, which is slowly varying in space, is expected to dominate the contributions to the partition function. Configurations that deviate substantially from this main configuration are not expected to make a significant contribution. The contribution of fluctuations is weak.

To approximate this, we use a variational perturbation approximation [Kleinert (1995); Curtis and Lue (2005)], where fluctuations in ψ_l are evaluated with respect to a Gaussian distribution with mean $\bar{\psi}_l$ and a covariance $\beta G_{\mathcal{K}}(\mathbf{r}, \mathbf{r}')$, a renormalized Green's function, defined through $G_{\mathcal{K}}^{-1}(\mathbf{r}, \mathbf{r}') = G_0^{-1}(\mathbf{r}, \mathbf{r}') + \mathcal{K}(\mathbf{r}, \mathbf{r}')$. Physically, $\mathcal{K}$ is a screening function that describes the influence of mobile charges, and $G_{\mathcal{K}}$ describes the propagation of the electric potential under the influence of these charges. A cumulant expansion is used to account for deviations from this Gaussian distribution. The case $\mathcal{K} = 0$ corresponds to the mean field approximation.

2.2.4 *Free Energy*

With a first-order variational perturbation approximation used to evaluate the averages over ψ_l and a second-order cumulant expansion for the averages over ψ_s, the free energy is given by

$$
\begin{aligned}
F[\rho, \Sigma] = & \sum_{\alpha} \int d\mathbf{R} d\Omega \, \rho_\alpha(\mathbf{R}, \Omega)[\ln \rho_\alpha(\mathbf{R}, \Omega)\Lambda_\alpha^d - 1] \\
& + \sum_{\alpha} \int d\mathbf{R} d\Omega \, \rho_\alpha(\mathbf{R}, \Omega)\beta u_\alpha(\mathbf{R}, \Omega) \\
& + \frac{1}{2} \sum_{\alpha, \alpha'} \int d\mathbf{R} d\Omega \, d\mathbf{R}' d\Omega' \, [e^{-\beta v_{\alpha\alpha'}(\mathbf{R}, \Omega, \mathbf{R}', \Omega')} - 1] \\
& - \frac{1}{2\beta} \int d\mathbf{r} d\mathbf{r}' i\bar{\psi}_l(\mathbf{r}) G_l^{-1}(\mathbf{r}, \mathbf{r}') i\bar{\psi}_l(\mathbf{r}') + \int d\mathbf{r} \Sigma(\mathbf{r}) i\bar{\psi}_l(\mathbf{r}) \\
& + \int d\mathbf{r} \sum_{\alpha} \int d\mathbf{R} d\Omega \, \rho_\alpha(\mathbf{R}, \Omega) Q_\alpha(\mathbf{r} - \mathbf{R}, \Omega) i\bar{\psi}_l(\mathbf{r}) \\
& + \frac{1}{2} \int_0^1 d\zeta \, \text{Tr} \mathcal{K}(G_{\zeta\mathcal{K}} - G_l). \quad (2.6)
\end{aligned}
$$

The first two terms in the expression for the free energy functional is the ideal gas contribution. The second term is the interaction of the particles with a renormalized external potential $u_\alpha(\mathbf{R}, \Omega)$. The third term is second virial contribution of the short wavelength electrostatic interaction between particles. The next three terms are the long-wavelength electrostatic energy of the system. The final term represents the contribution of long-wavelength fluctuations of the electrostatic potential to the free energy.

To complete the theory, we need to specify the forms of $\bar{\psi}_l$, $\mathcal{K}$, and σ. If we were able to exactly evaluate the averages over the fluctuations of the fields ψ_s and ψ_l, then the free energy would be independent of the choice of $\bar{\psi}_l$, $\mathcal{K}$, and σ. However, because of the approximations used, the free energy will depend on these quantities; in order to minimize this dependence, we select these quantities such that the free energy is stationary with respect to small variations in their values.

Making the free energy stationary with respect to variations in $\bar{\psi}_l(\mathbf{r})$ leads to the Poisson equation:

$$-\frac{1}{4\pi}\nabla \cdot \epsilon(\mathbf{r})\nabla\phi(\mathbf{r}) = \sum_\alpha \int d\mathbf{R}\,d\Omega\, Q_\alpha(\mathbf{r}-\mathbf{R},\,\Omega)\rho_\alpha(\mathbf{R},\,\Omega) + \Sigma(\mathbf{r})$$

(2.7)

where $\phi(\mathbf{r}) = \beta^{-1}\mathcal{P}\psi_l(\mathbf{r})$ is the mean electric potential in the system.

The value of the screening function is determined by making the free energy stationary with respect to variations in $\mathcal{K}(\mathbf{r}, \mathbf{r}')$. For systems in which electrostatics is the only mode of interaction and neglecting the third term in Eq. (2.6), the screening function becomes:

$$\mathcal{K}(\mathbf{r}, \mathbf{r}') = \beta \sum_\alpha \int d\mathbf{R}\,d\Omega\, Q_\alpha(\mathbf{r}-\mathbf{R},\,\Omega)\rho_\alpha(\mathbf{R},\,\Omega)Q_\alpha(\mathbf{r}'-\mathbf{R},\,\Omega) \quad (2.8)$$

This is a simple generalization of the Debye-Hückel theory for systems with extended charge distributions.

The value of the splitting parameter is determined from $\partial F/\partial\sigma = 0$. Simply setting $\sigma = 0$ corresponds to using the variational approximation for all the fluctuations in the system. In the limit where $\sigma \to \infty$, the theory reduces to a virial expansion or other liquid state theory approximations. In this case, the theory resembles the strong coupling expansions [Shklovskii (1999); Moreira and Netz (2000)], which are able to accurately describe systems in which electrostatic interactions dominate.

2.3 Applications

The theoretical approach developed in the previous section is quite versatile and applicable to a wide variety of problems. In this section,

we present its application to the one-component plasma (OCP), counterions confined between two charged plates, and counterions around a single charged dielectric sphere within the cell model.

2.3.1 *One-component Plasma*

In the OCP model, ions of charge q are contained within a rigid, uniform charge density $\Sigma = -q\rho$, where ρ is the ion number density, so that the system is electrically neutral. Typically, these ions are point charges, but here we generalize the model slightly, so that they are linear charge distributions of length L, such as a uniform line charge or a linear sequence of rigidly bonded point charges. The key parameters that govern the properties of this OCP model are the coupling parameter $\Gamma = \rho^{1/3}l_B$ (the ratio of the mean spacing between the counterions and the range of the interaction), and the ratio L/l_B.

In Fig. 2.1(a), we show the interaction energy of the OCP for 8-mer rods of various lengths. The lines are the predictions of the splitting theory, and the symbols are from molecular dynamics simulations [Hatlo *et al.* (2009)]. The dashed line is the prediction of the Debye-Hückel theory for point charges, which corresponds to the splitting theory with $\sigma = 0$.

(a)   (b)
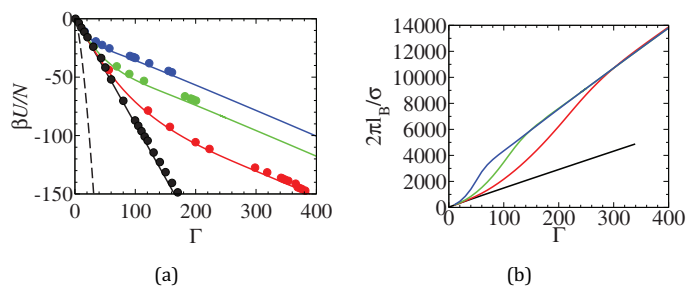
Figure 2.1   (a) Electrostatic interaction energy for 8-mer rods with: (i) $L/l_B = 0$ (black), (ii) $L/l_B = 0.025$ (red), and (iii) $L/l_B = 0.05$ (green), (iv) $L/l_B = 0.1$ (blue). The solid lines are the predictions of the splitting theory, and the dashed line is the prediction of the Debye-Hückel theory ($\sigma = 0$). The symbols are from molecular dynamics simulations. (b) Splitting parameter.

The corresponding values of the splitting parameter σ are shown in Fig. 2.1(b). The splitting parameter shrinks as the mean spacing between particles decreases. We find that it corresponds to the size of the "correlation hole," [Nordholm (1984); Forsman and Nordholm (2012)] which develops around each ion due to their strong repulsion at short distances.

Interestingly, the rod-like counterion systems show an ordering transition from an isotropic phase when the length of the counterions are much smaller than the Bjerrum length to a nematic phase at sufficiently high values of L/l_B, similar to that observed for long thin rods with only excluded volume interactions [Onsager (1949)].

2.3.2 *Planar Geometry*

Now, we examine the case wherein ions of charge q are confined between two plates with a uniform charge density Σ and separated by a distance D. The two length scales that characterize this system are [Moreira and Netz (2001)] the Bjerrum length $l_B = \beta q^2$ and the Gouy-Chapman length $\mu = (2\pi\beta\Sigma q)^{-1}$.

In Fig. 2.2, we plot the equilibrium curve of the two-plate system. The symbols are from Monte Carlo simulations [Moreira and Netz (2001)]. The solid line is the splitting theory with the mean field approximation for the long wavelength fluctuations and the cumulant expansion truncated at zeroth order. The dashed line is the prediction of the same splitting theory but with the cumulant expansion truncated at first order. As a comparison, we also present the predictions of a theory developed by Šamaj and Trizac (2011), based on a low temperature expansion around a two-dimensional Wigner crystal condensed on both plates (dotted line in Fig. 2.2).

As in the case of the OCP discussed previously, the splitting theory can be extended for two-plate system to the situation in which the counterions consist of extended charge distributions. In the case in which the counterions are a linear collection of point charges, there are two mechanisms for an attraction between the plates: correlations between counterions (similarly to the point charge) and correlations within a counterion, which leads to "bridging" of the counterion across the two plates. These two mechanisms can lead to two separate regions of attraction between
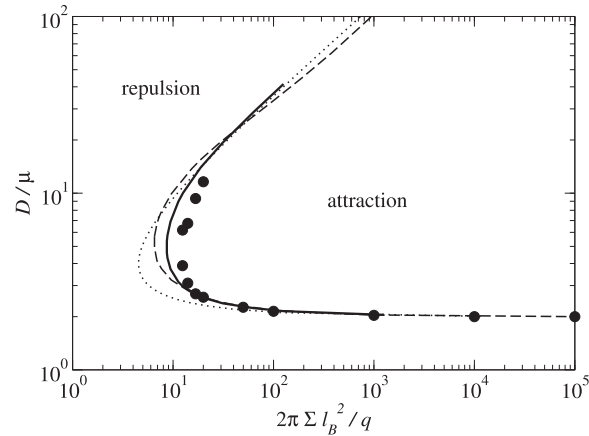
Figure 2.2   Equilibrium distance between two charged plates. The solid line is the prediction of the splitting theory with the second virial correction, and the dashed line is without the correction. The dotted line is the prediction of the Šamaj and Trizac [Šamaj and Trizac (2011)]. The symbols are Monte Carlo simulation data [Moreira and Netz (2001)].

the plates if the length of the counterions is sufficiently large [Hatlo *et al.* (2010); Bohinc and Lue (2011); Bohinc *et al.* (2012)].

2.3.3 *Spherical Cell Model*

Finally, we examine systems of spherical macroions of radius R_M and total charge Q, which occupy a volume fraction 0.01, along with a neutralizing number of point counterions of charge q. The interior of the sphere has a dielectric constant ε', whereas outside the sphere, the dielectric constant is ε.

This system is studied [Lue and Linse (2011)] within the cell model, wherein the environment around a single macroion is examined. We focus on four systems, which span a range of conditions: (I) $Q/q = -10$ and $R_M/l_B = 2.81$; (II) $Q/q = -80$ and $R_M/l_B = 2.81$; (III) $Q/q = -40$ and $R_M/l_B = 0.703$; and (IV) $Q/q = -80$ and $R_M/l_B = 22.5$.

The counterion density profiles for each of the systems are shown in Fig. 2.3(a). The predictions of PB theory (dotted lines)
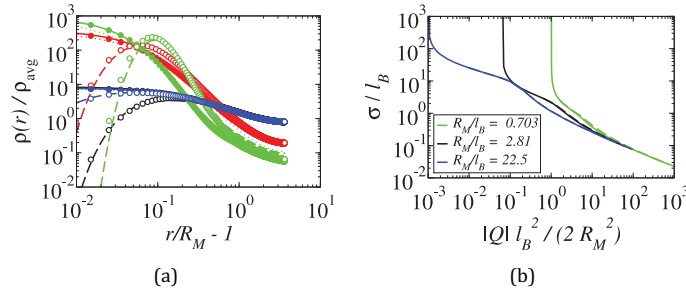
Figure 2.3 (a) Normalized counterion number density as a function of the distance from the center of the sphere for System I (black), II (red), III (green), and IV (blue). The solid lines are predictions of the splitting theory for $\varepsilon'/\varepsilon = 1$, the dashed lines are the predictions of the splitting theory for $\varepsilon'/\varepsilon = 1/78.4$, and the dotted lines are predictions of PB theory. The symbols are Monte Carlo simulation data for $\varepsilon'/\varepsilon = 1$ (filled) and $\varepsilon'/\varepsilon = 1/78.4$ (open). (b) Reduced splitting parameter.

are only in good agreement with the simulation data (symbols) for the weakly coupled systems. The predictions of the splitting theory (given by the solid and dashed lines) are in fairly good agreement with the simulation data, even for the strongly coupled system.

In Fig. 2.3(b), we show the variation of the splitting parameter with the macroion charge. One interesting feature is that σ diverges when the macroion charge becomes less than that of one counterion. In this case, the splitting theory reduces exactly to that of a single ion. The PB theory is unable to reproduce this limit, even in the region of very low surface charge densities, because it does not account for the discreteness of the counterions.

2.4 Conclusions

We have presented a general theoretical framework for treating electrostatic interactions in soft matter, which can be particularly useful in studying charged colloidal suspensions and electrolyte solutions wherein long-range interactions are important. The key physical motivation behind the theory is to treat the short and long wavelength fluctuations in the system within different approxima-

tion schemes. At short range, the systems are strongly coupled, and at long range, the systems are weakly coupled. To describe both these regimes within a single theory, we split the interaction into a short and long-range contribution. The long-range behavior is often well approximated by a mean field theory, or including first-order fluctuation corrections, whereas the short-range behavior can be captured by a virial expansion, or other liquid state methods suitable to describe particles with short range pair interactions. For weakly coupled systems, this theory approaches the Poisson-Boltzmann theory, whereas for strongly coupled systems, the theory resembles the strong coupling expansion. The theory also performs well for intermediate couplings. In addition, the accuracy of the theory can, in principle, be systematically improved. The theory can be applied to a wide variety of problems, such as systems with different geometries and conditions (e.g., dielectric interfaces) and particles with different shapes and charge distributions. As examples of how the theory may be used, we presented results for systems involving charged objects with neutralizing counterions. These fairly simple systems show a range of interesting phenomena, such as electrostatically driven isotropic-nematic transition and like-charge attraction, which cannot be captured with mean field approximations.

References

Bohinc, K., Grime, J. M. A. and Lue, L. (2012). The interactions between charged colloids with rod-like counterions, *Soft Matter* **8**, pp. 5679–5686.

Bohinc, K. and Lue, L. (2011). Interaction of similarly charged surfaces mediated by nanoparticles, *Chin. J. Polymer Sci.* **29**, 4, pp. 414–420.

Chapman, D. L. (1913). A contribution to the theory of electroencapillarity, *Philos* **25**, pp. 475–481.

Colla, T. E. and Levin, Y. (2010). The renormalized jellium model of colloidal suspensions with multivalent counterions, *J. Chem. Phys.* **133**, p. 234105.

Curtis, R. A. and Lue, L. (2005). Electrolytes at spherical dielectric interfaces, *J. Chem. Phys.* **123**, p. 174702.

Forsman, J. and Nordholm, S. (2012). Polyelectrolyte mediated interactions in colloidal dispersions: Hierarchical screening, simulations, and a new classical density functional theory, *Langmuir* **28**, 9, pp. 4069–4079.

Gouy, G. (1910). Sur la constitution de la charge electique a la surface d'un electrolyte, *J. Phys. Radium* **9**, pp. 468–475.

Hansen, J.-P. and McDonald, I. R. (2006). *Theory of Simple Liquids*, 2nd edn. (Academic Press, London).

Hatlo, M. M., Bohinc, K. and Lue, L. (2010). The properties of dimers confined between two charged plates, *J. Chem. Phys.* **132**, 11, 114102.

Hatlo, M. M., Karatrantos, A. and Lue, L. (2009). One-component plasma of point charges and of charged rods, *Phys. Rev. E* **80**, 6, 061107.

Hatlo, M. M. and Lue, L. (2009). A field theory for ions near charged surfaces valid from weak to strong couplings, *Soft Matter* **5**, pp. 125–133.

Hatlo, M. M. and Lue, L. (2010). Electrostatic interactions of charged bodies from the weak- to the strong-coupling regime, *EPL (Europhysics Letters)* **89**, 2, p. 25002.

Hubbard, J. (1959). Calculation of partition functions, *Phys. Rev. Lett.* **3**, pp. 77–78.

Šamaj, L. and Trizac, E. (2011). Counterions at highly charged interfaces: From one plate to like-charge attraction, *Phys. Rev. Lett.* **106**, p. 078301.

Kleinert, H. (1995). *Path Integrals in Quatum Mechanics, Statistics, and Polymer Physics*, 2nd edn. (World Scientific, Singapore).

Levin, Y. (2002). Electrostatic correlations: from plasma to biology, *Reports on Progress in Physics* **65**, pp. 1577–1632.

Lu, B. and Denton, A. R. (2010). Charge renormalization, thermodynamics, and structure of deionized colloidal suspensions, *Commun. Comput. Phys.* **7**, 2, pp. 235–249.

Lue, L. and Linse, P. (2011). Macroion solutions in the cell model studied by field theory and Monte Carlo simulations, *J. Chem. Phys.* **135**, 22, 224508.

Messina, R. (2009). Electrostatics in soft matter, *J. Phys.: Condens. Matter* **21**, 11, p. 113102.

Moreira, A. G. and Netz, R. R. (2000). Strong-coupling theory for counter-ion distributions, *Europhys. Lett.* **52**, 6, pp. 705–711.

Moreira, A. G. and Netz, R. R. (2001). Binding of similarly charged plates with counterions only, *Phys. Rev. Lett.* **87**, 7, p. 078301.

Naji, A., Jungblut, S., Moreira, A. G. and Netz, R. R. (2005). Electrostatic interactions in strongly coupled soft matter, *Physica A: Statistical Mechanics and its Applications* **352**, 1, pp. 131 – 170.

Nordholm, S. (1984). Simple analysis of the thermodynamic properties of the one-component plasma, *Chem. Phys. Lett.* **105**, 3, pp. 302–7.

Onsager, L. (1949). The effects of shape on the interaction of colloidal particles, *NY Acad. Sci.* **51**, pp. 627–659.

Shklovskii, B. I. (1999). Screening of a macroion by multivalent ions: Correlation-induced inversion of charge, *Phys. Rev. E* **60**, 5, pp. 5802–5811.

Stratonovich, R. L. (1957). A method for the computation of quantum distribution functions, *Dokl. Akad. Nauk SSSR* **115**, 6, pp. 1097–1100.

Appendix B- Charged Disks

We model clay as a one component plasma of charged disks, where the counterions are treated as a uniform background charge as per [121, 142]. The charge density for a disk of diameter D located at the origin is

$$Q(\mathbf{r}, \boldsymbol{\Omega}) = \frac{4q}{\pi D^2} \int_0^{D/2} r dr \int_0^{2\pi} d\theta \delta(\mathbf{r} - \hat{\mathbf{n}}_x(\boldsymbol{\Omega}) r \cos\theta - \hat{\mathbf{n}}_y(\boldsymbol{\Omega}) r \sin\theta)$$

$$\hat{Q}(\mathbf{p}, \boldsymbol{\Omega}) = q \frac{2 J_1(p_\perp D/2)}{p_\perp D/2}$$

Now, taking $z // \vec{p}$ we take the form of the director to be

$$\hat{n} = \begin{pmatrix} \sin\theta \cos\phi \\ \sin\theta \sin\phi \\ \cos\theta \end{pmatrix}$$

and

$$\hat{n}_0 = \begin{pmatrix} \sin\theta_0 \cos\phi_0 \\ \sin\theta_0 \sin\phi_0 \\ \cos\theta_0 \end{pmatrix}$$

we may write $\hat{n}.\hat{p} = \cos\theta$, $\hat{n}.\vec{p} = p\cos\theta$

$$p_\perp = (p^2 - (\mathbf{p}\cdot\hat{\mathbf{n}})^2)^{1/2}$$

$$= p^2 - (p\cos\theta)^2)^{1/2}$$

$$= p(1 - \cos^2\theta)^{1/2}$$

$$= p\sin\theta$$

Therefore $\hat{n}.\hat{n}_0$ may be written as

$$\hat{n}.\hat{n}_0 = \sin\theta\sin\theta_0\cos\phi\cos\phi_0 + \sin\theta\sin\theta_0\sin\phi\sin\phi_0 + \cos\theta\cos\theta_0$$

$$= \sin\theta\sin\theta_0(\cos\phi\cos\phi_0 + \sin\phi\sin\phi_0) + \cos\theta\cos\theta_0$$

$$= \sin\theta\sin\theta_0\cos(\phi - \phi_0) + \cos\theta\cos\theta_0$$

Now,

$$G_0(\mathbf{r}, \mathbf{r}') = G_s(\mathbf{r}, \mathbf{r}') + G_l(\mathbf{r}, \mathbf{r}')$$

where $G_s = (1 - \mathcal{P})G_0$, $G_l = \mathcal{P}G_0$. The operator $\mathcal{P}$ removes the short wavelength components of a function; its precise form is fairly arbitrary, and in this work we choose

$$\mathcal{P} = [1 - \sigma^2\nabla^2 + \sigma^4\nabla^4]^{-1}.$$

Within the variational splitting theory, the free energy is given by

$$\beta F[\rho, \Sigma] \approx \int d\mathbf{R} d\hat{\mathbf{n}} \, \rho(\mathbf{R}, \hat{\mathbf{n}}) \Big[\ln \rho(\mathbf{R}, \hat{\mathbf{n}}) \Lambda^d - 1 \Big] + \frac{1}{2} \int_0^1 d\zeta \mathrm{Tr} \mathcal{K}(G_{\zeta\mathcal{K}} - G_l)$$

$$+ \frac{1}{2\beta} \int d\mathbf{r} d\mathbf{r}' i\bar{\psi}_l(\mathbf{r}) G_l^{-1}(\mathbf{r}, \mathbf{r}') i\bar{\psi}_l(\mathbf{r}')$$

$$+ \beta \int d\mathbf{r} d\mathbf{r}' Q(\mathbf{r} - \mathbf{R}, \mathbf{\Omega}) G_s(\mathbf{r}, \mathbf{r}') \Sigma(\mathbf{r}') + \frac{\beta}{2} \int d\mathbf{r} d\mathbf{r}' \Sigma(\mathbf{r}) G_s(\mathbf{r}, \mathbf{r}') \Sigma(\mathbf{r}')$$

Details of the derivation of this free energy can be found in [142].

$$\kappa^2(\mathbf{r}, \mathbf{r}') = \frac{4\pi\beta}{\epsilon} \int d\mathbf{R} d\Omega Q(\mathbf{r} - \mathbf{R}, \mathbf{\Omega}) \rho(\mathbf{R}, \mathbf{\Omega}) Q(\mathbf{r}' - \mathbf{R}, \mathbf{\Omega}),$$

For the disk, this becomes:

$$\kappa^2(\mathbf{p}) = 4\pi\rho_D l_B z^2 \int d\hat{\mathbf{n}} \rho_D(\hat{\mathbf{n}}) \left[\frac{2J_1(p_\perp D/2)}{p_\perp D/2} \right]^2$$

where $z // \vec{p}$ gives $d\vec{n} \to \frac{d\cos\theta d\phi}{4\pi}$ so that

$$\kappa^2(\mathbf{p}) = l_B z^2 \int_{-1}^1 d\cos\theta \int_0^{2\pi} d\phi \rho_D f(\hat{n}.\hat{n_0}) \left[\frac{2J_1(p_\perp D/2)}{p_\perp D/2} \right]^2$$

$$= l_B \rho_D z^2 \int_{-1}^1 d\cos\theta \int_0^{2\pi} d\phi f(\sin\theta \sin\theta_0 \cos(\phi - \phi_0) + \cos\theta \cos\theta_0) \left[\frac{2J_1(p \sin\theta D/2)}{p \sin\theta D/2} \right]^2$$

To simplify the calculations, we choose the Onsager variational form

$$f(x) = a \frac{\cosh ax}{\sinh a}$$

$$f(\hat{\mathbf{n}} \cdot \hat{\mathbf{n}}_0) = \frac{a}{2\sinh a} \left[e^{a\hat{\mathbf{n}} \cdot \hat{\mathbf{n}}_0} + e^{-a\hat{\mathbf{n}} \cdot \hat{\mathbf{n}}_0} \right]$$

$$= \frac{a}{2\sinh a} \left[e^{\pm a \sin\theta \sin\theta_0 \cos(\phi - \phi_0) + \cos\theta \cos\theta_0} \right]$$

206

where a is a variational parameter. The limit $a = 0$ corresponds to an isotropic system, while the limit $a \to \infty$ corresponds to a system where all the disks are perfectly aligned. Now,

$$\int_0^{2\pi} d\phi e^{\pm a \sin \theta \sin \theta_0 \cos(\phi - \phi_0)} = \int_0^{2\pi} d\phi e^{\pm a \sin \theta \sin \theta_0 \cos \phi}$$

$$= 2\pi I_0(a \sin \theta \sin \theta_0)$$

where $I_0(x) = \frac{1}{2\pi} \int_0^{2\pi} d\phi e^{x \cos \phi}$. Now we may write

$$\int_0^{2\pi} d\phi f(\sin \theta \sin \theta_0 \cos(\phi - \phi_0) + \cos \theta \cos \theta_0) = \frac{a}{2 \sinh a} \left[2\pi I_0 \left(a \sin \theta \sin \theta_0 \right) e^{\pm a \cos \theta \cos \theta_0} \right)\right]$$

$$= \frac{2\pi a \cosh(a \cos \theta \cos \theta_0)}{\sinh a} I_0 \left(a \sin \theta \sin \theta_0 \right)$$

Now finally,

$$\kappa^2(\mathbf{p}) = 2 l_B z^2 \rho_D \int_0^{2\pi} d\cos \theta \frac{2\pi a \cosh(a \cos \theta \cos \theta_0)}{\sinh a} I_0 \left(a \sin \theta \sin \theta_0 \right) \left[\frac{2 J_1(p \sin \theta D/2)}{p \sin \theta D/2} \right]^2$$

$$= 4\pi l_B z^2 \rho_D \int_0^{2\pi} \sin \theta d\theta \frac{a \cosh(a \cos \theta \cos \theta_0)}{\sinh a} I_0 \left(a \sin \theta \sin \theta_0 \right) \left[\frac{2 J_1(p \sin \theta D/2)}{p \sin \theta D/2} \right]^2$$

For an isotropic solution, this simplifies to:

$$\kappa^2(\mathbf{p}) = 4\pi \rho_D l_B z^2 \frac{2}{(pD/2)^2} \left[1 - \frac{J_1(pD)}{pD/2} \right]$$

Using this trial function for the orientation distribution of the disks, the screening function can be simplified to

$$\kappa^2(\mathbf{p}) = 4\pi \rho_D l_B z^2 \int_0^{\pi/2} \sin \theta d\theta f(a \cos \theta \cos \theta_0) I_0(a \sin \theta \sin \theta_0) \left[\frac{2 J_1(pR \sin \theta)}{pR \sin \theta} \right]^2$$

where I_0 is the zeroth order modified Bessel function of the first kind. This allows us to write the Helmholtz free energy as

$$\frac{\beta F}{V} = \rho_D(\ln \rho_D \Lambda_D^d - 1) + \rho_D \left[\ln \frac{a \cosh a}{\sinh a} + \frac{\arctan \sinh a}{\sinh a} - 1 \right]$$

$$+ \frac{1}{2} \int_{\mathbf{p}} \left\{ \ln \left[1 + \frac{\hat{\mathcal{P}}(\mathbf{p})\kappa^2(\mathbf{p})}{p^2} \right] - \frac{\hat{\mathcal{P}}(\mathbf{p})\kappa^2(\mathbf{p})}{p^2} \right\} - \frac{1}{2}\rho^2 l_B z^2 4\pi\sigma^2$$